LAKEHEAD UNIVERSITY

Vibration Suppression and Energy Harvesting with a Variant Nonlinear Energy Sink

By

Xiaolin Li

A THESIS

SUBMITTED TO THE FAULTY OF GRADUATE STUDIES

IN PARTIAL FULFILMENT OF THE REQUIREMENT FOR THE

DEGREE OF MASTER OF SCIENCE

MECHANICAL ENGINEERING

THUNDER BAY, ONTARIO

April 2018

ABSTRACT

Vibration control is aimed to suppress or eliminate unwanted vibration to ensure proper operation of machines. On the other hand, energy harvesting intends to scavenge energy from ambient vibrations to power electronical devices such as wireless sensors. It is much desired to achieve simultaneous vibration control and energy harvesting. A great amount of effort has been focused on the use of a linear vibration absorber for this purpose. The shortcoming of such an approach is that its effectiveness is limited to a narrow bandwidth of frequency.

The goal of this research is to develop a device in order to achieve simultaneous vibration suppression and energy harvesting in a broad frequency band. Instead of using a linear vibration absorber, a nonlinear energy sink (NES) is considered. Since it is very challenging to realize a true NES as it requires a zero linear stiffness, this study focus on developing a variant NES that possesses a low linear stiffness but high nonlinear stiffness. Three designs and their corresponding apparatus are introduced. A base excitation is conducted to determine the spring restoring force in order to character the stiffness of each design. The apparatus that best emulates the NES is chosen. A stiff primary system and a flexible primary system are also developed by changing the primary spring's stiffness. The behaviors of the chosen variant NES are further investigated in two combined system: weakly coupled one (a stiff primary system plus the variant NES) and the strongly coupled one (a flexible primary system plus the variant NES). The transient responses of the two combined systems are investigated numerically and experimentally. The steady state responses of the two combined systems to a harmonic base excitation are investigated in numerically and experimentally. The results from both the weakly coupled and the strongly coupled systems show some typical features of the NES: 1:1 resonance, targeted energy transfer (TET), initial energy or excitation level dependence, jumping phenomena, and strongly modulated response (SMR), etc.

ACKNOWLEDGMENTS

First, I would like to express my sincere gratitude to my supervisor Dr. Kefu Liu who has provided me with valuable guidance during the course of this research. His academic passion and rigorousness have always been an inspiration to me. He has supported me in all aspects including thesis research and writing, career suggestion and my life in general.

I would also like to thank all my lab mates: John (Yu) Zhang, Miao Yuan, Wenjia Wang, Peter Luong, Turker Sengoz and Rahul Chandrakant Sable for their assistance in machining and experiment.

I would also like to thank my parents: Ping Li and Hong Tian and all my friends for their love, care, and patience throughout my life.

Table of Contents

List of Figures

List of Tables

Nomenclature

NES	Nonlinear energy sink
TMD	Tune mass damper
NVA	Nonlinear vibration absorber
PEH	Piezoelectric energy harvestor
TET	Targeted energy transfer
SMR	Strongly modulated response
LO	Linear oscillator
CX-A	Complexification averaging method
FEP	Frequency energy plot
FRP	Frequency response plot
RF	Reflex sensor
FFT	Fast Fourier transform
RMS	Root mean square
NNM	Nonlinear normal mode
SDOF	Single-degree-of-freedom
MDOF	Multi-degree-of-freedom
m_a	NES mass
m_p	Primary mass
k_1	Linear stiffness of the NES

k_3	Nonlinear stiffness of the NES
k_p	Linear stiffness of the primary mass
c_a	Damping coefficient of the NES
c_p	Damping coefficient of the Primary mass
ζ	Damping ratio
f_a	Natural frequency of the NES
f_p	Natural frequency of the primary mass
θ	Electromechanical coupling coefficient
C_s	Clamped capacitance of the PEH
R	Load resistance

Chapter 1 Introduction

1.1 Motivation and overview of the research

Vibration exists in many mechanical systems. The excessive vibration usually is undesired and harmful. Examples of unwanted vibration include noise in airplanes, unbalanced motors, the response of buildings to an earthquake or the response of a car on a rough road surface. Therefore, researchers and engineers have made efforts to control vibration. In general, vibration can be controlled by the four methods: (a) proper design through stiffening, softening or damping, (b) passive control, (c) semi-active control, and (d) active control.

A vibration absorber or a tuned mass damper (TMD) is one of the passive vibration control devices to suppress vibration of a primary system subjected to a harmonic excitation. The TMD is very effective if the exciting frequency is constant. However, the TMDs' performance deteriorates if the exciting frequency varies. Therefore, the major shortcoming of the TMD is a narrow operating band width.

This study is concerned with two kinds of vibration of a primary system: (1) transient responses to initial disturbance and (2) steady state responses to harmonic base excitation. Figure 1.1 shows the schematic of these two vibration problems where m_p, k_p, and c_p are the mass, stiffness and damping coefficient of the primary system, respectively; $x_p(t)$ is the absolute displacement of the primary structure in Figure 1.1 (a) and the relative displacement of the primary mass in Figure 1.1 (b); and $y(t)$ is the displacement of the base.

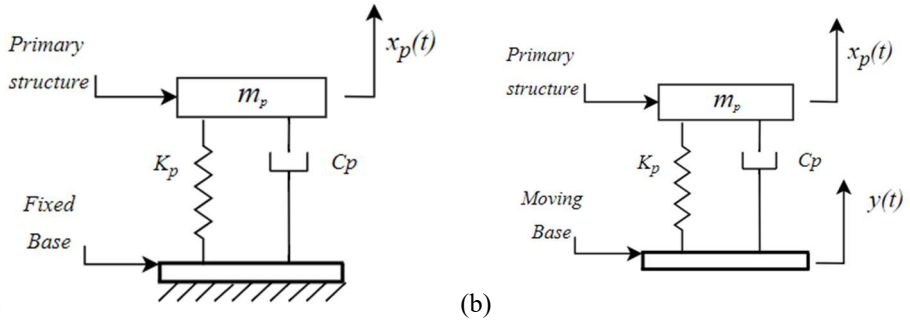

Figure 1.1 Schematic of two common vibration problems: (a) transient response; (b) harmonic base excitation.

For the transient response of the system shown in Figure 1.1 (a), the equation of motion is given by

$$\begin{cases} m_p\ddot{x}_p + c_p\dot{x}_p + k_p x_p = 0 \\ x_p(0), \dot{x}_p(0) \end{cases} \tag{1.1}$$

$$f_n = \frac{1}{2\pi}\sqrt{\frac{k_p}{m_p}},\ \zeta = \frac{c_p}{2\sqrt{k_p m_p}} \tag{1.2}$$

where x_p, $\dot{x}_p$ and $\ddot{x}_p$ are the displacement, velocity and acceleration of the primary structure, respectively; $x_p(0)$ and $\dot{x}_p(0)$ are the initial displacement and initial velocity; and f_n is the natural frequency of the primary system.

Figure 1.2 shows a typical transient response for the system with a low damping coefficient. The initial displacement and the initial velocity are set to $x_p(0)$ = 0.005 m and $\dot{x}_p(0) = 0$ m/s, respectively. As shown in Figure 1.2, the oscillation of the system attenuates over a long time. The vibration with this extended duration is undesirable.

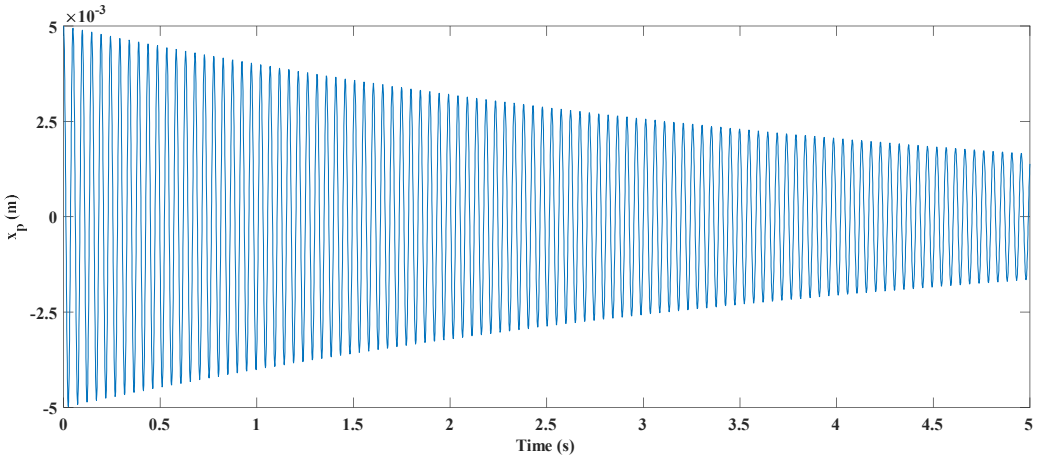

Figure 1.2 Transient response of the primary system: m_p=0.324 kg, k_p=5417.5 N/m, and ζ= 0.017.

For the system shown in Figure 1.1 (b), the equation of motion is defined by

$$\begin{cases} m_p\ddot{x}_p + c_p x_p + k_p x_p = -m_p\ddot{y} \\ \ddot{y} = A_y \cos(\Omega t) \end{cases} \tag{1.3}$$

where A_y = -$\Omega^2 Y$ is the acceleration amplitude, Ω is the excitation frequency, and Y is the amplitude of the base motion. As shown in Equation (1.3), the base excitation can be thought of as the direct excitation of the inertial force when the relative displacement of the primary mass is used. Figure 1.3 shows the system response to a linear upsweep of harmonic base excitation. Note that the response peaks around $f_n = 20.58$ Hz that is the natural frequency of the system. It should be also noted that the response to a downsweep excitation is identical to that from the upsweep excitation as the system is linear.

Energy harvesting intends to convert the mechanical energy of the vibration into electrical energy. For instance, these papers [1, 2] studied the vibration energy harvesting. Since vibration suppression involves the dissipation of energy, it is then of interest to investigate simultaneous vibration and energy harvesting. This thesis will focus on finding a way to suppress vibration and collect useful energy at the same time. The motivation of this research is to develop an apparatus for a brandband vibration suppression and energy harvesting.

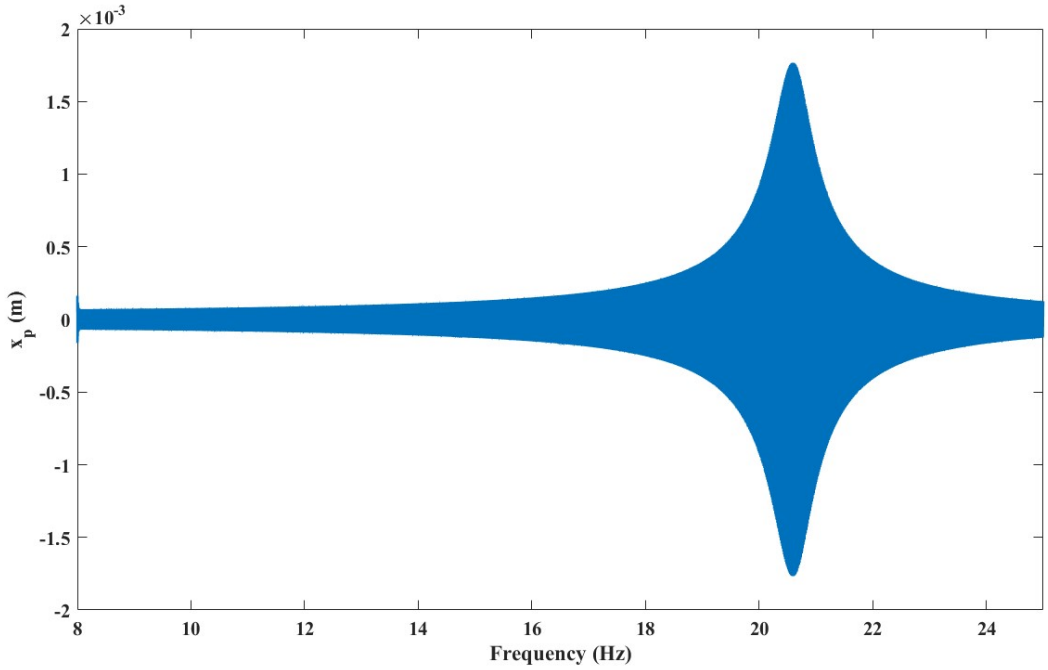

Figure 1.3 The harmonic response for the system with the natural frequency f_n = 20.58 Hz.

1.2 Literature review

1.2.1 Nonlinear energy sink

Passive vibration suppression has been studied by many researchers in the past [3, 4, 5, 6, 7, 8, 9]. Figure 1.4 (a) shows an example of passive vibration control where m_a, k_1 and c_a are the mass, linear stiffness and damping coefficient of the vibration absorber, respectively. As pointed previously, the major shortcoming of the vibration absorber is a narrow operating bandwidth. Instead, nonlinear energy sinks (NESs) have been proved to perform effectively in a wide frequency region [10]. The NES is a special type of nonlinear vibration absorber (NVA). In particular, the NES consists of a small mass, a spring with an essentially nonlinear stiffness and a viscous damper [9].

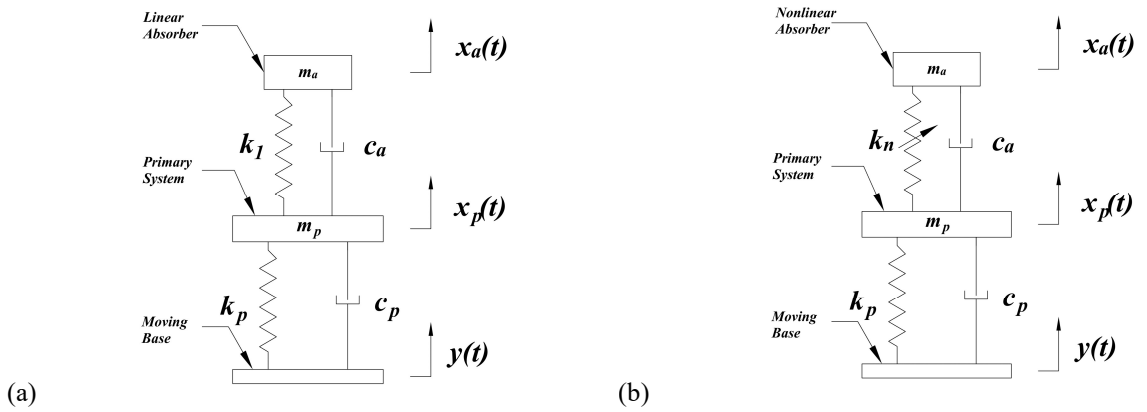

Figure 1.4 Schematic of a primary system attached by a vibration absorber with the harmonic base excitation: (a) a linear vibration absorber; (b) a nonlinear vibration absorber.

Figure 1.4 (b) shows the primary system attached by a nonlinear vibration absorber where the stiffness k_n represents a linear stiffness term k_1 and a nonlinear stiffness term k_3. In this case, the nonlinear restoring force of the absorber spring can be defined as a cubic function $F = k_1 z + k_3 z^3$, where z is the relative displacement between the absorber mass and primary mass. On the other hand, the restoring force of the NES's spring is defined by a pure cubic term $F = k_3 z^3$. The lack of the linear stiffness means that the NES can respond to any frequency as long as the excitation is sufficiently strong. Hence an NES is preferable to an NVA in terms of broadband performance. These studies [11, 12, 13] proved the effectiveness of the NES. In other research [14, 15], a linear oscillator (LO) coupled to an NES was studied by considering the underlying Hamiltonian system. In this system, the vibrational energy of the LO is efficiently absorbed by the NES. Such a setup with passive energy transformation can be presented as the so-called passive energy pumping or the targeted energy transfer (TET). Energy pumping or TET is defined as a one-way irreversible energy transformation from a linear primary system to a nonlinear attachment [16, 17, 18]. Moreover, the mentioned Hamiltonian systems were involved in the 1:1 internal resonance [10]. The 1:1 internal resonance is a particular concept that both the LO and NES process an equal dominant frequency. In [15], the author examined the resonance capture of a strongly nonlinear

and weakly damped two-degree-of-freedom system by numerical analysis. When the system is involved in the 1:1 resonance manifold, energy pumping is presented.

Many papers [19, 20, 21, 22, 23, 24, 25, 26, 27, 28] showed that the unwanted vibrational energy in the primary structure could be purposely transferred to the local essentially nonlinear attachment. In [29, 30], the authors explained the robustness and benefit of an NES with the absence of a linear stiffness. Moreover, these two studies found that an initial energy level is required to activate the NES. As long as the initial level of energy is higher than a certain energy threshold, the NES is engaged into the TET and the system reaches the 1:1 resonance. In [19], the researchers investigated the effectiveness of the TET through a detailed study of the transient responses with three initial energy levels. The results revealed that the TET was not achieved at the low initial energy level while the TET was effectively achieved for the intermediate initial energy level. The study showed that the NES with the intermediate initial energy level attenuated by 90-95% of the total oscillation energy. Even though the effectiveness of the TET decreased at the high initial energy level, the NES was still significantly activated. In [20], the researchers investigated the TET behaviors using both the grounded NES configurations and the ungrounded NES configurations. The advantages and disadvantages of these two configurations were investigated. It was found that the NES was only activated with a high amplitude, and the effectiveness of the TET decreased with the increase of the critical resonant regime.

In references [31, 32, 33, 34], the steady state responses of a primary system attached with the NES under harmonic excitations were investigated. In particular, the weakly modulated response and strongly modulated response (SMR) were examined. The approximate solutions of the steady state responses were based on the complexification averaging method (CX-A) [19]. The CX-A method assumes that the dynamics of the system analysis can be performed by a slow-fast partition. The numerical results were presented by the so-called frequency response plots (FRPs) [19]. The

desired bifurcation points were found, revealing the existence of multiple periodic solutions and the interesting SMR. Similar to transient response, the SMRs can be regarded as a repetitive TETs.

In practice, it is very challenging to realize an essentially nonlinear stiffness in the NES. The NES design in [35] achieved an essentially nonlinear stiffness by two coil springs attached to a small mass. The other ends of the two coil springs are connected to the pivots. If the springs are free of tension, a pure cubic stiffness is produced by the geometric nonlinearity. However, a rail guide is used to support the NES mass. The studies reported in [36, 37, 38] constructed an NES by using two thin steel wires to suspend a small mass. In order to reduce the pre-tension in the wires, the NES mass is supported on an air track, resulting in the linear stiffness of 11.3 N/m and the nonlinear stiffness of 1.83×10^7 N/m^3. In [39], the NES was made by a visco-elastic membrane by setting constant air pressure. The pre-stress caused large amplitude oscillations of the membrane. Thus, there was a normalized pre-stress parameter χ that was used to introduce an approximated zero linear stiffness. An experimental study was conducted in [40] to identify the nonlinear performance of the Vibro-Impact NES (VI-NES). The study conducted in [10] introduced the Magnetic-Strung NES (MS-NES). A magnet NES with two strings was set between two outer magnets on the primary system resulting in the nonlinear force.

Dr. Kefu Liu's research group has focused on simultaneous vibration suppression and energy harvesting using a variant NES [41, 42, 43, 44]. Different from the previous NES design, these devices were not essentially nonlinear. In Kremer's research [41, 42], the proposed NES consisted of a clamped beam and fixed repelling magnets, resulting in a low mechanical damping, a low linear stiffness, and a high nonlinear stiffness. The proposed NES acted similarly as the true NES. In Zhang's research [43], the NES beam was transversely preloaded to be nearly buckled to achieve quasi essentially nonlinear stiffness. In Xiong's study [44], a cantilever beam with fixed repelling magnets was mounted vertically to process a weak linear stiffness and strong nonlinear stiffness.

1.2.2 Energy harvesting

In the last decade, the energy harvesting [45] has been receiving much attention. The sources available for energy harvesting include the following types: light, radio-frequency electromagnetic radiation, thermal gradients, and motion. Based on the sources, there are many useful applications [46, 47]. For example, solar cells are the typical energy harvesting solution; thermoelectric generation is a solution for accumulating the thermal energies; piezoelectric energy harvester (PEH) is a method to harvest ambient vibration energy by the piezoelectric effect.

In the mechanical engineering field, vibrational energy can be converted to electric energy. Two common electromechanical transduction methods are the electromagnetic induction [48, 49, 50] and piezoelectric effect. In [51], a micro-electromagnetic energy harvester was investigated. The main structure consists of an electroplated copper planar spring, a permanent magnet, and a copper planar coil. The device is able to produce a voltage of 18 mV and output power of 0.61 μW. On the other hand, piezoelectric energy harvester (PEH) [52, 53, 54, 55] has been studied by many researchers. The advantages of the PEH are a high power generation per volume and wide working bandwidth. A typical piezoelectric energy harvester consists of a cantilever beam attached to a piezoelectric ceramic and an inertia mass on the end of the beam [56, 57]. In [58, 59] researchers investigated cantilevered beams with piezoceramic layers under harmonic base excitations. In the present study, a PEH is combined with a variant NES to realize the goal of vibration suppression and energy harvesting.

1.3 Objectives of the research

This study intends to continue the works reported in [41, 42, 43, 44]. The main theme is to seek a variant NES that possesses a low linear stiffness and high nonlinear stiffness for the purpose of simultaneous vibration suppression and energy harvesting. The objectives of this work are defined as follow: (1) to design three apparatuses that are capable of emulating the characteristics

of the NES; (2) to identify the parameters of the developed variant NESs and the parameters of the two developed primary systems; (3) among the three apparatuses, to select one apparatus that best emulates a true NES; (4) to investigate the transient responses of the weakly coupled system and strongly coupled system; and (5) to investigate the steady states responses of the weakly coupled system and strongly coupled system under harmonic base excitation.

1.4 Thesis outline

The rest of the thesis is organized as follows. Chapter 2 introduces the three proposed apparatuses of the variant NES and presents the identification of their parameters. Based on the testing results, one variant NES is selected for further study. Chapter 3 focuses on the transient responses of the two systems: the weakly coupled system and strongly coupled system. Chapter 4 concentrates on the harmonically forced responses of the two coupled system. Finally, Chapter 5 summarizes the main findings of this research and gives suggestion for the future work.

Chapter 2 Apparatus Development and System Characterization

This chapter focuses on the development of an apparatus that can be used to study simultaneous vibration suppression and energy harvesting. First, the system under consideration is introduced, which consists of a primary system attached with a nonlinear energy sink (NES). Then three variant NES designs are proposed. Finally, system characterization is conducted to determine the best variant NES among the three proposed designs. This lays a foundation for the next phase of investigation of this study.

2.1 Introduction

Figure 2.1 shows the schematic of a primary system with a nonlinear energy sink (NES) being attached where m_a, k_n and c_a are the mass, nonlinear stiffness and damping coefficient of the NES respectively; m_p, k_p and c_p are the mass, stiffness and damping coefficient of the primary system, respectively; $x_a(t)$ and $x_p(t)$ represent the displacement of the NES mass and primary mass, respectively; $y(t)$ represents the displacement of the base. As discussed in Introduction, realization of a true NES is rather challenging as it requires an essential nonlinear spring.

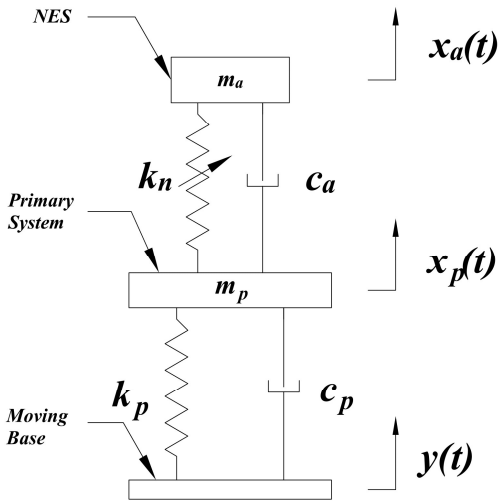

Figure 2.1. Schematic of a primary system attached by an NES.

The previous study [43] has shown that a nonlinear vibration absorber (NVA) can behave in a way similar to an NES if it meets two conditions: a strong nonlinearity and a weak coupling between the NVA and the primary system. An NVA that realizes these two conditions is referred to as a variant NES in this study. In what follows, the study is focused on developing a system consisting of a primary system and a variant NES.

2.2 The Proposed Apparatus

An apparatus is required in order to study simultaneous vibration suppression and energy harvesting. The desired apparatus should consist of a primary system and a variant NES. Figure 2.2 shows three proposed designs for the apparatus. All three designs consist of a primary system and a variant NES. The primary system is formed by clamping the primary block and the base block by four thin steel plates which act as the primary spring. The variant NES is formed by the cantilever beam and the mass attached at the free end of the beam. The beam length and mass are chosen to keep its natural frequency as low as possible.

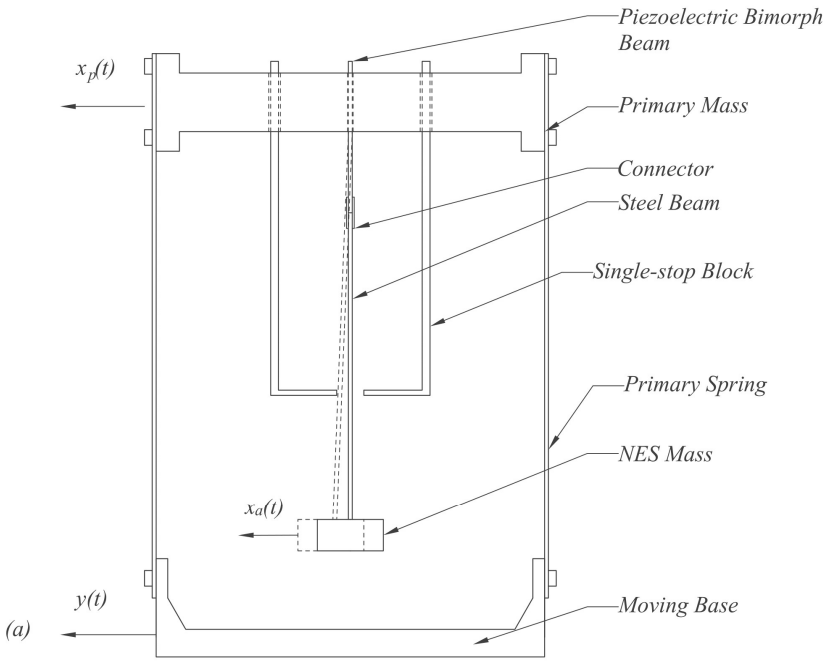

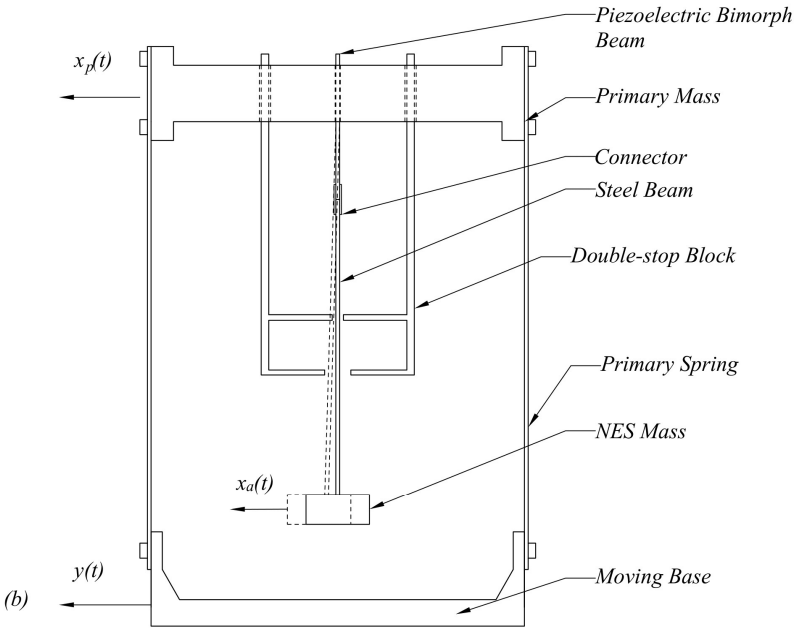

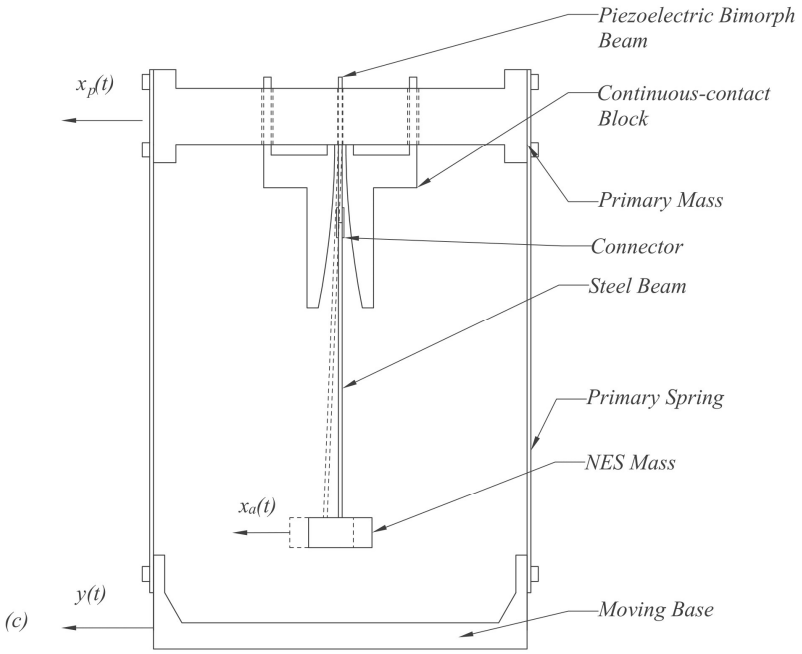

Figure 2.2. Schematic of the three designs: (a) single-stop blocks; (b) double-stop blocks; (c) quadratic-curved blocks.

To harvest energy, the cantilever beam is composed of a thin steel plate and a piezoelectric energy harvester (PEH) (PPA-2011, PPA Piezo Protection Advantage). Three different ways are used to enhance the system nonlinearity. In Figure 2.2 (a), two L-shape blocks named single-stop blocks are used. If the magnitude of the transverse motion of the beam exceeds the gap between the beam and the blocks, the beam makes contact with one of the blocks so that its stiffness changes suddenly. Thus the beam possesses a two piecewise linear stiffness. In Figure 2.2 (b), two upside-down F-shape blocks named double-stop block are employed so that the beam possesses a three-piece linear stiffness. In Figure 2.2 (c), two quadratic-curved blocks named as continuous-contact blocks are used to produce a continuous nonlinear stiffness. In the following section, the stiffness of each of these systems will be determined.

The testing system is shown in Figure 2.3. The base is fastened onto a slipping table that is driven by a B&K Vibration Exciter (Type 4809) through a stinger. The shaker is driven by a B&K power amplifier (Type 2718). Two laser reflex (RF) sensors (Wenglor model CP24MHT80) are used to measure the displacement of the primary mass and NES mass, respectively. A dSPACE CLP1104 data acquisition board is used to collect sensor data generated from the laser reflex sensors and voltage output generated by the PEH. The control program is developed by MATLAB Simulink and interfaced with the dSPACE Controldesk Desktop software.

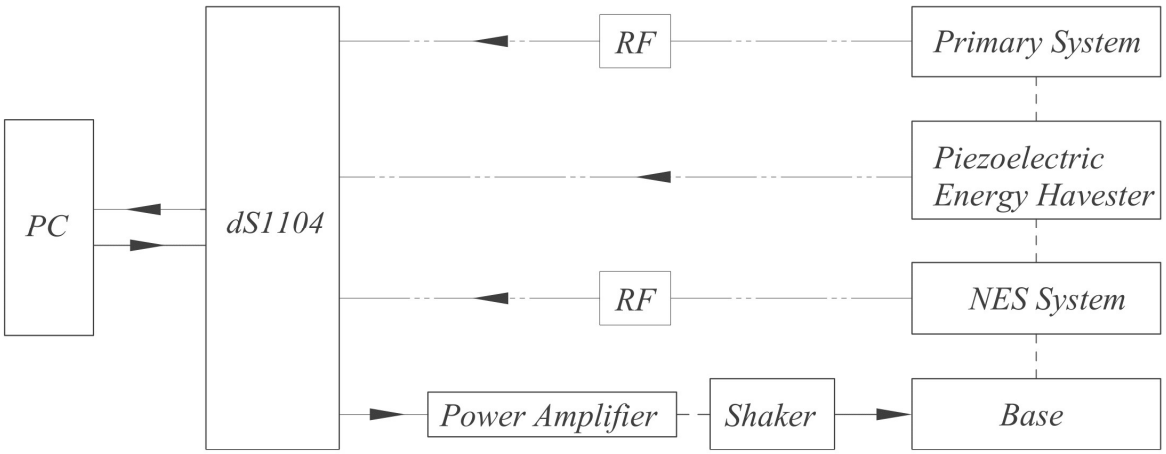

Figure 2.3. Schematic of testing system.

2.3 Identification of the Primary System Parameters

A traditional method is employed to determine the parameters of the primary system. The mass of the primary system is found to be m_p = 0.324 kg by a scale. In order to investigate different couplings between the primary system and the variant NES, two primary systems are formed by employing two sets of thin steel plates. They are obtained by cutting steel rulers with a width of 30.19 mm and a thickness of 0.53 mm. The length of the first set is 73.23 mm while the length of the second set is 156.98 mm. Thus the first primary system has a high stiffness while the second primary system has a low stiffness. To determine the stiffness of the primary system, the free response is recorded, and the natural frequency is determined from the Fast Fourier transform

(FFT) spectrum of the free response. Figure 2.4 shows the free response and its FFT spectrum from the primary system with high stiffness. The natural frequency of the primary system is found to be 20.58 Hz. Figure 2.5 shows the free response and its FFT spectrum from the primary system with low stiffness. The natural frequency is found to be 6.92 Hz. Stiffness k_p can be determined by the following equation:

$$k_p = \omega_p^2 m_p \tag{2.1}$$

The results are k_p = 5417.45 N/m for the first primary system and k_p = 611.98 N/m for the second primary system.

In order to determine the damping coefficient, the logarithmic decrement method is used. As is shown on Figures 2.4 (a) and 2.5(a), all peak values are measured. The damping ratio can be obtained by the following equations:

$$\delta = \frac{1}{n}\ln\left(\frac{x(t)}{x(t+nT)}\right) \tag{2.2}$$

$$\zeta = \frac{\delta}{\sqrt{4\pi^2 + \delta^2}} \tag{2.3}$$

$$c_p = 2\zeta(2\pi f_p)m_p \tag{2.4}$$

where $x(t)$ is the peak of the response at time t, $x(t+nT)$ is the peak of the response at time $t+nT$ with T as the natural period, and ζ is the damping ratio. By using Equation (2.3) and Equation (2.4), the damping ratio for the first primary system is found to be $\zeta = 0.016883$ while the damping ratio for the second system is found to be $\zeta = 0.02035$. Using the found damping ratio and Equation (2.4), the damping coefficients can be determined and are listed in Table 2.1.

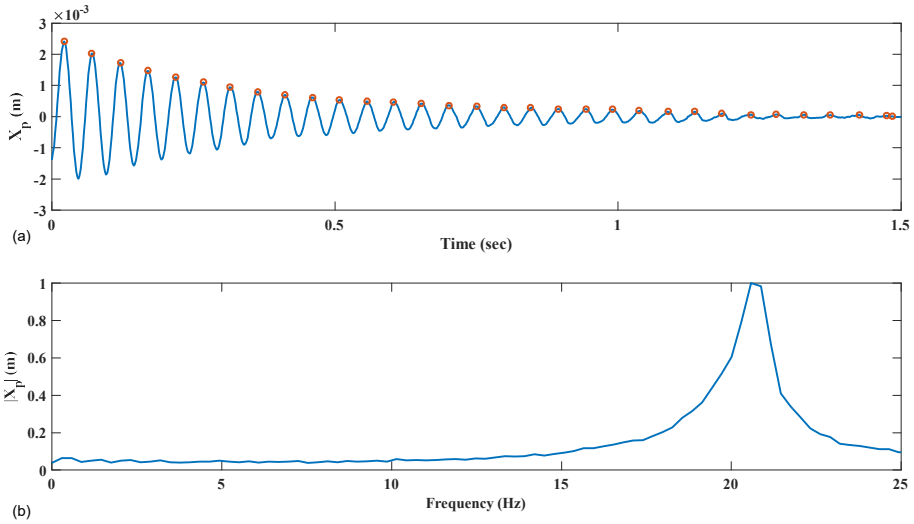

Figure 2.4. Experimental results of the first primary system: (a) Free response; (b) FFT spectrum of the response.

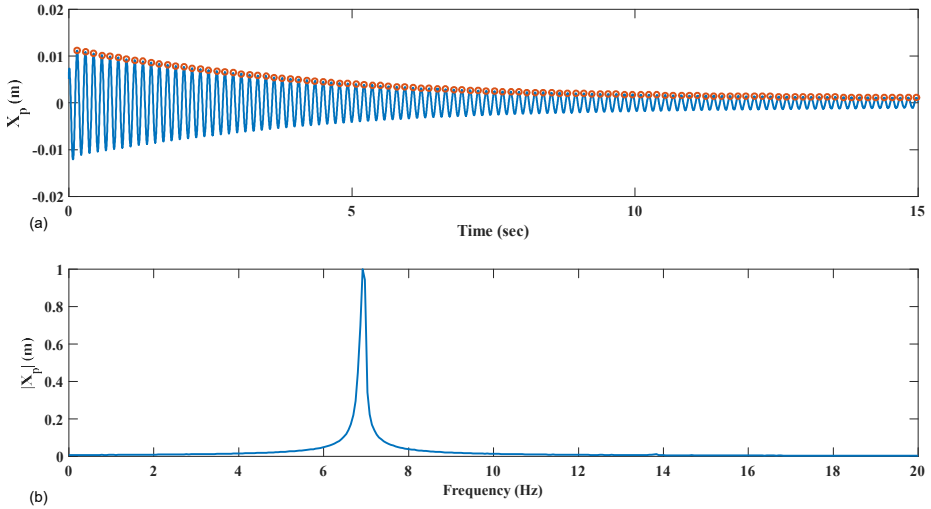

Figure 2.5. Experimental results of the second primary system: (a) Free response; (b) FFT spectrum of the response.

Table 2.1 Estimated parameter values of the primary system

Stiff Primary System		*Flexible Primary System*	
Parameter	Estimated value	Parameter	Estimated value
m_p	0.324 kg	m_p	0.324 kg
k_p	5417.45 N/m	k_p	611.98 N/m
c_p	1.983 Ns/m	c_p	0.131 Ns/m
f_p	20.58Hz	f_p	6.917Hz
ζ	0.025	ζ	0.004

2.4 Characterization of Nonlinear Springs of the Proposed Variant NESs

Figures 2.6, 2.7 and 2.8 show the setups used to determine the nonlinear stiffness for each of the proposed variant NESs. In all setups, a rigid frame is constructed by connecting the primary block and base block by two rigid plates. The cantilever beam is constructed by connecting the piezoelectric energy harvester and steel ruler by the connector. The two magnets are attached to the end of the beam by the magnet holder.

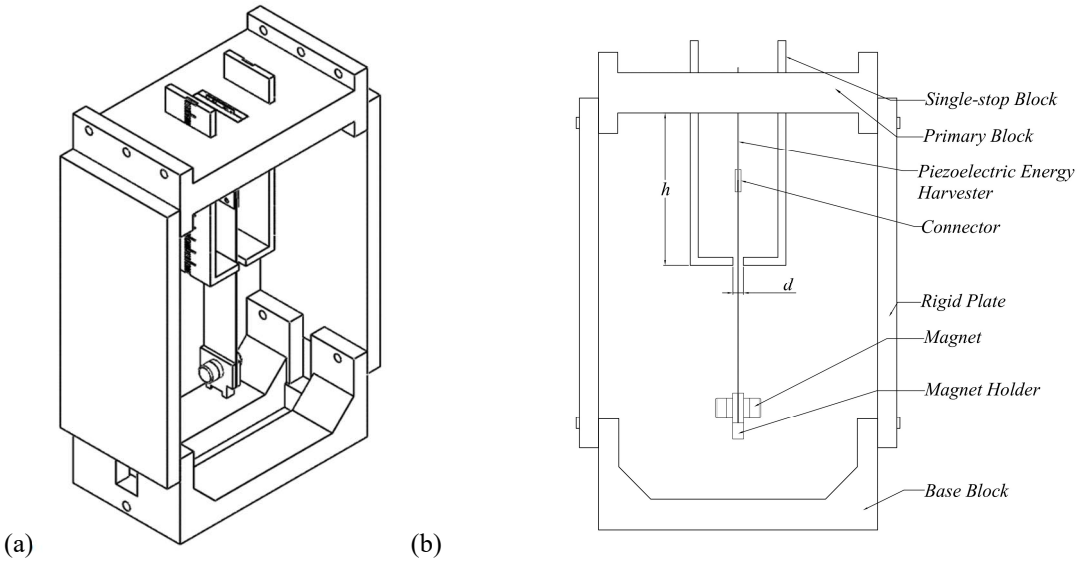

Figure 2.6. Schematic of the developed model with the single-stop blocks: (a) Isometric view; (b) Front view.

Figure 2.6 shows the developed model that employs the single-stop blocks. The configuration of the single-stop blocks is specified by height *h* and gap *d*.

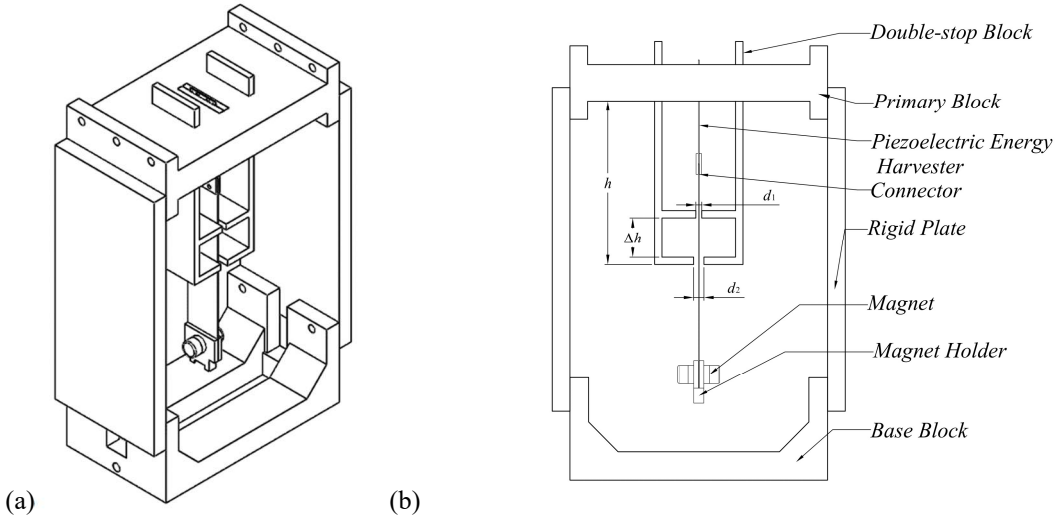

Figure 2.7. Schematic of the developed model with the double-stop blocks: (a) Isometric view; (b) Front view.

Figure 2.7 illustrates the developed model that employs the double stop-blocks. In this case, the configuration of the double-stop blocks is specified by height *h*, and gaps Δh, d_1 and d_2, respectively.

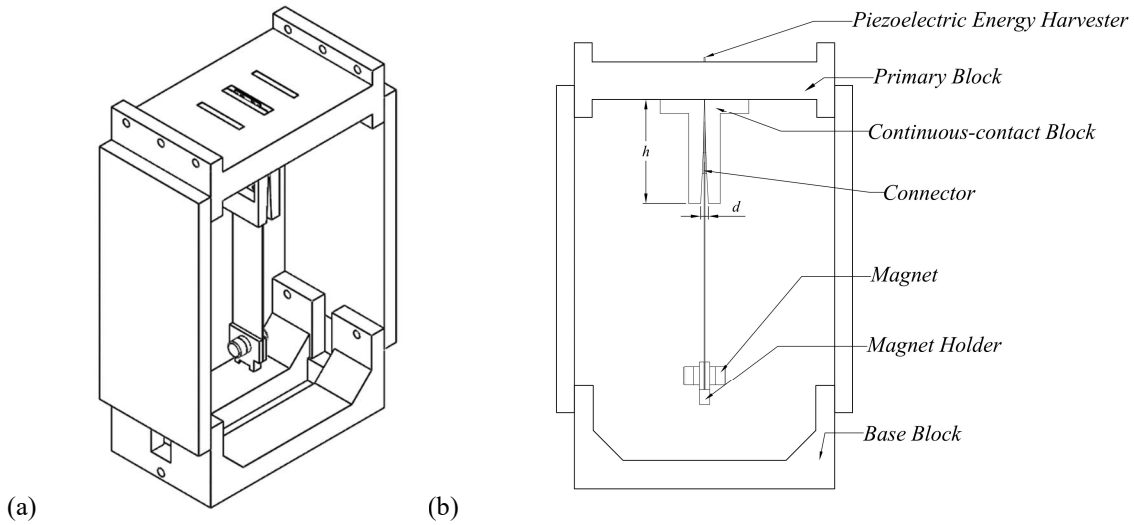

Figure 2.8. Schematic of the developed model with the continuous-contact blocks: (a) Isometric view; (b) Front view.

Figure 2.8 shows the developed model that employs the continuous-contact blocks. The configuration of the continuous-contact blocks is specified by height *h* and gap *d*.

The three systems can be represented by the model shown in Figure 2.9 where m_a is the NES mass, c_a is the mechanical damping coefficient of the NES system, k_n is the nonlinear stiffness of the NES spring, $y(t)$ and $x_a(t)$ are the displacements of the base and NES, respectively.

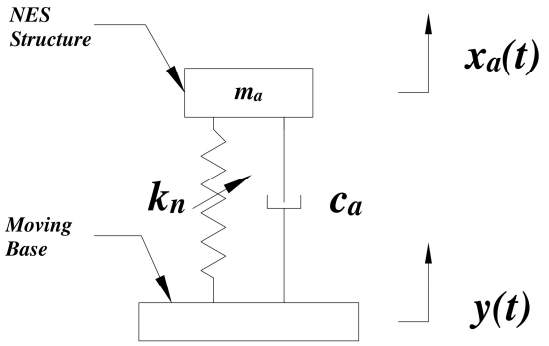

Figure 2.9. Schematic of equivalent SDOF system

The equation of motion for the system and the dynamics of the PEH circuit can be defined by [43]:

$$m_a\ddot{x}_a + c_a\dot{z} + k_1 z + k_3 z^3 + \theta V = 0 \tag{2.5}$$

$$\frac{V}{R} + C^s\dot{V} - \theta\dot{z} = 0 \tag{2.6}$$

where $\dot{z} = \dot{x}_a - \dot{y}$ is the relative velocity, $z = x_a - y$ is the relative displacement; $f(z)$ is the restoring force of the nonlinear spring; θ is the electromechanical coupling coefficient of the PEH; V is the voltage across the resistor R that is used to close the circuit of PEH; C^s is the capacitance of the PEH. As the value of the term θV is very small, Equation (2.5) can be simplified as

$$F(z,\dot{z}) = -m_a\ddot{x}_a \tag{2.7}$$

where $F(z,\dot{z}) = c_a\dot{z} + k_1 z + k_3 z^3$, the NES mass is found to be m_a = 0.023 *kg*.

To determine the linear stiffness k_1 and damping coefficient c_a of the NES systems, a free response is induced by gently tapping the NES mass without the stop blocks in place. Figure 2.10 (a) shows a typical free response while Figure 2.10 (b) gives its FFT spectrum. The natural frequency is found to be $f_a = 4.281$ Hz. The linear stiffness is then found to be $k_1 = 16.64$ N/m by Equation (2.8).

$$k_1 = m_a(2\pi f_a)^2 \tag{2.8}$$

The damping ratio is ς = 0.011, and damping coefficient can be found by the following equation (2.9) to be c_a = 0.014 Nm/s

$$c_a = 2\zeta(2\pi f_a)m_a \tag{2.9}$$

The parameter value found in this section are tabulated in Table 2.2.

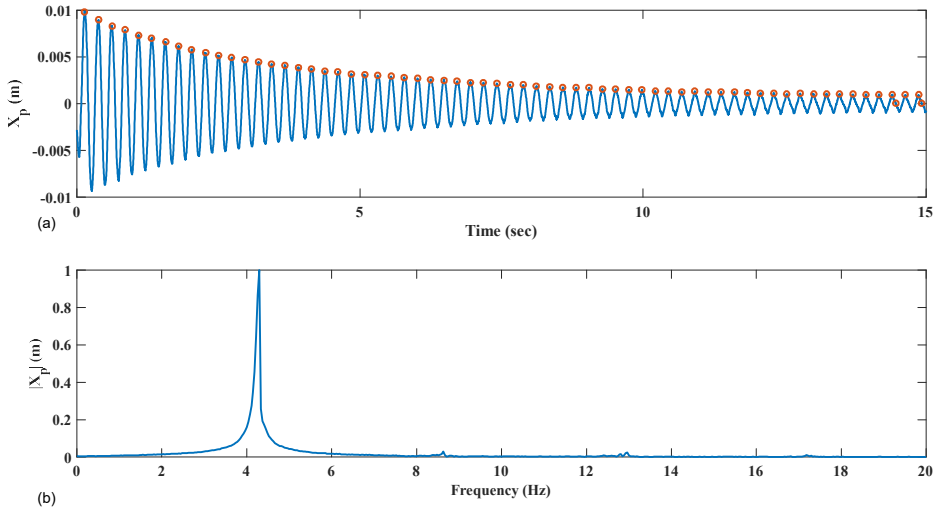

Figure 2.10. Experimental results of the NES system without the stop blocks: (a) Free response; (b) FFT spectrum of the response.

Table 2.2 Estimated parameter values of the NES system

Parameter	Estimated value
m_a	0.023 kg
k_1	16.64 N/m
c_a	0.014 Ns/m
f_a	4.281Hz

2.5 Comparison of the Three Variant NESs

The nonlinear stiffness of each of the three proposed NESs is determined by the force surface method. A 3-dimensional plot of $F(z,\dot{z})$ vs. z and $\dot{z}$ is referred to as the force surface [60, 61]. If $\dot{x}_a$, z and $\dot{z}$ are available at discrete interval k with a sampling time Δt, there is a triplet of $z_k = z(t_k)$, $\dot{z}_k = \dot{z}(t_k)$, and $F(z_k, \dot{z}_k)$ where $t_k = (k-1)\Delta t$. Using the method outlined in [61], these data can be mapped to the phase plane. The phase plane is then divided into small square

grids. The forces lying within each grid are averaged to give the force value for the center of the grids. The process is repeated until no new square grid is produced. This generates an average force map in the phase plane for the variant NES, which can be used to identify the restoring force of the NES spring. Based on the previous studies [43, 41], two important requirements to ensure the accuracy of the force surface method are the way to excite the system and the calculation of the velocity and acceleration data. The excitation signal should be rich enough so that the response signals cover fully the phase plane. Thus a modulated periodic signal is used to excite the base. The signal is determined by the following equation:

$$y(t) = Y\cos(0.1\pi t)\cdot\cos(2\pi f_e t) \tag{2.10}$$

where f_e is the exciting frequency that will be selected by trial-and-error. For results presented within this section, the displacement signals of the base and NES mass are recorded for 200 seconds with the laser reflex (RF) sensors. The velocities and accelerations are obtained by numerical differentiation. Numerical differentiation is very susceptible to noise presented in the displacement signals. To alleviate the noise amplification problem, the displacement signals are smoothened by cubic spline approximation before numerical differentiation operations.

2.5.1 Variant NES with the single-stop blocks

Figure 2.11 shows the restoring force surface as $F(z,\dot{z})$ vs. z and $\dot{z}$ obtained with f_e = 6.9 Hz. A nonlinear effect is witnessed on Figure 2.11. And the restoring force rapidly increases as displacement growth. In the meantime, the NES spring reveals a low mechanical damping, as the force surface appears flat along the velocity axis or $\dot{z}$.

The circles in Figure 2.12 show $F(z,0)$ vs. z. Clearly due to the effect of single-stop blocks, the restoring force appears as piece-wise linear stiffness. The piece-wise linear restoring force is defined by the following equations:

$$F(z,0)=\begin{cases} k_{11}z \text{ if } z<-\dfrac{b}{2} \\ k_{12}z \text{ if } -\dfrac{b}{2}\le z\le\dfrac{b}{2} \\ k_{13}z \text{ if } \dfrac{b}{2}<z \end{cases} \tag{2.11}$$

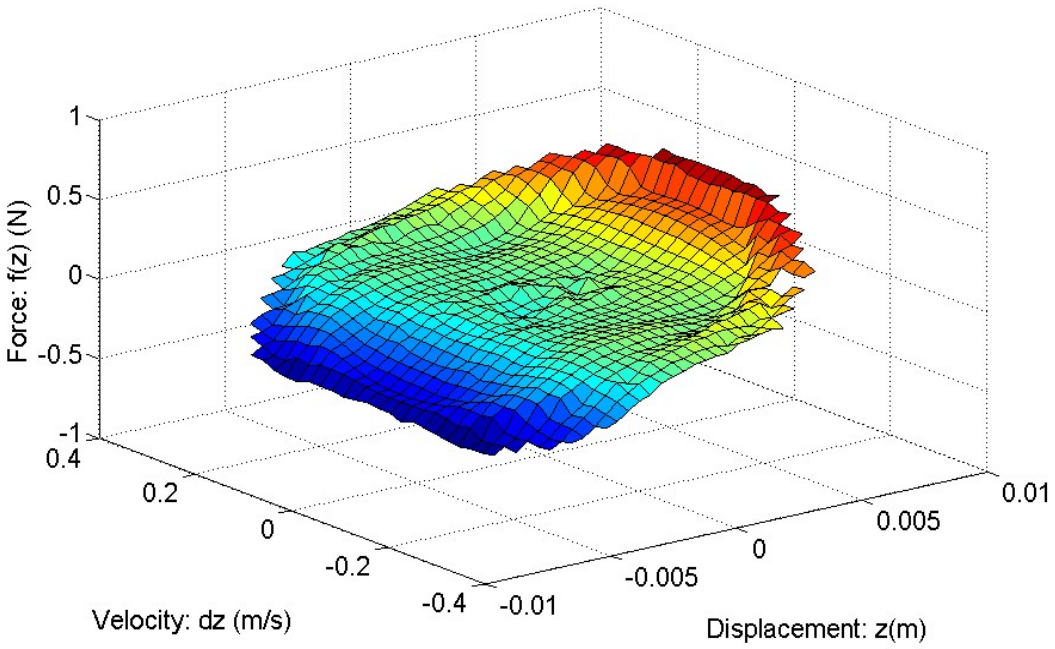

Figure 2.11. Restoring force surface with exciting frequency f_e = 6.9 Hz and height h = 0.065 m.

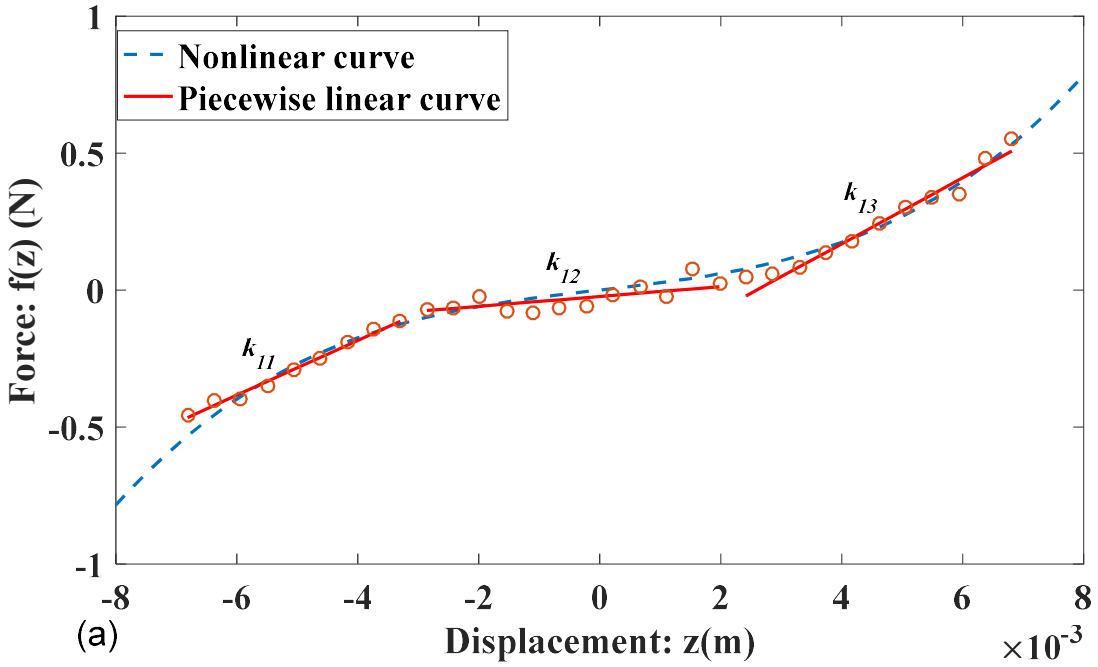
Nonlinear curve
Piecewise linear curve
Force: f(z) (N)
Displacement: z(m)
×10-3
k11
k12
k13
(a)

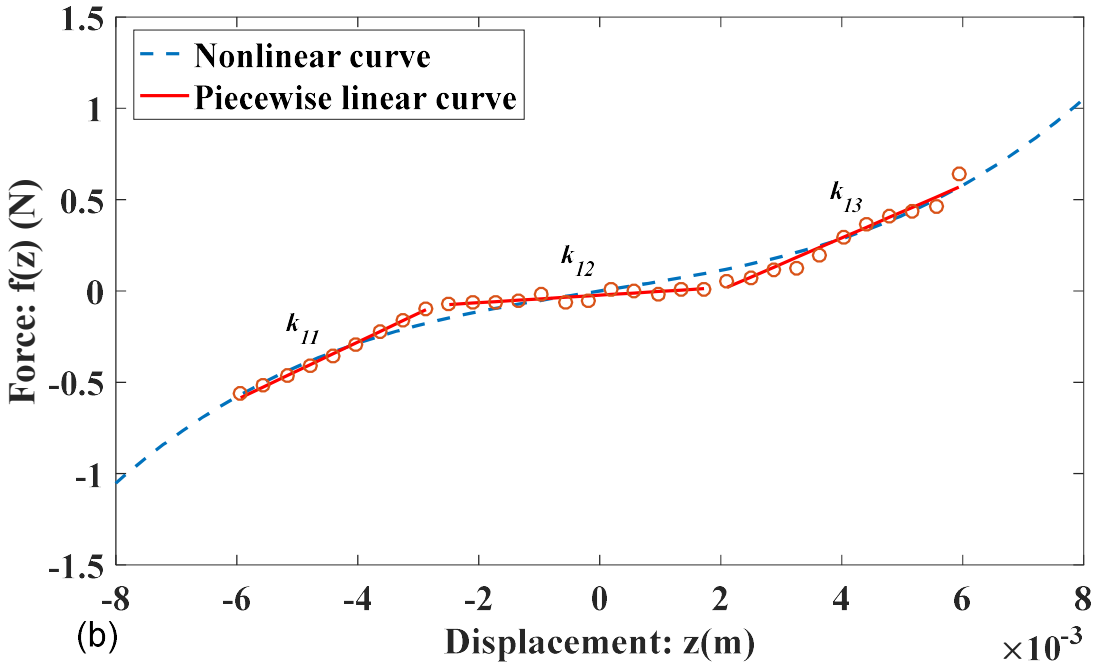
Nonlinear curve
Piecewise linear curve
Force: f(z) (N)
Displacement: z(m)
×10-3
k11
k12
k13
(b)

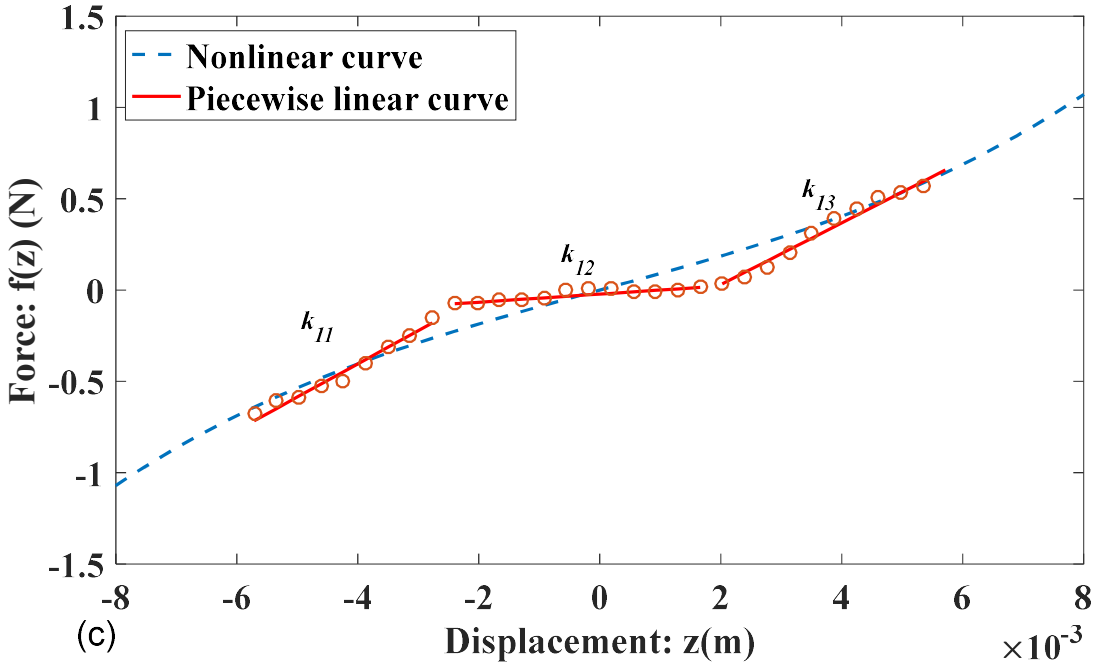

Figure 2.12. Restoring force of NES system with single-stop blocks and fixed gap d = 0.007 m: (a) h = 0.065 m; (b) h = 0.075 m;(c) h = 0.084 m.

where k_{11}, k_{12}, k_{13} are the piece-wise linear stiffnesses, and b is the clearance. It will be of interest to examine where the restoring force $F(z,0)$ can also be represented by a cubic function defined as

$$F(z,0) = k_1 z + k_3 z^3 \tag{2.12}$$

where k_1 is the linear stiffness and k_3 is the nonlinear stiffness. In Figure 2.12 the solid lines represent the best fits using Equation (2.11) while the dotted curve represents the best fits using Equation (2.12). The results in Figure 2.12 are obtained by fixing the gap as d = 0.007 m and varying the heights h.

In particular, the results in Figure 2.12 (a) is based on $h = 0.065$ m, Figure 2.12 (b) is based on $h = 0.075$ m and Figure 2.12 (c) is based on $h = 0.084$ m. The relative displacement is within $-0.008 \text{ m} < z < 0.008 \text{ m}$. It is obtained that within the region of $z = \pm 0.0025$ m the slope

of the curve is small, which results in a low linear stiffness. In the meantime, the restoring force increases quickly when the relative displacement exceeds the region of $z = \pm 0.0025$ m, which gives a high linear stiffness. According to Table 2.3 the first group is considered the best among the three different setups.

With the recorded voltage signal of the PEH, a voltage surface $V(z, \dot{z})$ vs. z and $\dot{z}$ can be obtained. From the section $V(z, 0)$, the proportional constant λ can be determined by the following equation:

$$V(z, 0) = \lambda z \tag{2.13}$$

where $\lambda = \theta / C^s$. The results are also presented in Table 2.3.

Table 2.3 Results for the NES system with the single-stop blocks.

h (m)	f_e (Hz)	k_1 (N/m)	k_3 (N/m^3)	k_{11} (N/m)	k_{12} (N/m)	k_{13} (N/m)	λ (V/m)
0.065	6.9	25.48	1.134×10^6	99.91	18.01	120.3	1257
0.075	9.0	54.02	1.001×10^6	157.3	20.59	143.1	1217
0.084	10.5	90.1	6.819×10^5	174.5	22.04	178	1169

2.5.2 Variant NES with the double-stop blocks

The configuration of the system with double-stop blocks is defined by fixing the gaps d_1 = 0.004 m, d_1 =7 mm, and Δh =2.7 mm and varying the heights. Figure 2.13 shows the force surface for the case of h = 0.066 m. The exciting frequency is chosen to be f_e = 5.8 Hz by the trial-and-error method.

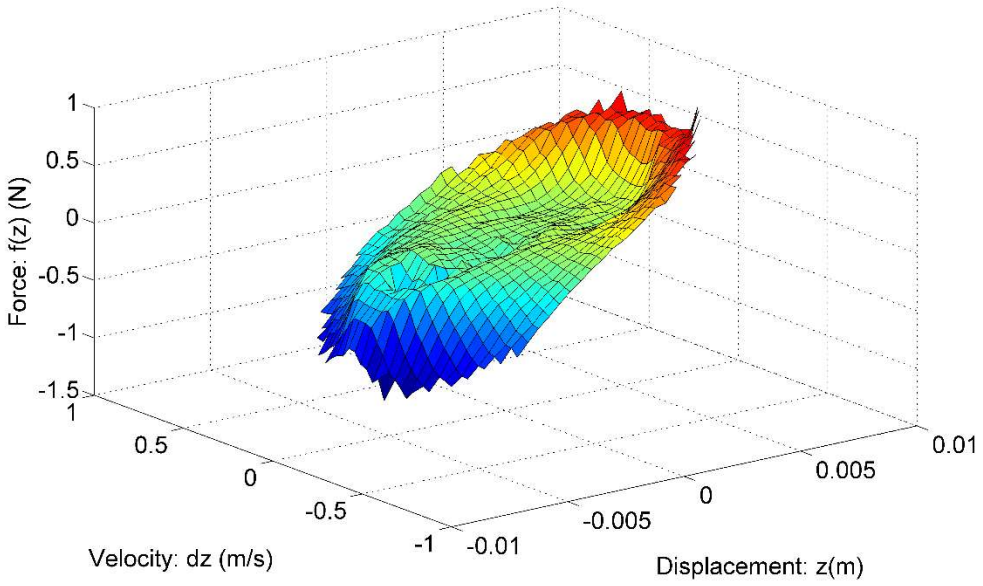

Figure 2.13. Restoring force surface with the exciting frequency f_e = 5.8 Hz and height h = 0.066 m.

The circles in Figure 2.14 shows the section of $F(z,0)$ vs. z . Clearly due to the effect of the double-stop blocks, the restoring force appears as the piece-wise linear stiffness. The piece-wise linear restoring force is defined by the following:

$$F(z,0)=\begin{cases} k_{11}z \text{ if } z<-\dfrac{b_1}{2} \\ k_{12}z \text{ if } -\dfrac{b_1}{2}\le z\le -\dfrac{b_2}{2} \\ k_{13}z \text{ if } -\dfrac{b_2}{2}\le z\le \dfrac{b_2}{2} \\ k_{14}z \text{ if } \dfrac{b_2}{2}\le z\le \dfrac{b_1}{2} \\ k_{15}z \text{ if } \dfrac{b_1}{2}< z \end{cases} \tag{2.14}$$

where k_{11}, k_{12}, k_{13}, k_{14}, and k_{15} are the piece-wise linear stiffnesses, and b_1 and b_2 are the clearances.

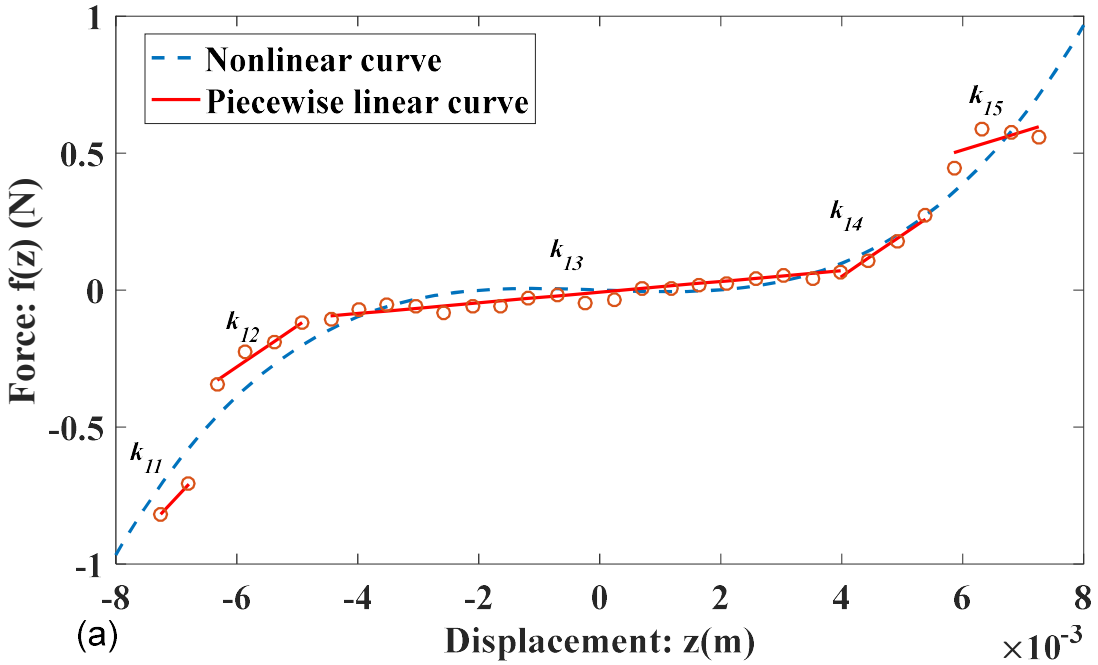
Nonlinear curve
Piecewise linear curve
Force: f(z) (N)
Displacement: z(m)
×10-3
(a)
k11
k12
k13
k14
k15

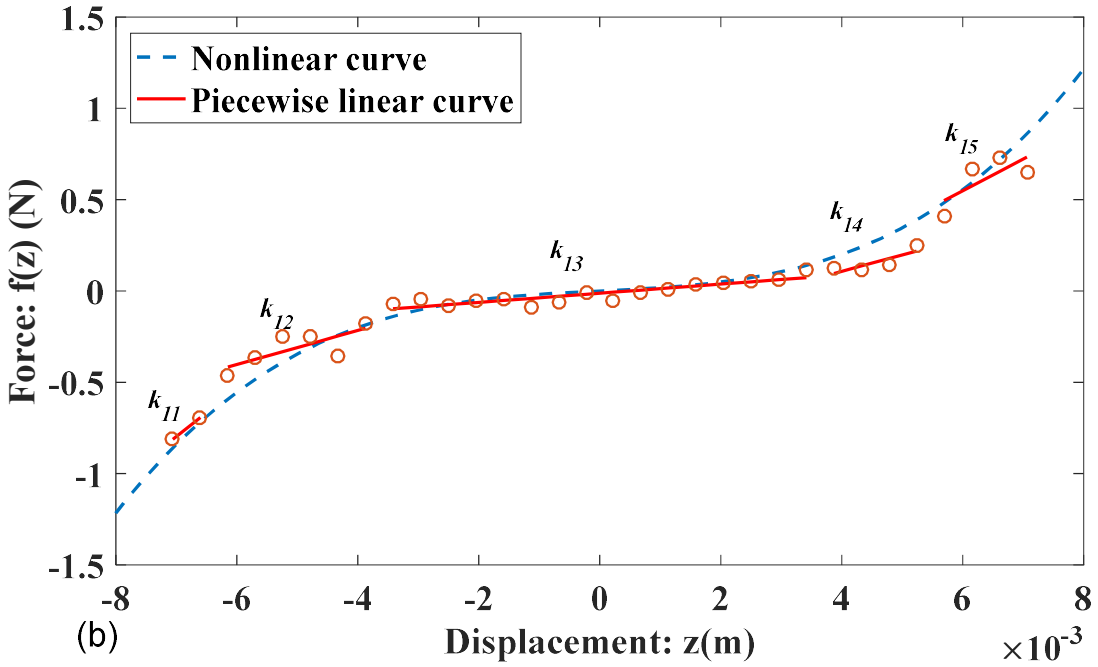
Nonlinear curve
Piecewise linear curve
Force: f(z) (N)
Displacement: z(m)
×10-3
(b)
k11
k12
k13
k14
k15

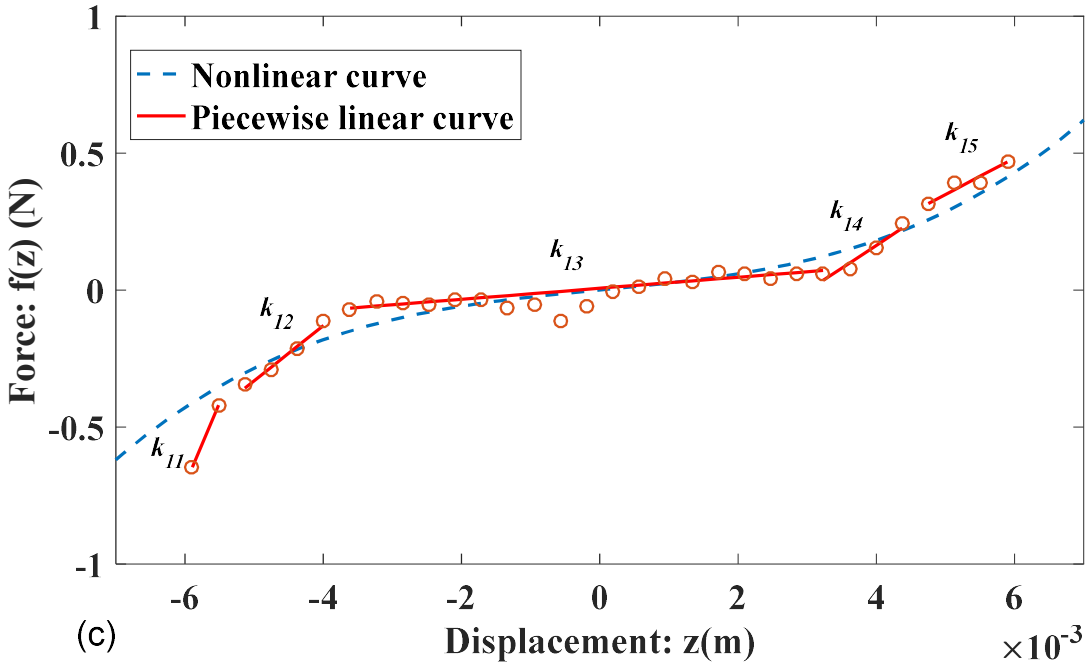

Figure 2.14 Restoring force of the NES system with the double-stop block and the two fixed gaps d_1 = 0.004 m and d_2 = 0.007 m: (a) h = 0.061 m; (b) h = 0.066 m;(c) h = 0.076 m.

In Figure 2.14, the solid lines represent the best fits using Equation (2.14) while the dotted lines represent the best fits using Equation (2.12). The results in Figure 2.14 (a) are obtained with h = 0.0604 m. The results in Figure 2.14 (b) are obtained with h = 0.066 m. The results in Figure 2.14 (c) are obtained with h = 0.076 m. The curve-fitting results are listed in Table 2.4. It is noted that if the cubic function of Equation (2.12) is used, the values of k_1 become negative for the case h = 0.0604 m. A nonlinear spring with a negative linear stiffness results in a bi-stable system that has two no-zero stable positions. Apparently, the intended variant NES should not be a bi-stable system. Thus, a different curve-fit technique is needed in order to avoid this problem. It is also noted that the piece-wise linear stiffness values by using Equation (2.14) are not symmetrical.

Table 2.4 Results for the NES system with the double-stop blocks.

h (m)	f_e (Hz)	k_1 (N/m)	k_3 (N/m^3)	k_{11} (N/m)	k_{12} (N/m)	k_{13} (N/m)	k_{14} (N/m)	k_{15} (N/m)	λ (V/m)
0.061	5.4	-7.63	2.005×10^6	235.4	149.4	19.6	150.0	67.0	1080
0.066	5.8	16	2.123×10^6	261.9	92.85	24.88	90.25	173.7	1045
0.076	6	24.38	1.308×10^6	596.1	201.1	20.1	166.8	132.6	1041

2.5.3 Variant NES with the continuous-contact blocks

The configuration of the system with the continuous-contact blocks are defined by a fixed gap d = 0.005 m and a designed height d = 0.067 m. The exciting frequency was selected to be f_e = 6.8 Hz. The force surface is shown in Figure 2.15.

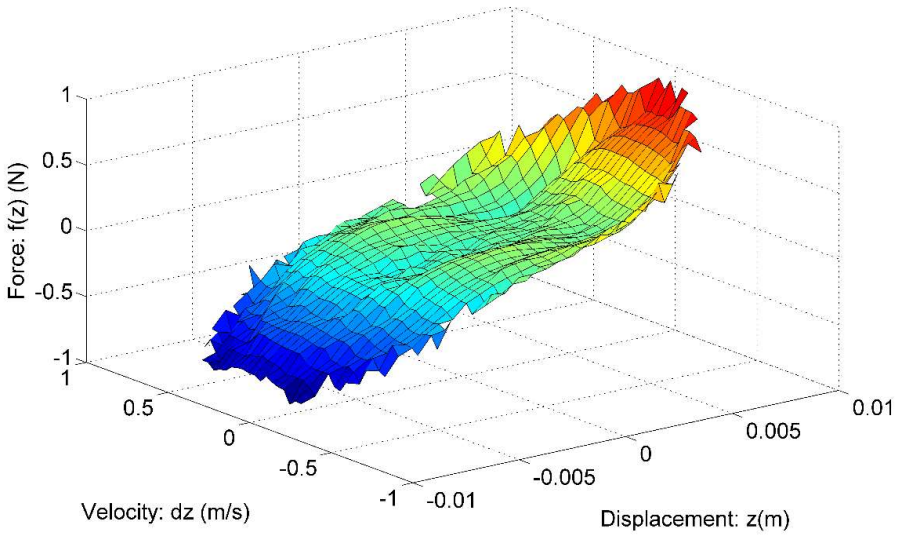

Figure 2.15. Restoring force surface with the exciting frequency f_e = 6.8 Hz and height h = 0.067 m.

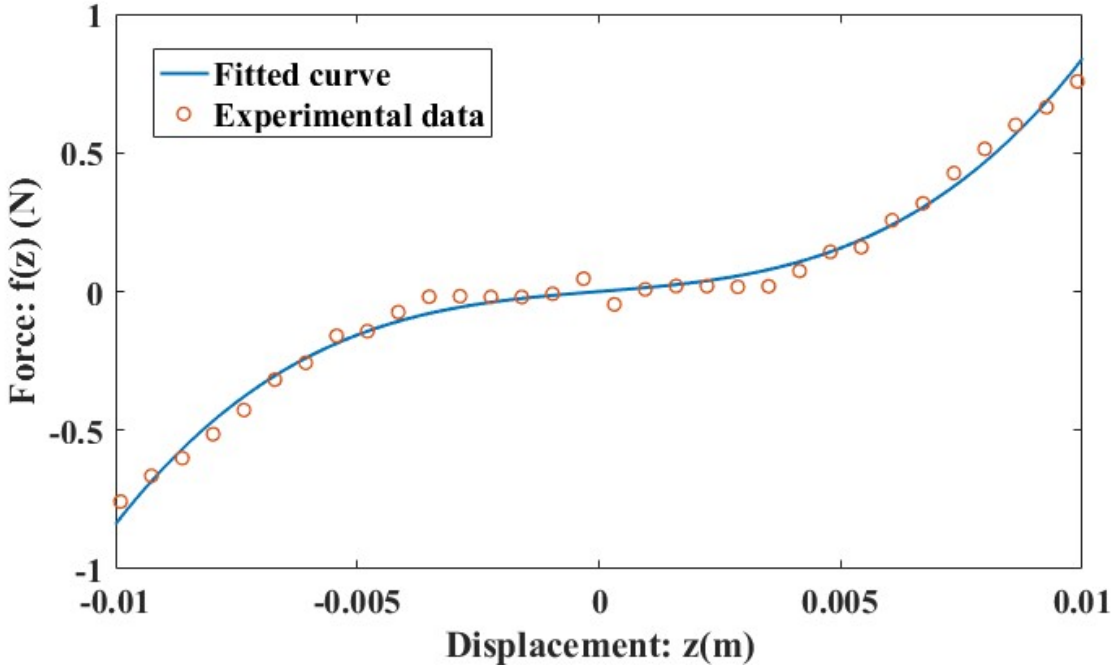

Figure 2.16. Restoring force of the NES system with the continuous-contact blocks and d = 0.005 m and h = 0.067 m.

The circles in Figure 2.16 shows $F(z,0)$ vs. z. The solid line in Figure 2.16 is the best fits by using Equation (2.12). The range of displacement is $-0.01\text{ m} < z < 0.01\text{ m}$, note that obvious 'nearly flat' portion in such range. It is also noted that the RMS values between the fitted data and experimental data is very small. The curve fitted results are listed in the Table 2.5. Compared with the results in Table 2.4, this setup results in a lower nonlinear stiffness.

Table 2.5 Results for the NES system with the continuous-contact blocks.

h (m)	f_e (Hz)	k_1 (N/m)	k_3 (N/m^3)	λ (V/m)
0.067	6.8	13.82	7.003×10^5	1051

2.6 Conclusion

This chapter has focused on the development of an apparatus for the study of simultaneous vibration suppression and energy harvesting. Two primary systems have been developed and their parameters have been identified. Three variant nonlinear energy sinks have been built. The common component of the variant NESs is a cantilever beam attached by a mass at its free end. The variation is achieved by using different stop-blocks. The nonlinear stiffness of each of the variant NESs has been determined by using the force surface method. For the NES with single-stop blocks and the NES with double-stop blocks, the restoring forces determined by the force surface method are curve-fitted by both the piece-wise linear functions and the cubic function. on the other hand, for the NES with continuous-contact blocks, the restoring force is curve-fitted by the cubic function. Comparison of the three designs reveals that the NES with double-stop blocks and h = 0.066 m is the best one as it possesses a low linear stiffness and high nonlinear stiffness.

Chapter 3 Transient Responses

3.1 Introduction

This chapter studies the transient behaviors of the variant nonlinear energy sink (NES) developed in Chapter 2. The two different primary systems have been developed in Chapter 2 (section 2.3 in particular). Attaching the NES to the primary system with the high stiffness results in a weakly coupled system, while attaching the NES to the primary system with the low stiffness results in a strongly coupled system. The transient behaviors of the two systems will be investigated by computer simulation and experiment. The focus is on comparison of the two systems in terms of achieving the targeted energy transfer (TET). TET is referred to as an irreversible transfer of mechanical energy from a linear oscillator to a nonlinear energy sink. As the variant NES used in the following study is not a true NES, it is of interest to examine the weakly coupled system's TET and the strongly coupled system's TET. In the meantime, the energy harvesting capability of the two systems is compared as well.

3.2 Simulation results with the cubic nonlinearity function

The schematic of a primary system attached by a variant NES is shown in Figure 2.1. If the NES's stiffness is defined by a cubic function, the equations of motion of the combined system are defined by:

$$m_a\ddot{x}_a + c_a(\dot{x}_a - \dot{x}_p) + k_1(x_a - x_p) + k_3(x_a - x_p)^3 + \theta V = 0 \tag{3.1}$$

$$m_p\ddot{x}_p + c_p(\dot{x}_p - \dot{y}) + k_p(x_p - y) - \left[c_a(\dot{x}_a - \dot{x}_p) + k_1(x_a - x_p) + k_3(x_a - x_p)^3 + \theta V\right] = 0 \tag{3.2}$$

where $\ddot{x}_a$, $\dot{x}_a$ and x_a are the acceleration, velocity, and displacement of the variant NES mass, respectively; x_p, $\dot{x}_p$ and $\ddot{x}_p$ are the displacement, velocity, and acceleration of the primary mass, respectively; and $\dot{y}$ and y are the velocity and the displacement of the base, respectively.

Table 3.1 lists the natural frequency f_a of the NES only, the natural frequency f_p of the primary system only, and the natural frequencies f_1 and f_2 of the combined systems for both the weakly coupled system and strongly coupled system. It can be seen that f_1 is very close to f_a and f_2 is very close to f_p.

Table 3.1 Comparison of the various natural frequencies

System	f_a (Hz)	f_p (Hz)	f_1 (Hz)	f_2 (Hz)
Weakly coupled	4.198	20.58	4.191	20.61
Strongly coupled	4.198	6.917	4.115	7.056

To generate transient responses, the following initial conditions are used: $x_p(0) = X$, $x_a(0) = X$, $\dot{x}_p(0) = 0$ and $\dot{x}_a(0) = 0$. The relative initial displacement is zero so that the total initial energy is held only in the primary system. This means that the input energy is equal to the potential energy stored in the primary system. The initial energy is computed by:

$$E_{ini} = E_{tot}(0) = E_p(0) = \frac{1}{2} k_p X^2 \tag{3.3}$$

If the damping is neglected, the total instantaneous energy $E_{NES}(t)$ in the variant NES can be obtained by:

$$E_{NES}(t) = \frac{m_a \dot{x}_a^2(t)}{2} + \frac{k_a \left[x_a(t) - x_p(t) \right]^2}{2} + \frac{k_3 \left[x_a(t) - x_p(t) \right]^4}{4} \tag{3.4}$$

And the total instantaneous energy $E_p(t)$ in the primary system is given by:

$$E_p(t) = \frac{m_p \dot{x}_p^2(t)}{2} + \frac{k_p x_p^2(t)}{2} \tag{3.5}$$

For the piezoelectric energy harvester (PEH), if a resistive load is used to close the circuit, the dynamics of the PEH circuit is defined by

$$\frac{V}{R} + C^s \dot{V} - \theta \dot{z} = 0 \tag{3.6}$$

where the accumulated energy in the PEH can be computed by numerical integration as follows:

$$E_h(t) = \int_0^t \frac{V^2(t)}{R} dt \tag{3.7}$$

where R is resistance, and $V(t)$ is the instantaneous voltage across the resistance R. When the load resistance is set as R=100 MΩ, the circuit is considered to be open.

To measure the TET, the percentage of the instantaneous energy in the NES is defined as:

$$D(t) = \frac{E_{NES}(t)}{E_p(t) + E_{NES}(t)} \times 100 \tag{3.8}$$

In what follows, the responses are generated by setting initial displacements to $X = 2.5$ mm, $X = 5$ mm or $X = 10$ mm, respectively. The initial displacement of $X = 2.5$ mm is considered to be a low-energy level. The initial displacement of $X = 5$ mm is considered to be a medium-energy level. The initial displacement of $X = 10$ mm is considered to be a high-energy level. As indicated by Equation (3.3), the initial energy level depends on the stiffness of the primary system as well. Table 3.2 lists the energy levels for both combined systems. In what follows, the transient behaviors will be examined in terms of the responses, the percentage of the instantaneous energy in the NES, and load voltages of the PEH.

Table 3.2 Initial energy levels computed by Equation (3.3)

System	Low-energy level (J)	Medium-energy level (J)	High-energy level (J)
Weakly coupled	1.69×10^{-2}	6.77×10^{-2}	2.709×10^{-1}
Strongly coupled	1.9×10^{-3}	7.6×10^{-3}	3.06×10^{-2}

3.2.1 Computer simulation with the weakly coupled system

First, the weakly coupled system is considered. Figure 3.1 and Figure 3.2 show the simulation results with the initial displacement X = 2.5 mm. As shown in Figure 3.1 (a), the primary system and the NES vibrate with significantly different amplitudes and frequencies. The frequency contents can be revealed by the wavelet transform (WT) spectrum. Figure 3.2 (a) shows the WT spectrum of the NES's response, indicating that the response is dominated by frequency close to f_1 or f_a. Figure 3.2 (b) shows the WT spectrum of the primary system's response, indicating that the response is dominated by frequency close to f_2 or f_p. Based on the difference in the response frequencies, it can be concluded that the 1:1 resonance phenomenon does not occur. However, as shown in Figure 3.1(b), even without the 1:1 resonance, the TET is established, and the energy is almost localized in the NES after 2 seconds. Figure 3.1(c) shows that the PEH is able to generate a fairly large magnitude voltage.

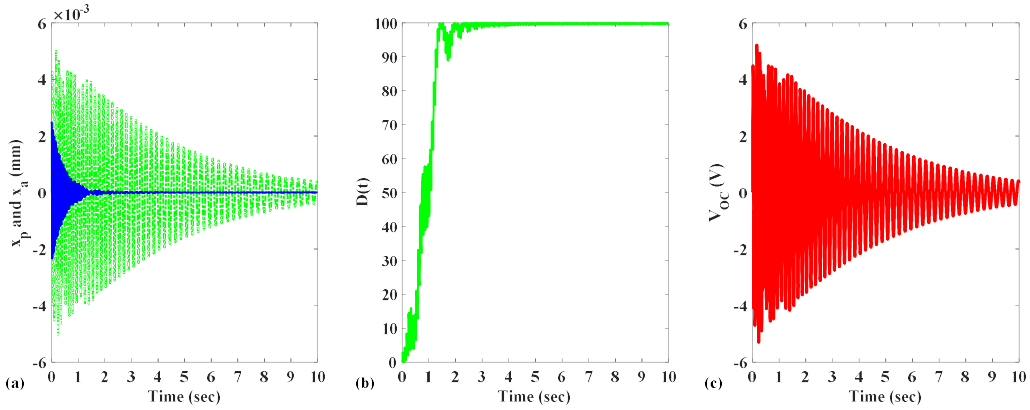

Figure 3.1 Simulation results with X = 2.5 mm: (a) displacements (solid line: primary system; dotted line: NES); (b) the percentage of the instantaneous energy in the NES and (c) open circuit voltage generated by the PEH.

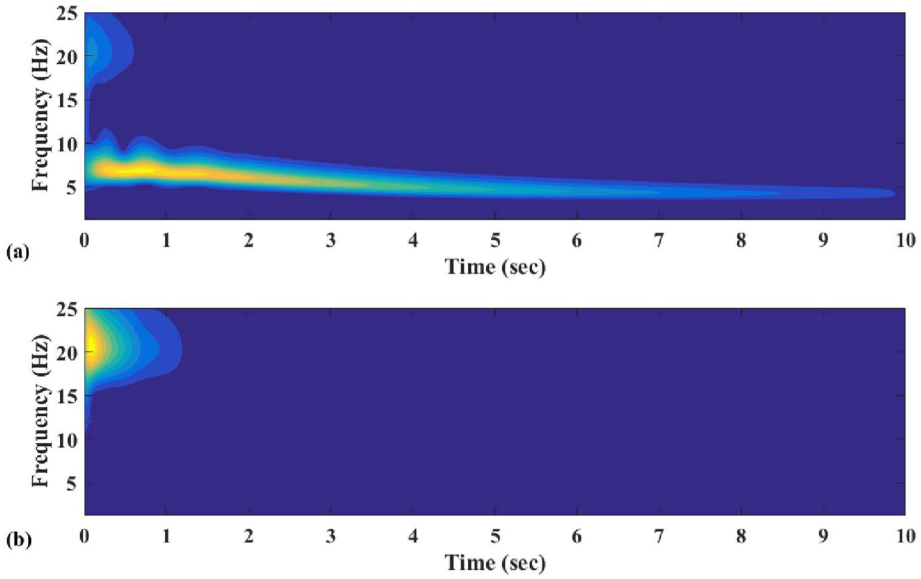

Figure 3.2 Wavelet transform spectra of the simulated responses with X = 2.5 mm: (a) x_a and (b) x_p.

Figure 3.3 and Figure 3.4 show the simulation results for the case of the medium-energy level or X = 5 mm. As shown in Figure 3.3 (a) and Figure 3.4 with increase in the initial energy, the 1:1 resonance phenomenon is established so that the NES's response becomes more nonlinear. In particular, Figure 3.4 (a) shows that in the beginning, the NES is set into an oscillation with a high frequency around f_2 or f_p, but then the response gradually sets down at a low frequency around f_1 or f_a. Shown in Figure 3.3 (b), the TET is established after 3 seconds. As a result, the PEH's voltage magnitude increases, indicated in Figure 3.3 (c).

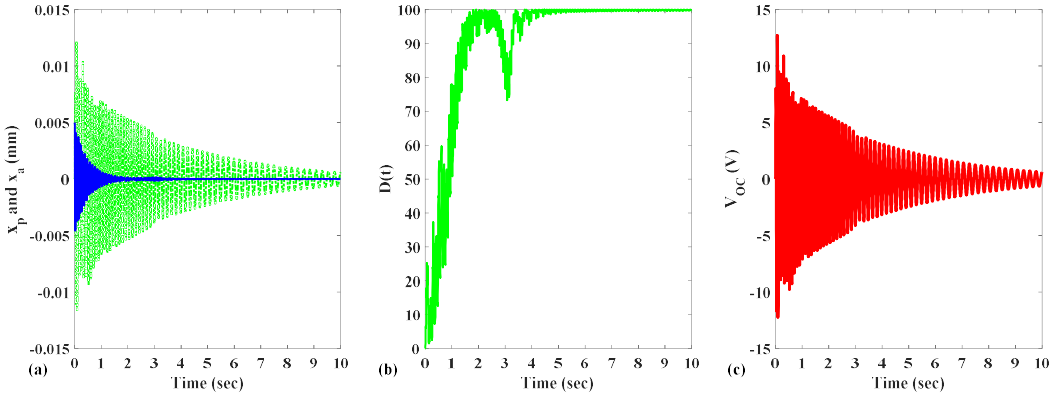

Figure 3.3 Simulation results with X = 5 mm: (a) displacements (solid line: primary system; dotted line: NES); (b) the percentage of the instantaneous energy in the NES and (c) open circuit voltage generated by the PEH.

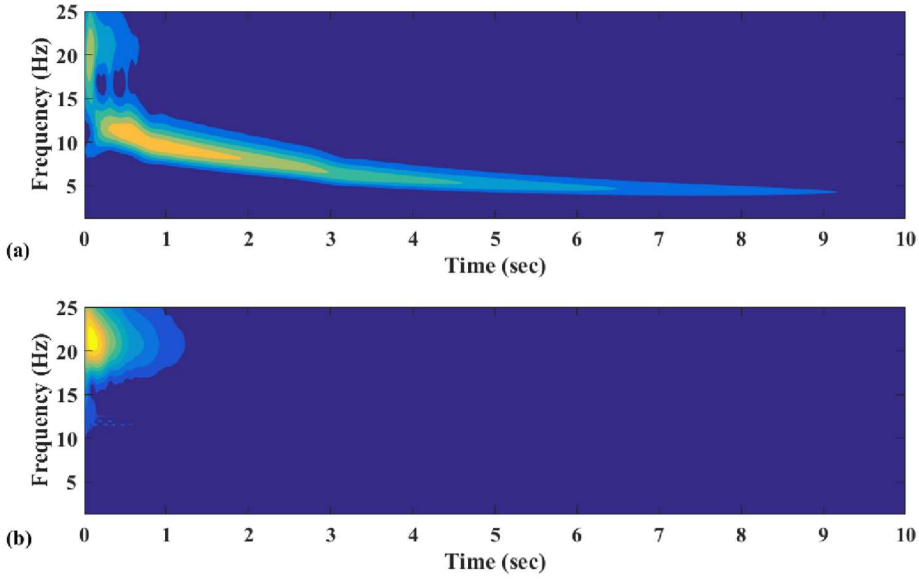

Figure 3.4 Wavelet transform spectra for simulation with X = 5 mm: (a) x_a and (b) x_p.

Figure 3.5 and Figure 3.6 show the simulation results for the case of the high-energy level or X = 10 mm. With a further increase in the initial energy level, the behavior of the 1:1 resonance is more dominant, as shown in Figure 3.5 (a) and Figure 3.6. In particular, Figure 3.6 (a) indicates that the NES is engaged in a strong nonlinear oscillation that is marked by a gradual decrease of the response frequency. However, in the first 3 seconds, both the primary mass and the NES mass

oscillate with a strong nonlinear beats phenomenon [62], indicating that energy is exchanged between the primary system and the NES. Therefore, the TET is not fully established for a short period. After 4 seconds, the TET is achieved so that the percentage of the instantaneous energy in the NES is close to 100% as shown in Figure 3.5 (b). Figure 3.5 (c) shows that the PEH's voltage magnitude further increases.

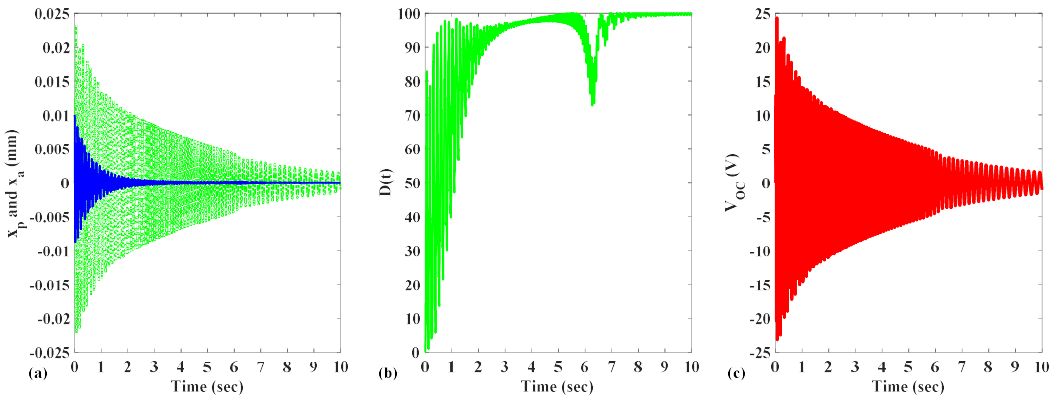

Figure 3.5 Simulation results with $X = 10$ mm: (a) displacements (solid line: primary system; dotted line: NES); (b) the percentage of the instantaneous energy in the NES and (c) open circuit voltage generated by the PEH.

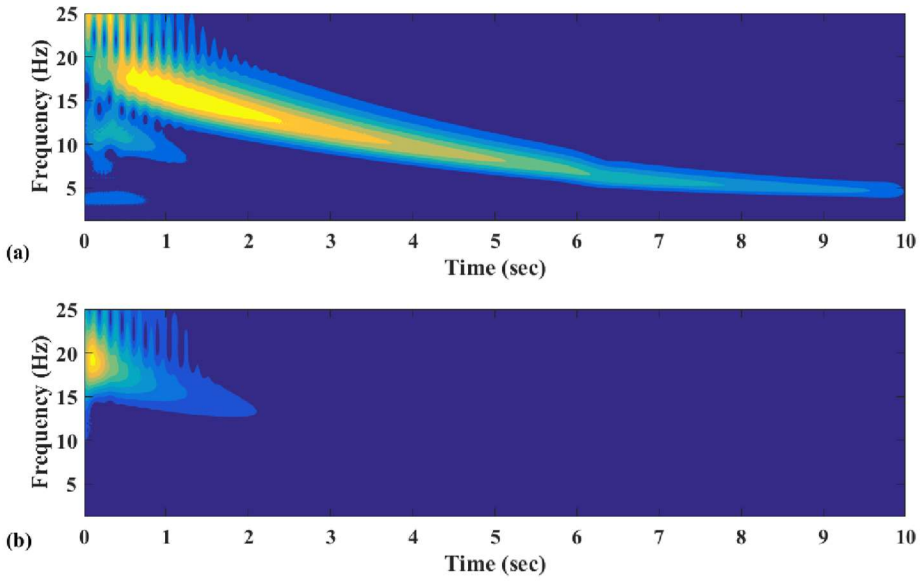

Figure 3.6 Wavelet transform spectra of the simulated response with $X = 10$ mm: (a) x_a and (b) x_p.

To investigate the effects of load resistance on the energy harvesting, the accumulated harvested energy defined by Equation (3.7) is computed for the five different resistance levels: R= 20, 50, 100, 200, 1000 kΩ. Figure 3.7 shows the results. Several observations can be made. First, the accumulated harvested energy increases with the increase of time. Second, the accumulated harvested energy increases with the increase of the initial energy level. Third, there is a best resistance in terms of maximizing the accumulated harvested energy. For five resistances considered, the highest accumulated energies are obtained with a load resistance of R = 50 kΩ for all three initial energy levels.

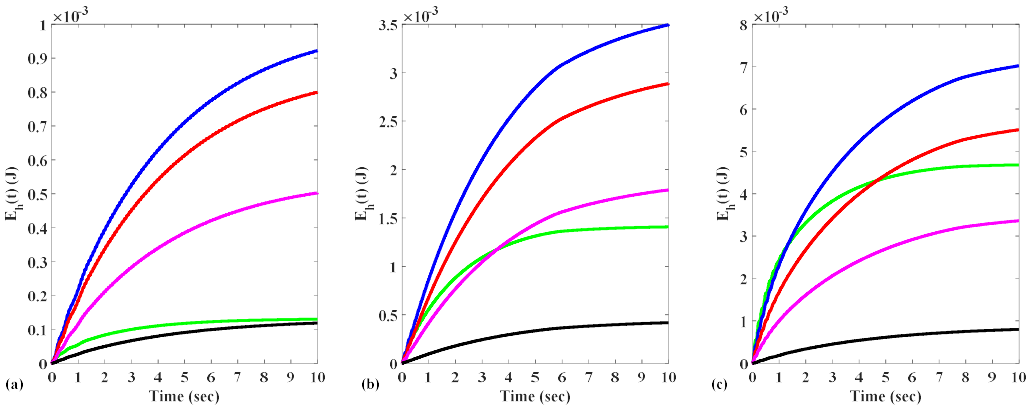

Figure 3.7 The accumulated energy harvested by the PEH: (a) low-energy level, (b) medium-energy level and (c) high-energy level; (d) resistance (green line: 20 kΩ, blue line: 50 kΩ, red line: 100 kΩ, pink line: 200 kΩ, black line: 1000 kΩ).

3.2.2 Computer simulation with the strongly coupled system

Figure 3.8 and Figure 3.9 show the simulation results for the case of the low-energy level or X = 2.5 mm. As shown in Figure 3.8 (a) and Figure 3.9, the 1:1 resonance phenomenon occurs such that the NES demonstrates the nonlinear behavior. In particular, Figure 3.8 (a) reveals that the NES oscillates with a frequency around f_2 or f_p and then the response gradually decreases to a low frequency around f_1 or f_a. However, in the first 3 seconds, a nonlinear beats phenomenon is witnessed in both of the NES and the primary system, indicating that the energy is reversible in

both the primary system and the NES. As a consequence, TET is not able to be fully established for the first few seconds. After 4 seconds, the TET is achieved so that the percentage of the instantaneous energy in the NES raises gradually to 1 as shown in Figure 3.8 (b). In Figure 3.9, a reasonably large magnitude voltage can be observed.

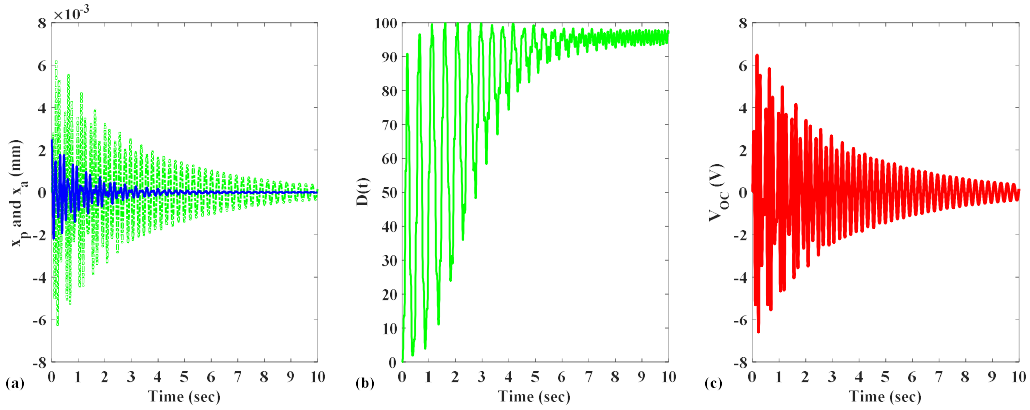

Figure 3.8 Simulation results with $X = 2.5$ mm: (a) displacements (solid line: primary system; dotted line: NES), (b) the percentage of the instantaneous energy in the NES and (c) open circuit voltage generated by the PEH.

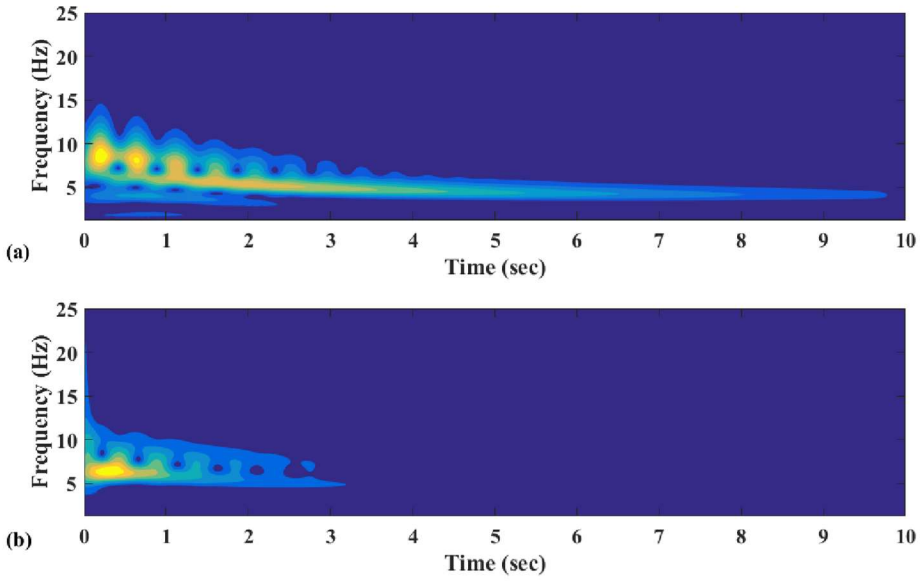

Figure 3.9 Wavelet transform spectra of simulated response with $X = 2.5$ mm: (a) x_a and (b) x_p.

Figure 3.10 and Figure 3.11 show the simulation results for the case of the medium-energy level or $X = 5$ mm. Figure 3.10 (a) and Figure 3.11 show that the 1:1 resonance is more dominant with an increase in the initial energy. As shown in Figure 3.11 (a), the NES's oscillation appears strongly nonlinear with an initial frequency around f_2 or f_p to a final frequency around f_1 or f_a. However, due to the nonlinear beats phenomenon, the strong internal nonlinear resonance leads the frequency content to jump from around f_2 or f_p to around 10 Hz. Figure 3.10 (b) indicates that the TET is fully established after 5 seconds and the energy is almost 100% localized in the NES after 7 seconds. Figure 3.10 (c) shows the increase of voltage magnitude.

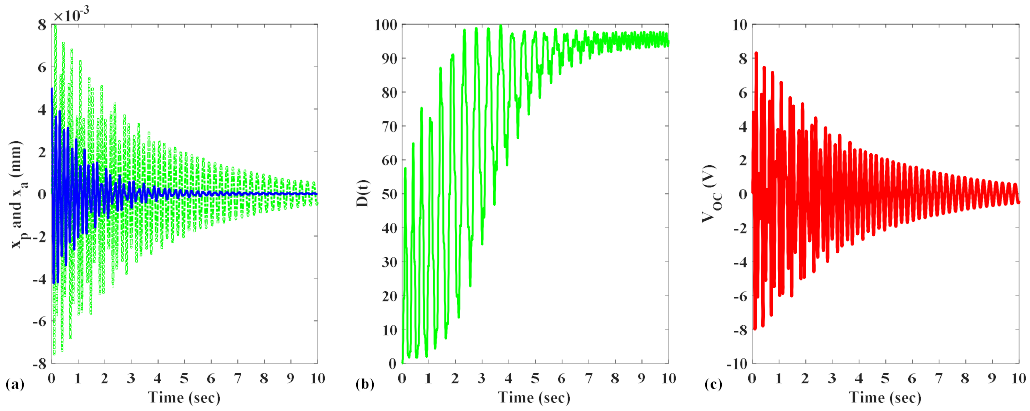

Figure 3.10 Simulation results with $X = 5$ mm: (a) displacements (solid line: primary system; dotted line: NES), (b) the percentage of the instantaneous energy in the NES, and (c) open circuit voltage generated by the PEH.

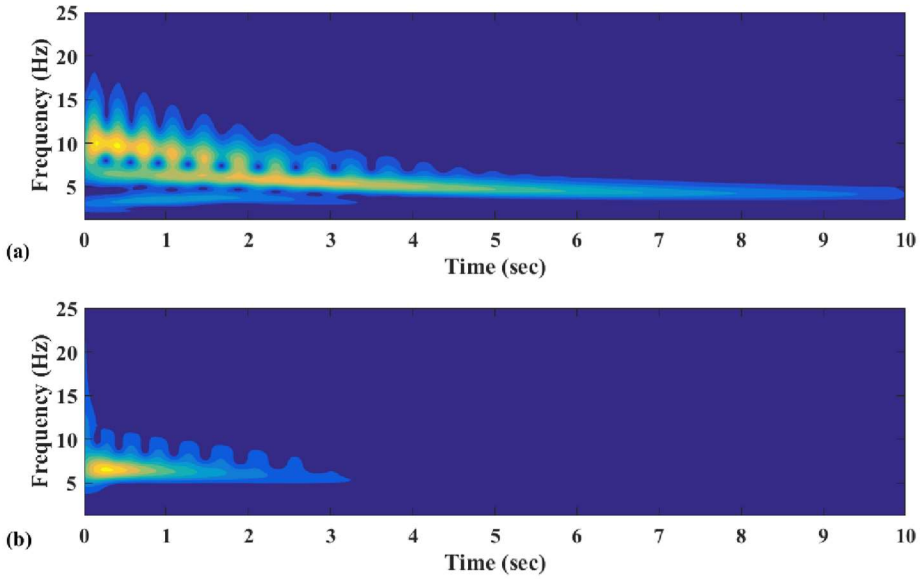

Figure 3.11 Wavelet transform spectra of simulated response with $X = 5$ mm: (a) x_a and (b) x_p.

Figure 3.12 and Figure 3.13 show the simulation results for the case of the high-energy level or $X = 10$ mm. With a further increase in the initial energy level, the desired 1:1 resonance is dominant as with medium-energy level, as shown in Figure 3.12 (a) and Figure 3.13, the NES oscillates with a strong nonlinearity, indicated by a gradual decrease of the response frequency. Still, as shown in Figure 3.13 (a) and Figure 3.12 (b), a long period of the nonlinear beats causes the delay in establishing the TET. After 7 seconds, the energy is almost localized in the NES. Besides, Figure 3.12 (c) indicates that the PEH's voltage magnitude increases insignificantly compared to the case shown in Figure 3.10 (c).

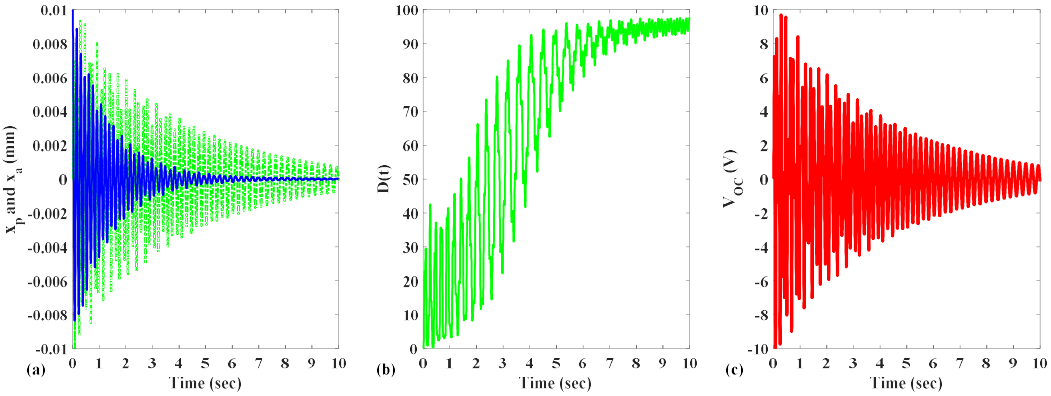

Figure 3.12 Simulation results with $X = 10$ mm: (a) displacements (solid line: primary system; dotted line: NES); (b) the percentage of the instantaneous energy in the NES and (c) open circuit voltage generated by the PEH.

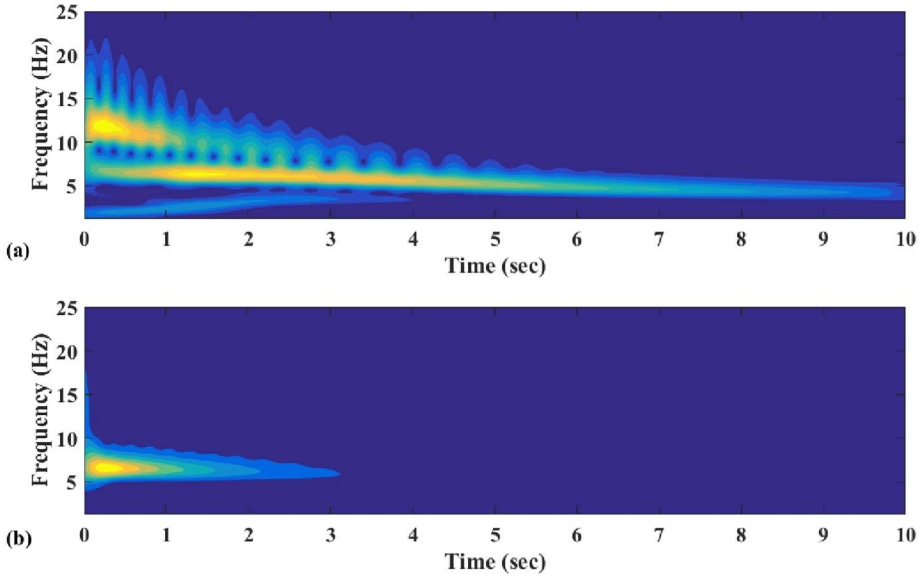

Figure 3.13 Wavelet transform spectra of simulated response with $X = 10$ mm: (a) x_a and (b) x_p.

Figure 3.14 presents the simulation results of the accumulated harvested energy for the strongly coupled system. Similar observations to those from the weakly coupled system are found. Firstly, the accumulated harvested energy increases over time. Next, the accumulated harvested energy increases from the low-energy level to the high-energy level. Thirdly, the highest

accumulated energies are obtained with the load resistance of R = 50 kΩ for all the three initial energy levels.

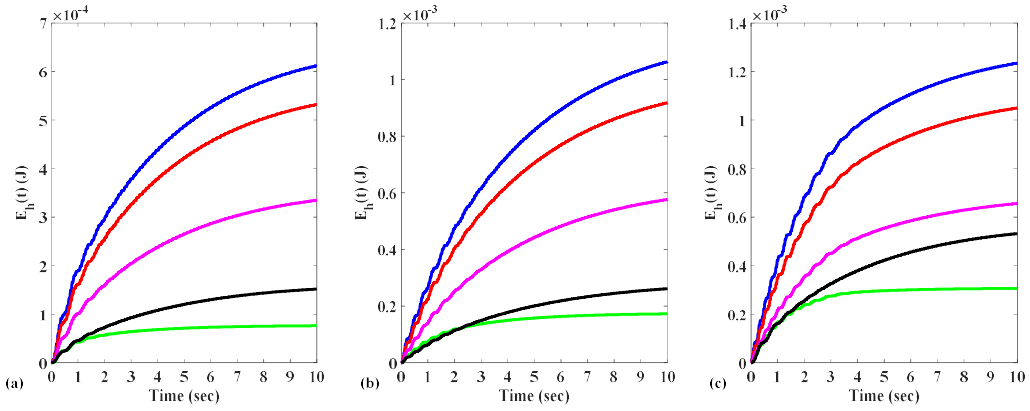

Figure 3.14 The accumulated energy harvested by the PEH: (a) low-energy level, (b) medium-energy level and (c) high-energy level; (d) resistance (green line: 20 kΩ, blue line: 50 kΩ, red line: 100 kΩ, pink line: 200 kΩ, black line: 1000 kΩ).

3.3 Simulation results with the piecewise linear function

It is of interest to investigate the behaviors of the combined systems if the NES's stiffness is defined by the piecewise linear functions obtained in Chapter 2. The equations of motion of the combined system are defined by:

$$m_a\ddot{x}_a + c_a(\dot{x}_a - \dot{x}_p) + f(x_a - x_p) + \theta V = 0 \tag{3.9}$$

$$m_a\ddot{x}_p + c_p(\dot{x}_a - \dot{y}) + k_p(x_p - y) - \left[c_a(\dot{x}_a - \dot{x}_p) + f(x_a - x_p) + \theta V\right] = 0 \tag{3.10}$$

where $f(x_a - x_p)$ is the piecewise linear function defined by:

$$f(x_a - x_p) = \begin{cases} k_{11}(x_a - x_p) \text{ if } (x_a - x_p) < -\dfrac{b_1}{2} \\ k_{12}(x_a - x_p) \text{ if } -\dfrac{b_1}{2} \le (x_a - x_p) \le -\dfrac{b_2}{2} \\ k_{13}(x_a - x_p) \text{ if } -\dfrac{b_2}{2} \le (x_a - x_p) \le \dfrac{b_2}{2} \\ k_{14}(x_a - x_p) \text{ if } \dfrac{b_2}{2} \le (x_a - x_p) \le \dfrac{b_1}{2} \\ k_{11}(x_a - x_p) \text{ if } \dfrac{b_1}{2} < (x_a - x_p) \end{cases} \tag{3.11}$$

where k_{11}, k_{12}, k_{13}, k_{14} and k_{15} are the piece-wise linear stiffnesses; and b_1 and b_2 are the "clearances".

The values of the piece-wise linear stiffness can be found in Table 2.4. They are $k_{11} = 261.9$ N/m, $k_{12} = 92.85$ N/m, $k_{13} = 24.88$ N/m, $k_{14} = 90.25$ N/m and $k_{15} = 173.7$ N/m respectively. And the clearances can be found in Figure 2.14 (b) which are $b_1 = 10.47$ mm and $b_2 = 6.832$ mm.

Only the weakly coupled system is considered. Figure 3.15 and Figure 3.16 show the simulation results with the low-energy level. Figure 3.15 (a) and Figure 3.16 indicate that the primary system and the NES oscillate in two different frequencies, or the 1:1 resonance phenomenon is not achieved. Figure 3.16 (a) shows that the NES behaves almost linearly. However, similar to the case with the cubic function shown in Figure 3.1 (c), Figure 3.15 (c) shows that the TET can still be established without the 1:1 resonance.

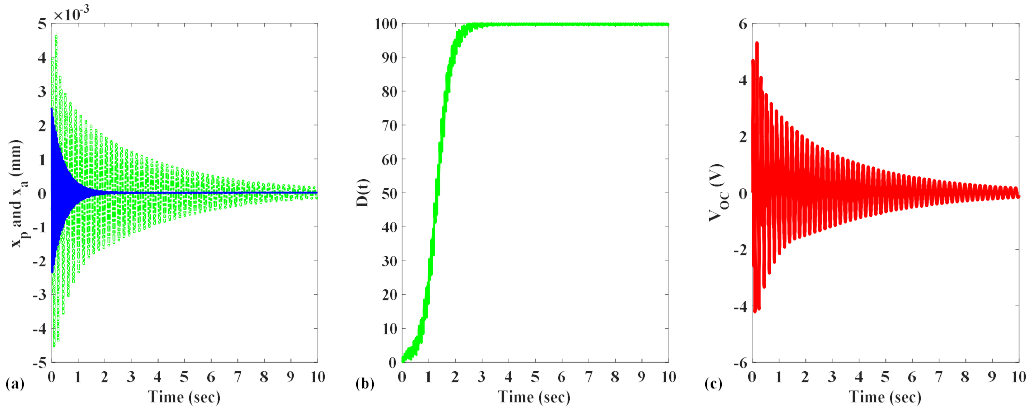

Figure 3.15 Simulation results with $X = 2.5$ mm: (a) displacements (solid line: primary system; dotted line: NES); (b) the percentage of the instantaneous energy in the NES and (c) open circuit voltage generated by the PEH.

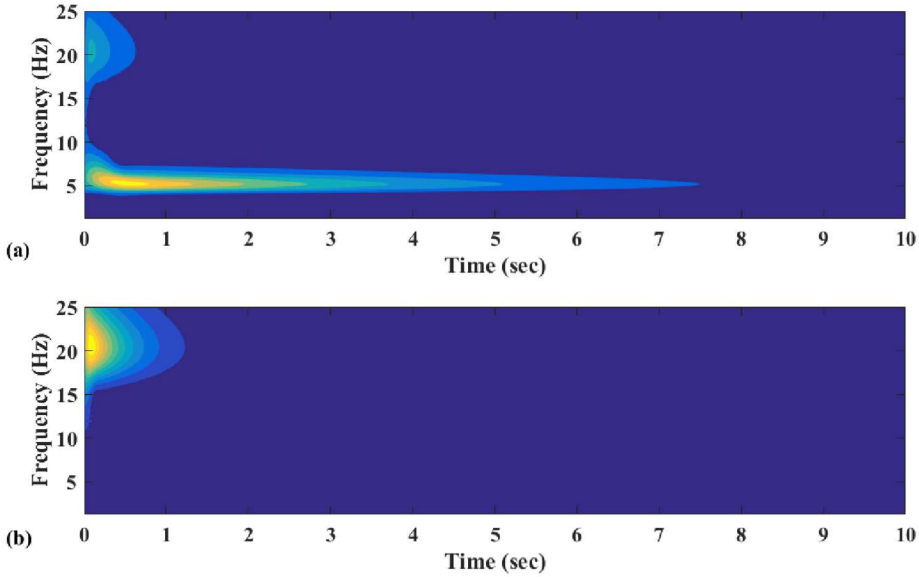

Figure 3.16 Wavelet transform spectra of simulated response with $X = 2.5$ mm: (a) x_a and (b) x_p.

Figure 3.17 and Figure 3.18 show the simulation results for the case of the medium-energy level or $X = 5$ mm. As shown in Figure 3.17 (a) and Figure 3.18, the NES's response becomes more nonlinear. In Figure 3.18 (a), in the beginning, the frequency content of the NES is around 20 Hz which is close to f_p or f_2, indicating that the 1:1 resonance is established. As a result, the NES's response shows more nonlinearity. However, due to the nature of the piecewise linear stiffness, the frequency of the response quickly drops to around 10 Hz and then gradually sets down at a low frequency around f_1 or f_a. As shown in Figure 3.17 (b), the TET is fully established after 2 seconds. Figure 3.17 (c) shows the PEH voltage that is similar to that observed in Figure 3.3 (c).

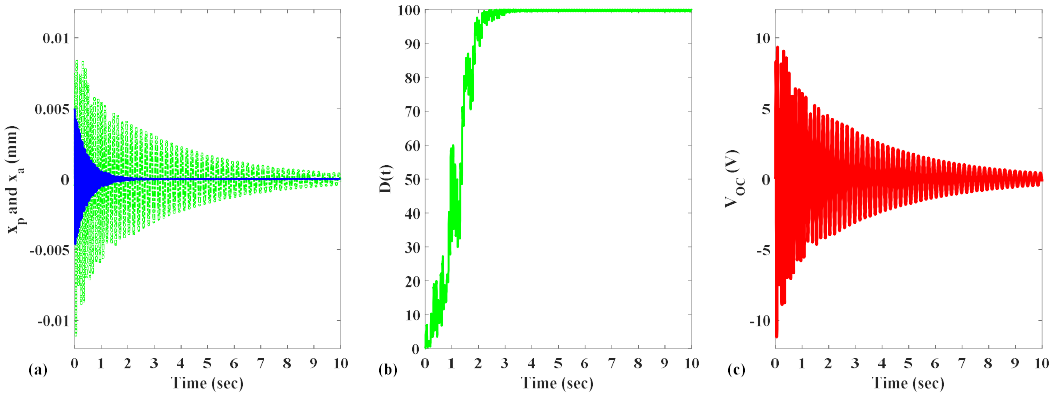

Figure 3.17 Simulation results with X = 5 mm: (a) displacements (solid line: primary system; dotted line: NES); (b) the percentage of the instantaneous total energy in the NES and (c) open circuit voltage generated by the PEH.

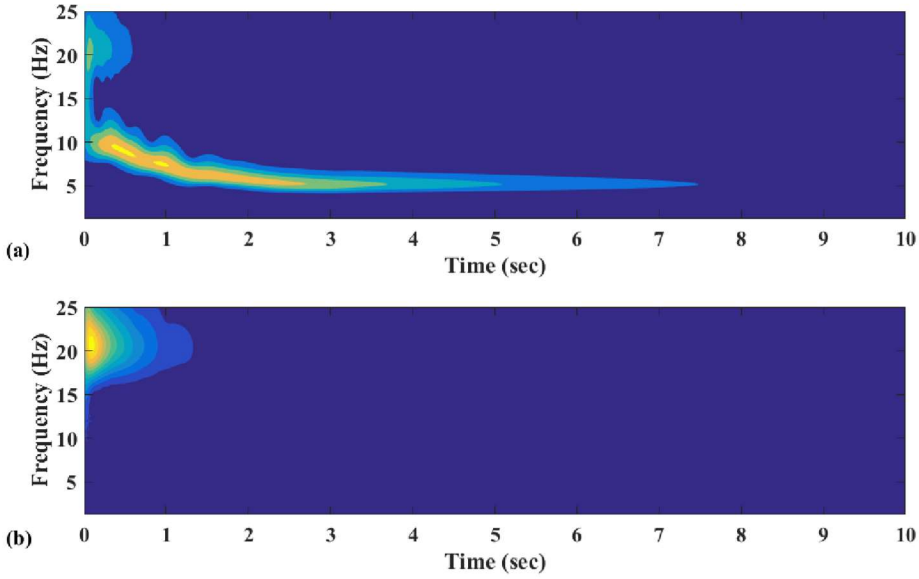

Figure 3.18 Wavelet transform spectra of simulated response with X = 5 mm: (a) x_a and (b) x_p.

Figure 3.19 and Figure 3.20 show the simulation results for the case of the high-energy level or X = 10 mm. With the increase of the initial displacement, the response of the NES demonstrates a strong nonlinear behavior as shown in Figure 3.20 (a) and the 1:1 resonance is achieved shown as Figure 3.19 (a). The PEH's voltage magnitude increases significantly shown in

Figure 3.19 (c). Besides, as shown in Figure 3.19 (b), the desired TET is established so that the energy is localized in the NES eventually.

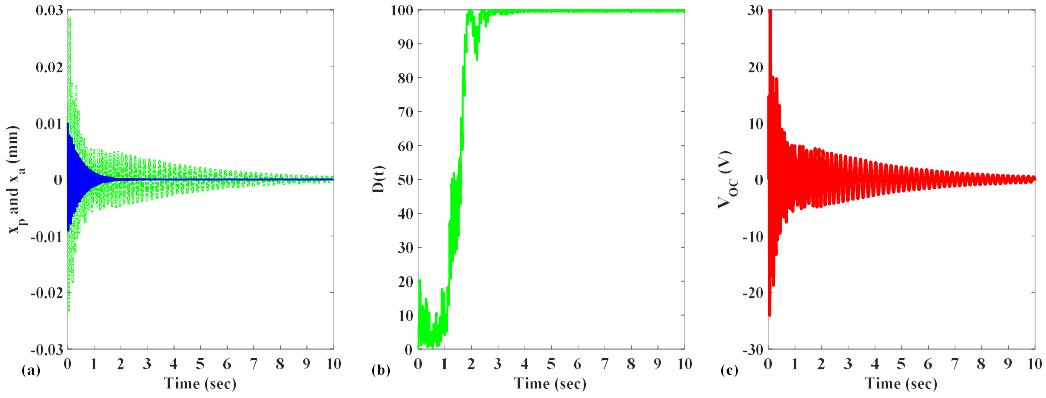

Figure 3.19 Simulation results with $X = 10$ mm: (a) displacements (solid line: primary system; dotted line: NES); (b) the percentage of the instantaneous total energy in the NES and (c) open circuit voltage generated by the PEH.

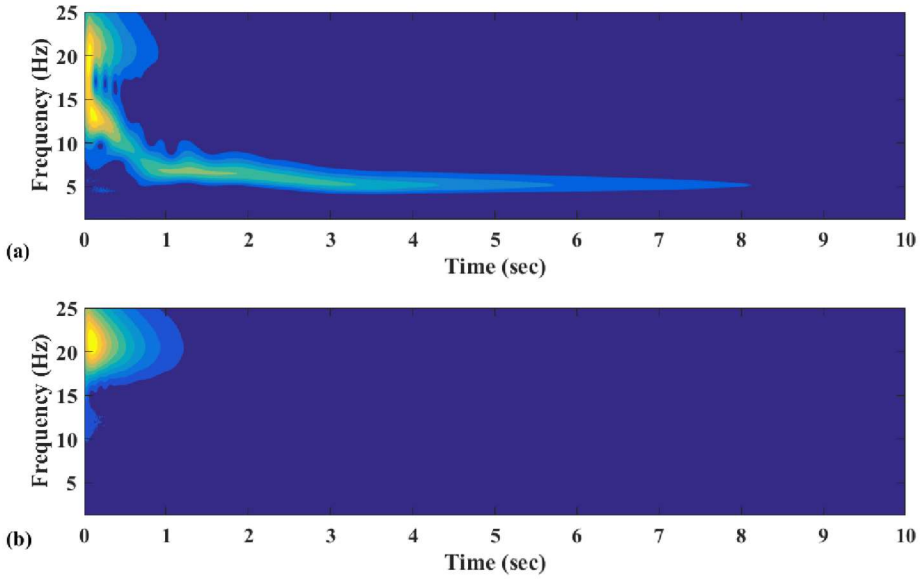

Figure 3.20 Wavelet transform spectra of simulated response with $X = 10$ mm: (a) x_a and (b) x_p.

Figure 3.14 shows the effects of load resistance on the accumulated harvested energy. The general trends are similar to those shown in Figure 3.7. However, the magnitudes of the

accumulated energy are lower than those in Figure 3.7. The conclusions made of the results in Figure 3.21 are the same as those previously made.

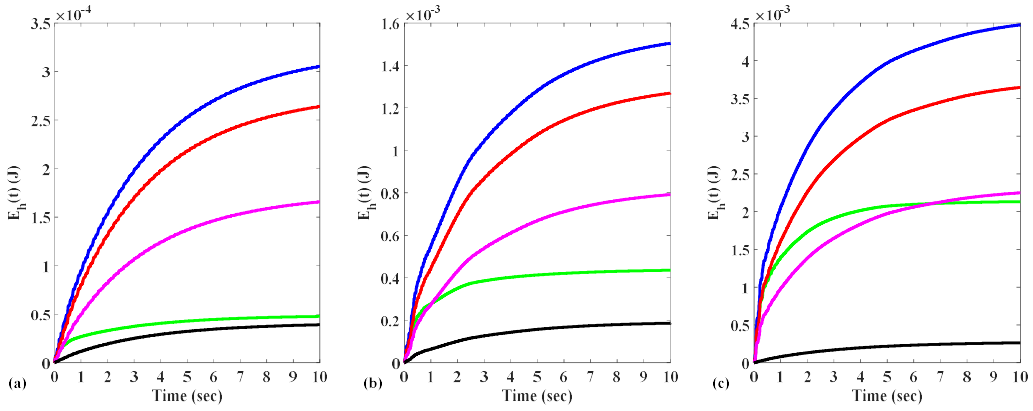

Figure 3.21 The accumulated energy harvested by the PEH: (a) low-energy level, (b) medium-energy level and (c) high-energy level; (d) resistance (green line: 20 kΩ, blue line: 50 kΩ, red line: 100 kΩ, pink line: 200 kΩ, black line: 1000 kΩ).

3.4 Experimental results

In order to validate the simulation results, the experiments are conducted. The experimental set-ups are shown in Figure 3.22 and Figure 3.30, respectively. The base of the combined system is firmly fixed on the ground. Two reflex (RF) lasers sensors on the left are used to measure the responses of the primary mass and the NES mass, respectively. As shown in Figure 3.22 and Figure 3.30, a steel bracket mounted on a support (not shown) is used to control the initial displacements. For the low-energy level, the initial displacement should be controlled to be around $X = 2.5$ mm. For the medium-energy level considered, the initial displacement should be controlled to be around $X = 5$ mm. For the high-energy level considered, the initial displacement should be controlled to be around $X = 10$ mm.

3.4.1 Experimental results with the weakly coupled system

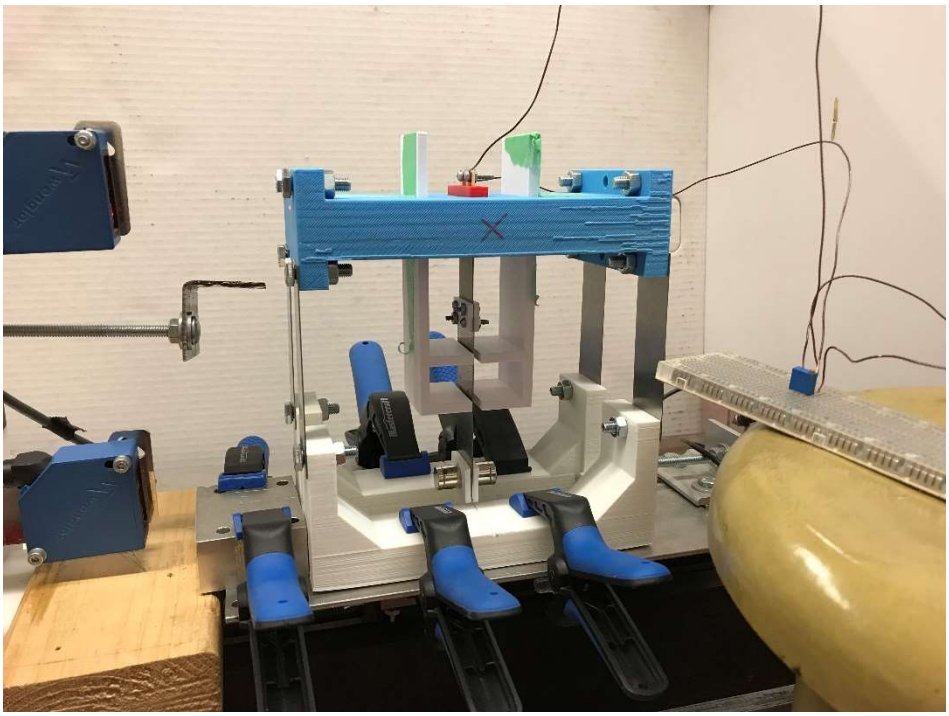

Figure 3.22 Photo of the weakly coupled system.

Figure 3.23 and Figure 3.24 demonstrate experimental results with the initial displacement $X = 2.48$ mm. As shown in Figure 3.23 (a) and Figure 3.24, the NES is not engaged in the 1:1 resonance. In Figure 3.24 (a), the WT spectrum of the NES's response shows that the frequency of the response decreases from a frequency around 7.5 Hz to the frequency around f_1 or f_a in less than 0.5 seconds. This indicates that the NES's nonlinearity is partially induced. However, the TET is fully established as shown in Figure 3.23 (b). Figure 3.23 (c) shows that the PEH is able to obtain a reasonably voltage magnitude. Note that as it is not possible for the measured response to be completely zero, a condition is imposed to make $x_p(t)$ zero if $\left|x_p(t)\right| \le 5\times10^{-5}$ m. With this condition, 100% of the TET is established or $D(t) = 1$ if $\left|x_p(t)\right| \le 5\times10^{-5}$.

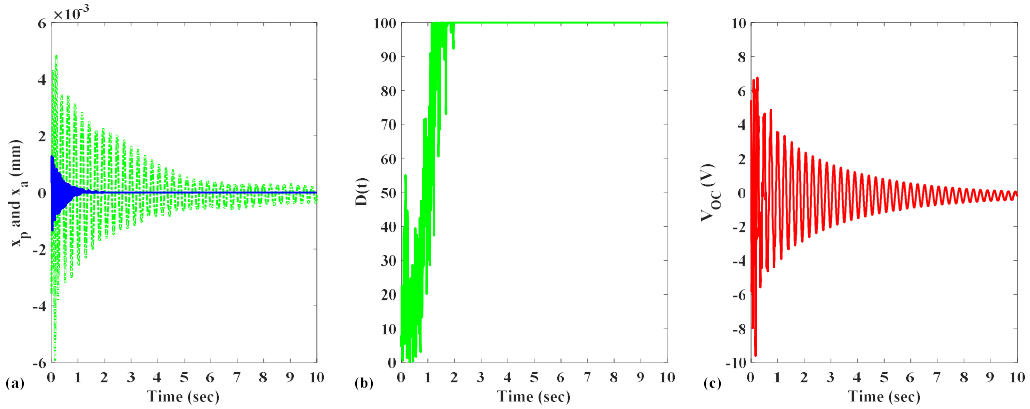

Figure 3.23 Experimental results with X=2.48 mm: (a) displacements (solid line: primary system; dotted line: NES); (b) the percentage of the instantaneous total energy in the NES and (c) open circuit voltage generated by the PEH.

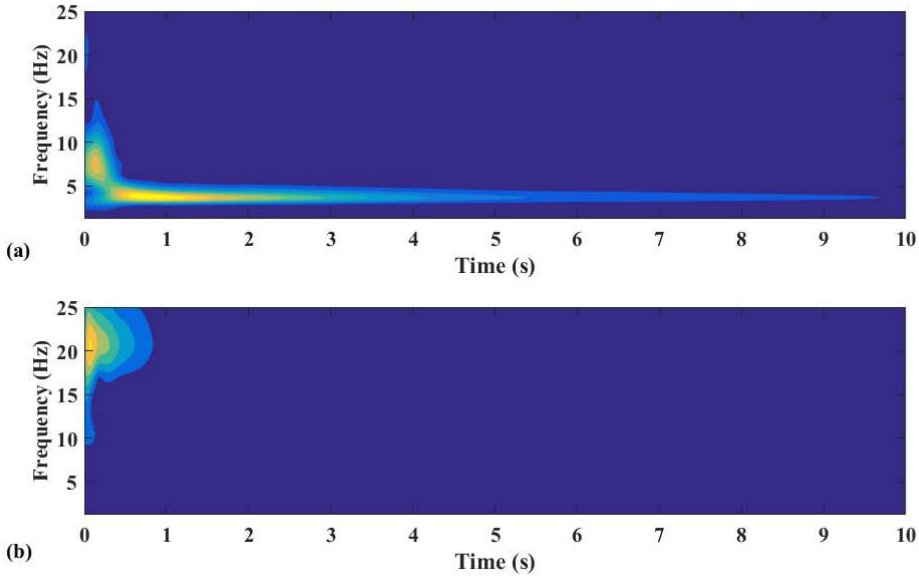

Figure 3.24 Wavelet transform spectra with X = 2.48 mm: (a) x_a and (b) x_p.

Figure 3.25 and Figure 3.26 show the experimental results with the initial displacement $X = 5.03$ mm or the medium-energy level. As shown in Figure 3.25 (a), the primary system and NES do not vibrate at the same frequency, indicating that the 1:1 resonance is not established. Figure 3.26 (a) shows that in the beginning, the NES is set into vibration with a frequency around 7.5 Hz and then the response of the NES quickly decreases to the frequency around f_1 or f_a,

indicating that the NES's nonlinearity is partially induced. As shown in Figure 3.25 (b), the TET is quickly achieved in a short period even without the 1:1 resonance. The percentage of the instantaneous energy in the NES is close to 100% after a short period as well. The voltage magnitude generated by the PEH sees a slight increase as demonstrated in Figure 3.25 (c).

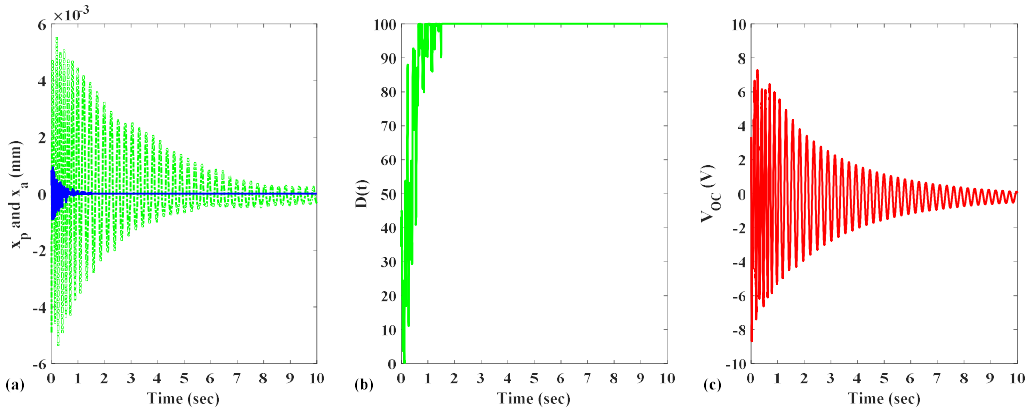

Figure 3.25 Experimental results with X =5.03 mm: (a) displacements (solid line: primary system; dotted line: NES); (b) the percentage of the instantaneous total energy in the NES and (c) open circuit voltage generated by PEH.

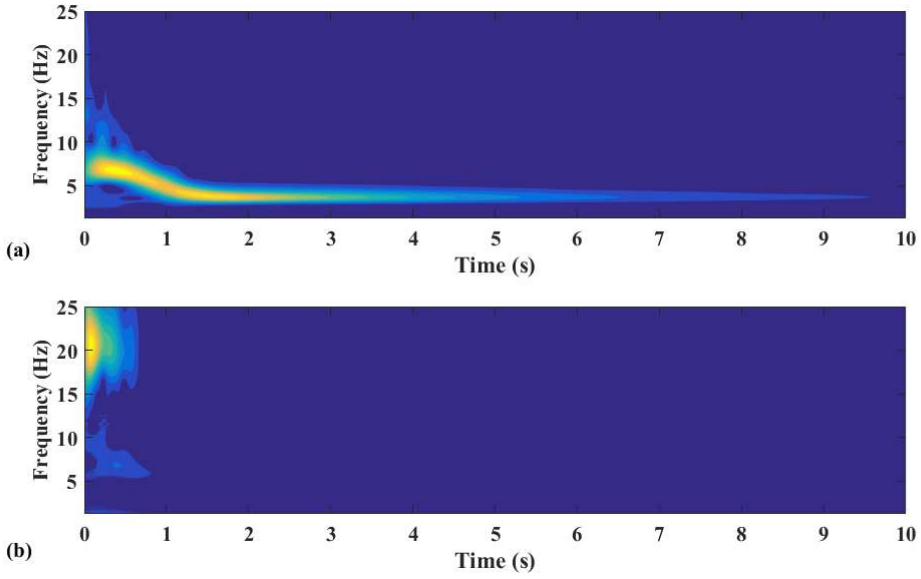

Figure 3.26 Wavelet transform spectra with X = 5.03 mm: (a) x_a and (b) x_p.

Figure 3.27 and Figure 3.28 show the experimental results with the initial displacement $X = 10.29$ mm or the high-energy level. Figure 3.27 (a) shows that the primary system and the NES oscillate with different frequencies. Figure 3.28 shows that both of the NES's and primary system's response start with a high frequency around f_2 or f_p. Then the NES's response frequency decreases to a frequency around 7.5 Hz for about 0.5 seconds and further decreases to a frequency around f_1 or f_a. This indicates that the desired 1:1 resonance is achieved and the NES's response shows a strong nonlinearity. Compared with simulation results, the nonlinear beats are less dominant. Therefore, after 1 second, the TET is fully established, and almost 100% of the energy is localized in the NES, as shown in Figure 3.27 (b). The PEH's voltage magnitude sees a further increase. Compared with the simulation results, the PEH's voltage magnitude is limited in 10 V. This is mainly due to the physical limitations of the PEH. Also, the analog to digital conversion channels of the data acquisition system are limited by ± 10 V. Overall the experimental results agree well with simulation results.

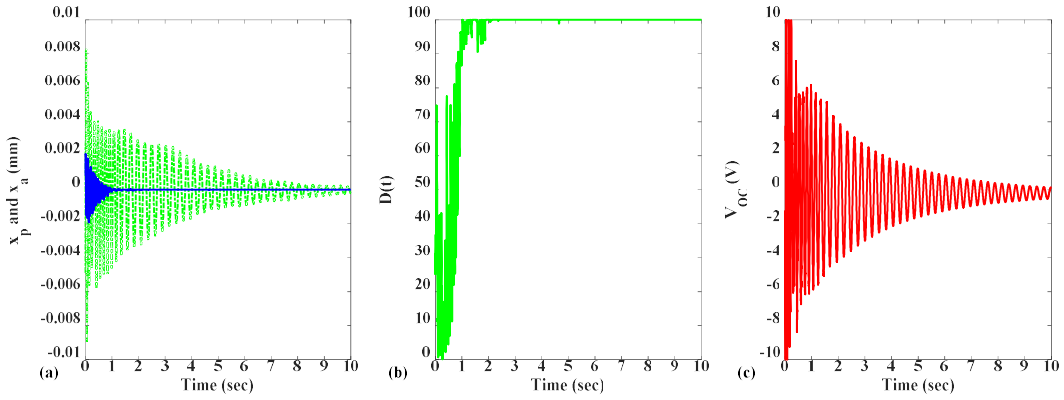

Figure 3.27 Experimental results with X=10.29 mm: (a) displacements (solid line: primary system; dotted line: NES); (b) the percentage of the instantaneous total energy in the NES and (c) open circuit voltage generated by the PEH.

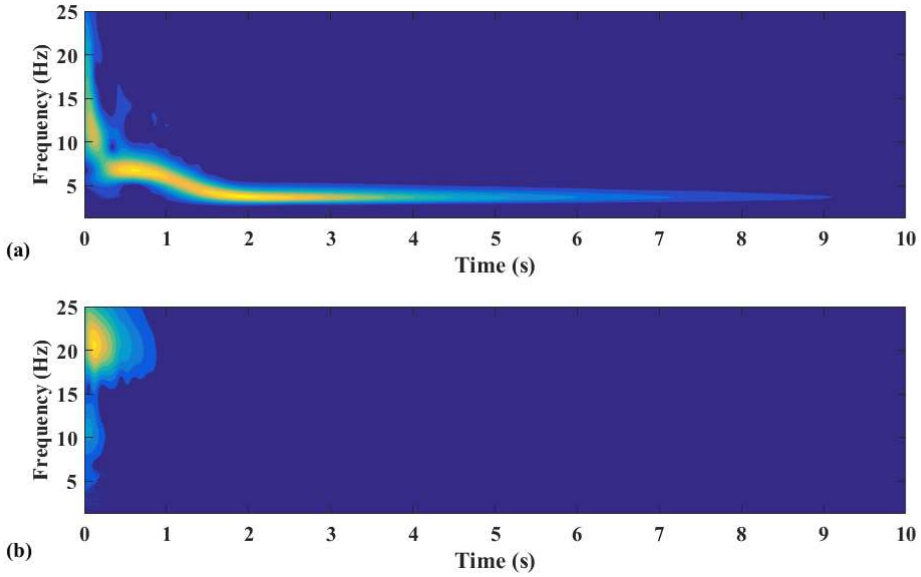

Figure 3.28 Wavelet transform spectra with $X = 10.29$ mm: (a) x_a and (b) x_p.

Figure 3.29 shows the effects of load resistances on the PEH's harvested energy. Compared with the results shown in Figure 3.7, the main difference is that the highest accumulated harvested energies are obtained with the load resistance of $R = 200$ kΩ instead of 50 kΩ

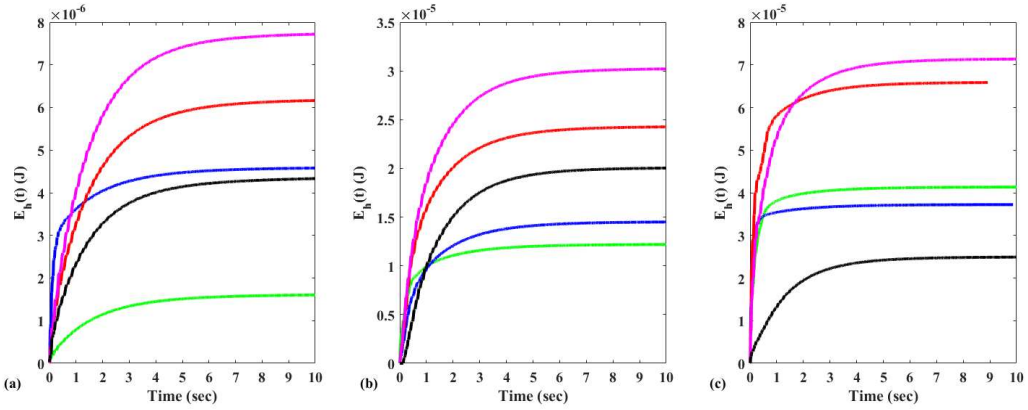

Figure 3.29 The accumulated energy harvested by the PEH: (a) low-energy level, (b) medium-energy level and (c) high-energy level; (d) resistance (green line: 20 kΩ, blue line: 50 kΩ, red line: 100 kΩ, pink line: 200 kΩ, black line: 1000 kΩ).

3.4.2 Experimental results with the strongly coupled system

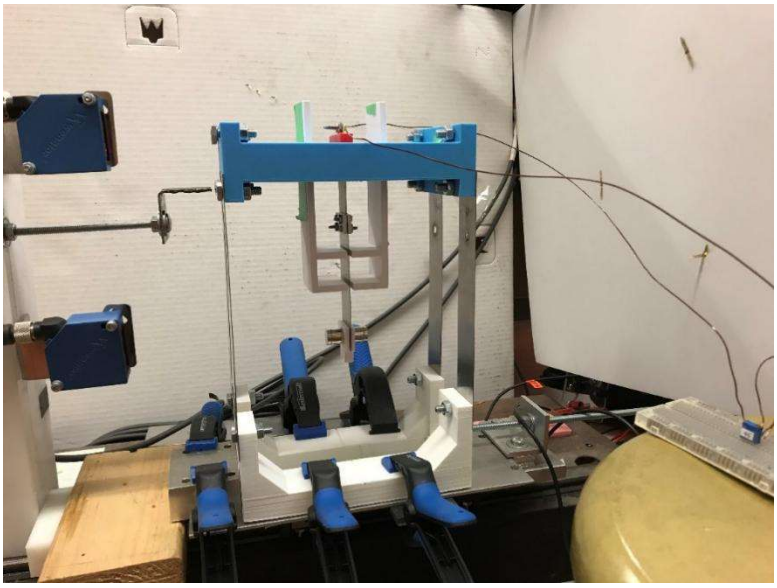

Figure 3.30 Photo of the strongly coupled system.

Figure 3.31 and Figure 3.32 show the experimental results with the initial displacement X = 2.55 mm or the low-energy level. As shown in Figure 3.31 (a) and Figure 3.32, the 1:1 resonance is established and a weak nonlinear manner is observed. In Figure 3.31 (b), after 2 seconds, the energy is localized in the NES system so that the desired TET occurs. As shown in Figure 3.31 (c), a fairly large magnitude voltage is generated by the PEH.

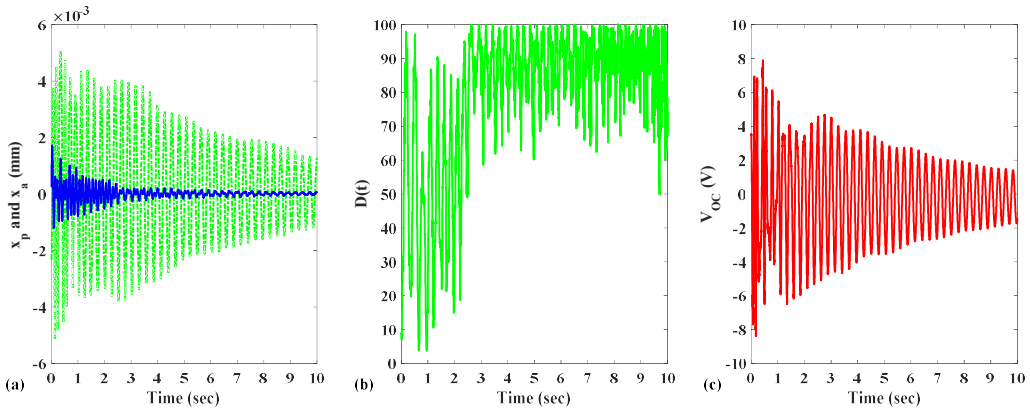

Figure 3.31 Experimental results with X =2.55 mm: (a) displacements (solid line: primary system; dotted line: NES); (b) the percentage of the instantaneous total energy in the NES and (c) open circuit voltage generated by the PEH.

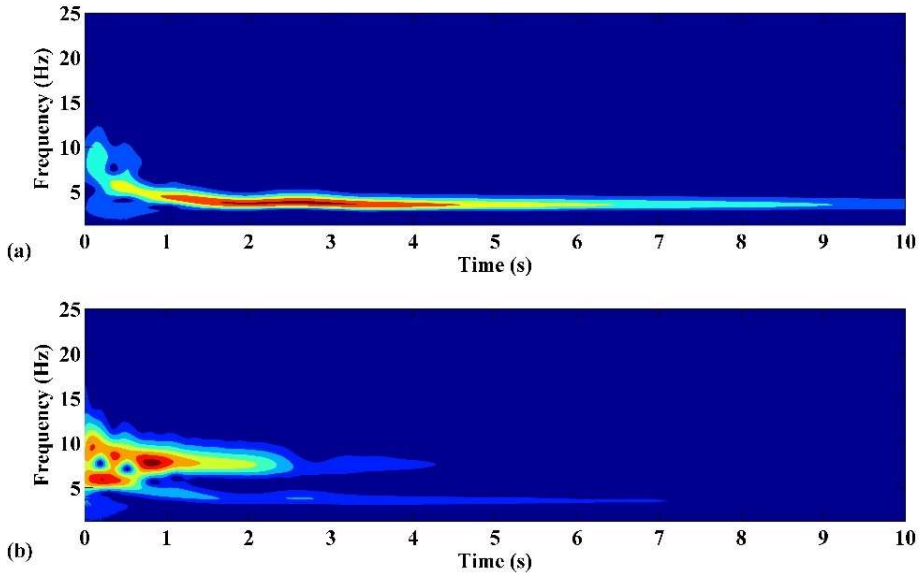

Figure 3.32 Wavelet transform spectra with X = 2.55 mm: (a) x_a and (b) x_p.

Figure 3.33 and Figure 3.34 show the experimental results with the initial displacement X = 5.19 mm or the medium-energy level. A stronger nonlinearity and more dominant 1:1 resonance are observed in Figure 3.33 (a) and Figure 3.34. However, the energy is not able to be

fully localized in the NES such that the TET is partially achieved, as shown in Figure 3.33 (b). The PEH's voltage magnitude changes little between Figure 3.33 (c) and Figure 3.31 (c).

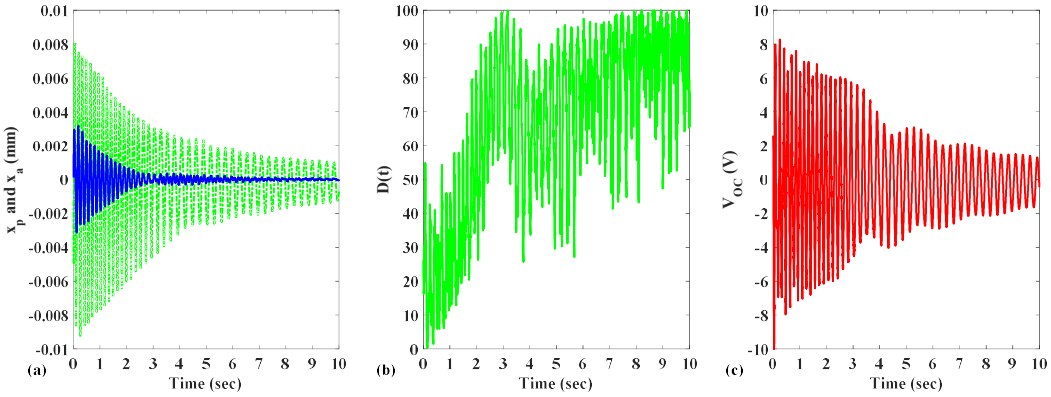

Figure 3.33 Experimental results with X=5.19 mm: (a) displacements (solid line: primary system; dotted line: NES); (b) the percentage of the instantaneous total energy in the NES and (c) open circuit voltage generated by PEH.

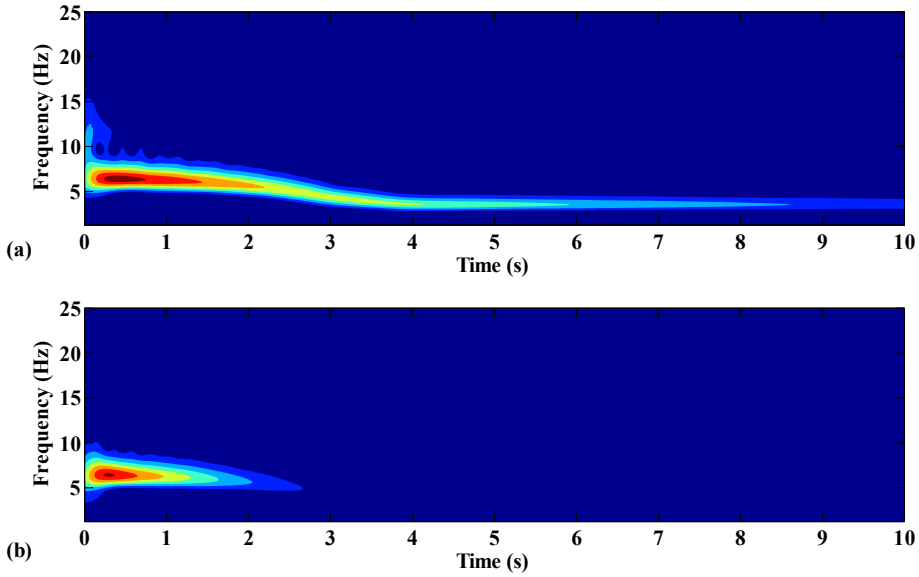

Figure 3.34 Wavelet transform spectra with X = 5.19 mm: (a) x_a and (b) x_p.

Figure 3.35, Figure 3.36 and Figure 3.37 show the experimental results with the initial displacement $X = 10.14$ mm or the high-energy level. The system behaves in similar way to that with the medium-energy level.

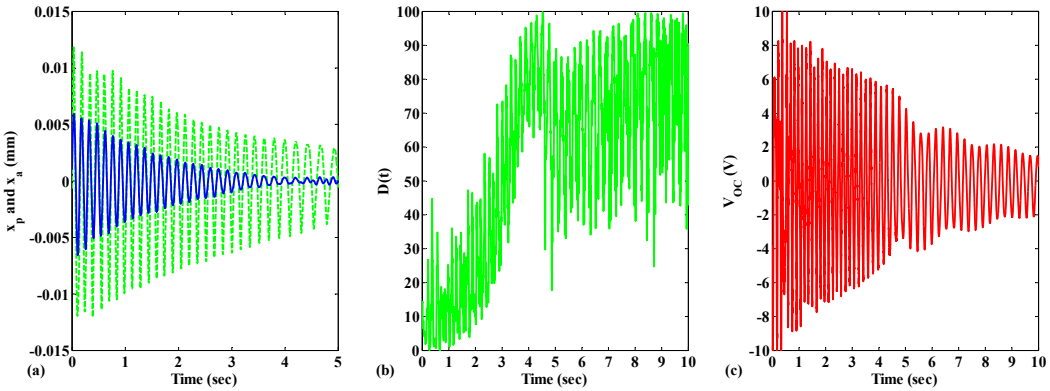

Figure 3.35 Experimental results with X=10.14 mm: (a) displacements (solid line: primary system; dotted line: NES); (b) the percentage of the instantaneous total energy in the NES and (c) open circuit voltage generated by PEH.

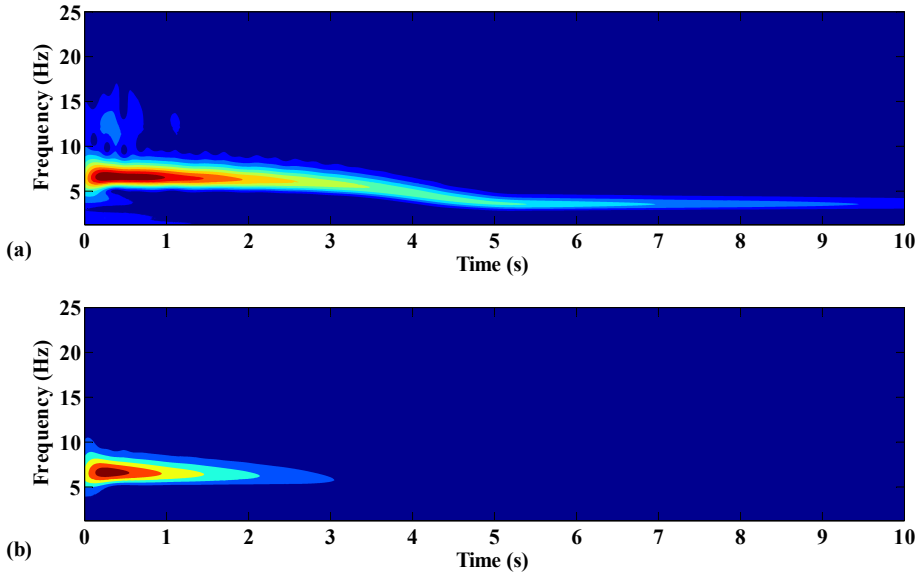

Figure 3.36 Wavelet transform spectra with X = 10.14 mm: (a) x_a and (b) x_p.

Figure 3.37 shows the effects of load resistances on the PEH's harvested energy. Compared with the results shown in Figure 3.21, the main difference is that the highest accumulated harvested energies are obtained with the load resistance of R = 200 kΩ instead of 50 kΩ. Compared with the

results shown in Figure 3.29, the magnitude of the accumulated harvested energy is lower than those for the weakly coupled system.

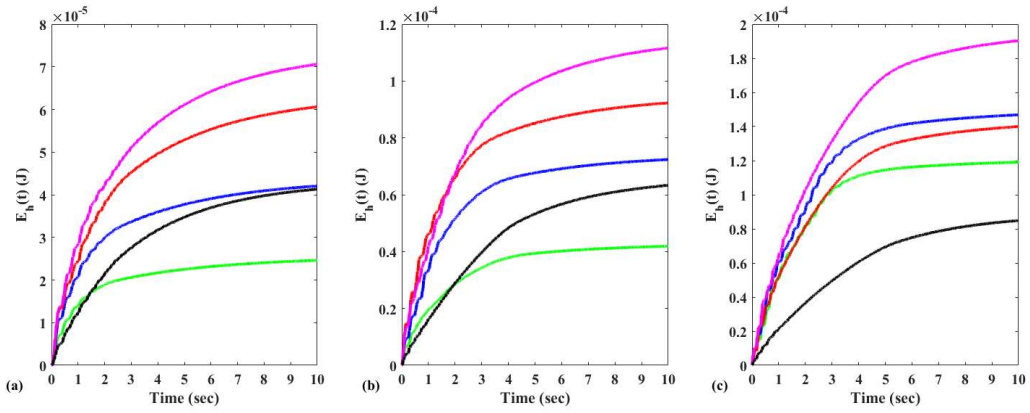

Figure 3.37 The accumulated energy harvested by PEH: (a) low-energy level, (b) medial-energy level and (c) high-energy level; (d) resistance (green line: 20 kΩ, blue line: 50 kΩ, red line: 100 kΩ, pink line: 200 kΩ, black line: 1000 kΩ).

In general, the simulation results are validated by the experimental results. It is noted that the weakly coupled system demonstrates a better TET performance than the strongly coupled system. And the variant NES in the weakly coupled system is witnessed a stronger behavior of the nonlinearity than the strongly coupled system.

3.5 Nonlinear normal mode analysis

Normal modes are an important concept in linear vibration theory. The equation of motion of a multi-degree-of-freedom (MDOF) linear system can be decoupled using the normal modes. Each of the decoupled equations of motions can be treated as an SDOF system and its modal response can be obtained by solving the SDOF system. Then the total responses of the system can be found by superposition of the modal responses. The concept of the normal mode can be extended to nonlinear system. A nonlinear normal mode (NNM) of an undamped discrete MDOF system is defined as a synchronous period oscillation where all the coordinates or masses of the

system reach their extreme positions or pass through zero simultaneously [43]. In [19], the NNM is further defined as a (not necessarily synchronous) time-periodic oscillation of a non-dissipative dynamic system. In what follows, the NNM analysis is conducted to understand the frequency contents of the combined system and the energy threshold required by the establishment of the 1:1 resonance. The equations of motion of the underlying Hamiltonian (free of damping) mechanical system are defined as follow:

$$m_a\ddot{x}_a + k_1(x_a - x_p) + k_3(x_a - x_p)^3 = 0 \tag{3.12}$$

$$m_p\ddot{x}_p + k_p x_p - \left[k_1(x_a - x_p) + k_3(x_a - x_p)^3\right] = 0 \tag{3.13}$$

In the NNM analysis, the complexification-averaging method (CX-A) is used [19]. To this end, the following complex variables are introduced:

$$\psi_1 = \dot{x}_p + j\omega x_p \text{ and } \psi_2 = \dot{x}_a + j\omega x_a \tag{3.14}$$

where ω is the dominant frequency also known as the fast frequency and $j = \sqrt{-1}$. In terms of the new variables, the displacements and the accelerations of the undamped combined system can be expressed as follow:

$$x_p = \frac{\psi_1 - \bar{\psi}_1}{2j\omega}, \ddot{x}_p = \dot{\psi}_1 - \frac{j\omega}{2}(\psi_1 + \bar{\psi}_1) \tag{3.15}$$

$$x_a = \frac{\psi_2 - \bar{\psi}_2}{2j\omega}, \ddot{x}_a = \dot{\psi}_2 - \frac{j\omega}{2}(\psi_2 + \bar{\psi}_2) \tag{3.16}$$

where the terms with the overbar denote complex conjugate.

Since the nearly monochromatic periodic solution (the periodic orbits) are sought, an assumption can be made that the primary system and the NES vibrate at the same fast frequency

ω. Therefore, the two complex variables can be approximately expressed in terms of the fast frequency ω, $e^{j\omega t}$, and they can be modulated by slowly varying amplitudes $\phi_n(t)$, $n=1, 2$:

$$\psi_1(t)=\phi_1(t)e^{j\omega t} \text{ and } \psi_2(t)=\phi_2(t)e^{j\omega t} \tag{3.17}$$

Substituting Equations (3.15) and (3.16) into Equations (3.12) and (3.13) yields the following expressions:

$$\begin{aligned} &m_p\left(\frac{d}{dt}\psi_1(t)-\frac{1}{2}j\omega(\psi_1(t)+\bar{\psi}_1(t))\right)-\frac{jk_p(\psi_1(t)-\bar{\psi}_1(t))}{2\omega} \\ &-\frac{jk_1\left((\psi_1(t)-\bar{\psi}_1(t))-(\psi_2(t)-\bar{\psi}_2(t))\right)}{2\omega}-\frac{k_3\left(j\left((\psi_1(t)-\bar{\psi}_1(t))-(\psi_2(t)-\bar{\psi}_2(t))\right)\right)^3}{8\omega^3}=0 \end{aligned} \tag{3.18}$$

$$\begin{aligned} &m_a\left(\frac{d}{dt}\psi_2(t)-\frac{1}{2}j\omega(\psi_2(t)+\bar{\psi}_2(t))\right) \\ &+\frac{jk_1\left((\psi_1(t)-\bar{\psi}_1(t))-(\psi_2(t)-\bar{\psi}_2(t))\right)}{2\omega}+\frac{k_3\left(j\left((\psi_1(t)-\bar{\psi}_1(t))-(\psi_2(t)-\bar{\psi}_2(t))\right)\right)^3}{8\omega^3}=0 \end{aligned} \tag{3.19}$$

Substituting Equation (3.17) into Equations (3.18) and (3.19) results in:

$$\begin{aligned} &m_p\left(\frac{d}{dt}(\phi_1(t)e^{j\omega t})-\frac{1}{2}j\omega(\phi_1(t)e^{j\omega t}-\bar{\phi}_1(t)e^{-j\omega t})\right)-\frac{jk_p\left(\phi_1(t)e^{j\omega t}-\bar{\phi}_1(t)e^{-j\omega t}\right)}{2\omega} \\ &-k_1\left(\frac{j\left(\phi_1(t)e^{j\omega t}-\bar{\phi}_1(t)e^{-j\omega t}\right)}{2\omega}-\frac{j\left(\phi_2(t)e^{j\omega t}-\bar{\phi}_2(t)e^{-j\omega t}\right)}{2\omega}\right) \\ &-k_3\left(\frac{j\left(\phi_1(t)e^{j\omega t}-\bar{\phi}_1(t)e^{-j\omega t}\right)}{2\omega}-\frac{j\left(\phi_2(t)e^{j\omega t}-\bar{\phi}_2(t)e^{-j\omega t}\right)}{2\omega}\right)^3=0 \end{aligned} \tag{3.20}$$

$$\begin{aligned} &m_a\left(\frac{d}{dt}(\phi_2(t)e^{j\omega t})-\frac{1}{2}j\omega(\phi_2(t)e^{j\omega t}-\bar{\phi}_2(t)e^{-j\omega t})\right) \\ &+k_1\left(\frac{j\left(\phi_1(t)e^{j\omega t}-\bar{\phi}_1(t)e^{-j\omega t}\right)}{2\omega}-\frac{j\left(\phi_2(t)e^{j\omega t}-\bar{\phi}_2(t)e^{-j\omega t}\right)}{2\omega}\right) \\ &+k_3\left(\frac{j\left(\phi_1(t)e^{j\omega t}-\bar{\phi}_1(t)e^{-j\omega t}\right)}{2\omega}-\frac{j\left(\phi_2(t)e^{j\omega t}-\bar{\phi}_2(t)e^{-j\omega t}\right)}{2\omega}\right)^3=0 \end{aligned} \tag{3.21}$$

Next Equations (3.20) and (3.21) are simplified by keeping the terms with fast frequency ω, and ignoring the higher order terms of $e^{3j\omega t}$ and $e^{5j\omega t}$. Collecting the terms associated with $e^{j\omega t}$ yields:

$$\begin{aligned} & m_p\left(\frac{d}{dt}\phi_1(t)\right)+\frac{1}{2}jm_p\phi_1(t)\omega+\frac{3jk_3}{8\omega^3}(\bar{\phi}_2(t)\phi_1(t)^2+\bar{\phi}_2(t)\phi_2(t)^2-\bar{\phi}_1(t)\phi_1(t)^2-\bar{\phi}_1(t)\phi_2(t)^2) \\ & +\frac{j}{2\omega}\left(k_1(\phi_2(t)-\phi_1(t))-k_p\phi_1(t)\right)+\frac{3jk_3}{4\omega^3}\left(\bar{\phi}_2(t)\phi_2(t)\phi_1(t)-\bar{\phi}_1(t)\phi_1(t)\phi_2(t)\right)=0 \end{aligned} \tag{3.22}$$

$$\begin{aligned} & m_a\left(\frac{d}{dt}\phi_2(t)\right)+\frac{1}{2}jm_a\phi_2(t)\omega+\frac{3jk_3}{8\omega^3}(\bar{\phi}_2(t)\phi_1(t)^2+\bar{\phi}_1(t)\phi_2(t)^2-\bar{\phi}_2(t)\phi_1(t)^2 \\ & -\bar{\phi}_2(t)\phi_2(t)^2)+\frac{j}{2\omega}\left(k_1(\phi_1(t)-\phi_2(t))\right)+\frac{3jk_3}{4\omega^3}\left(\bar{\phi}_2(t)\phi_2(t)\phi_1(t)-\bar{\phi}_1(t)\phi_1(t)\phi_2(t)\right)=0 \end{aligned} \tag{3.23}$$

The representations of polar forms: $\phi_1=a(t)e^{j\alpha(t)}$ and $\phi_2=b(t)e^{j\beta(t)}$ are introduced in Equations (3.22) and (3.23), where $a(t)$ and $b(t)$ are real amplitudes, $\alpha(t)$ and $\beta(t)$ are the real phases. Then by separating the real and the imaginary parts, the four first-order ordinary differential equations are obtained as follow:

$$\dot{a}=\frac{1}{8m_p\omega^3}\left((-b^3k_3-3a^2bk_3-4bk_1\omega^2)\sin(\alpha-\beta)+3ab^2k_3\sin(2\alpha-2\beta)\right) \tag{3.24}$$

$$\begin{aligned} \dot{\alpha}=\frac{1}{8am_p\omega^3}((&-9a^2bk_3-3b^2k_3-4bk_1\omega^2)\cos(\alpha-\beta)+3ab^2k_3\cos(2\alpha-2\beta) \\ &+6ab^2k_3+4ak_1\omega^2+4ak_p\omega^2+3a^3k_3-4am_p\omega^4) \end{aligned} \tag{3.25}$$

$$\dot{b}=\frac{1}{8m_a\omega^3}\left((3a^3k_3+4ak_1\omega^2+3ab^2k_3)\sin(\alpha-\beta)-3a^2bk_3\sin(2\alpha-2\beta)\right) \tag{3.26}$$

$$\begin{aligned} \dot{\beta}=\frac{1}{8bm_a\omega^3}((&-9ab^2k_3-4ak_1\omega^2-3a^3k_3)\cos(\alpha-\beta)+3a^2bk_3\cos(2\alpha-2\beta) \\ &+6a^2bk_3+4bk_1\omega^2+3b^2k_3-4bm_a\omega^4) \end{aligned} \tag{3.27}$$

where the over-dot represents the derivative with respect to time. Due to seeking the periodic solutions, the steady state solutions of the equations above are found by setting Equations (3.25)

to (3.27) to be zero. Further, it is assumed that the system oscillates in phase or $\alpha = \beta$. Thus Equations (3.24) and (3.26) become:

$$0 = \frac{1}{8am_p\omega^3}\left(3k_3(a-b)^3 + 4k_1\omega^2(a-b) + 4ak_p\omega^2 - 4am_p\omega^4\right) \tag{3.28}$$

$$0 = \frac{1}{8bm_a\omega^3}\left(3k_3(b-a)^3 + 4k_1\omega^2(b-a) - 4bm_a\omega^4\right) \tag{3.29}$$

Equations (3.28) and (3.29) are a set of two coupled nonlinear algebraic equations which can be numerically solved for *a* and *b* by specifying frequency ω. After *a* and *b* are obtained, the responses can be expressed as follow:

$$x_p(t) \approx X_p \cos\omega t = \frac{\psi_1 - \bar{\psi}_1}{2j\omega} = \frac{a}{\omega}\cos\omega t \tag{3.30}$$

$$x_a(t) \approx X_a \cos\omega t = \frac{\psi_2 - \bar{\psi}_2}{2j\omega} = \frac{b}{\omega}\cos\omega t \tag{3.31}$$

As the system is conservative, the total energy of the system can be defined by

$$E = \frac{1}{2}k_p X_p^{\,2} + \frac{1}{2}k_1(X_a - X_p)^2 + \frac{1}{4}k_3(X_a - X_p)^4 \tag{3.32}$$

Figure 3.38 is the so-called Frequency Energy Plot (FEP) that is made by using a triplet of *a*, *b* and ω obtained by solving Equations (3.28) and (3.29) with the parameters values of the weakly coupled system. The FEP shows the relationship between the total energies of the system and the frequencies ω of the periodic solutions. The two curves are the so-called the backbone curves of the NNMs, where the backbone branch "S11+" expresses an in-phase oscillation, and the backbone branch "S11−" indicates an out-of-phase oscillation. It is noted that S11+ originates from a low frequency that is very close to the natural frequency f_a of the NES while S11− originates from a high frequency that is close to the natural frequency f_p of the primary system. Finally, the energy

threshold is identified by the arrow in Figure 3.38. For a combined system consisting of a primary system and a true NES, when the initial energy exceeds this threshold, the oscillation is attracted to the S11+ backbone curve and the desired 1:1 resonance is activated. Otherwise, the system will be attracted to the S11− backbone curve and the primary system and NES vibrates at two different frequencies [19].

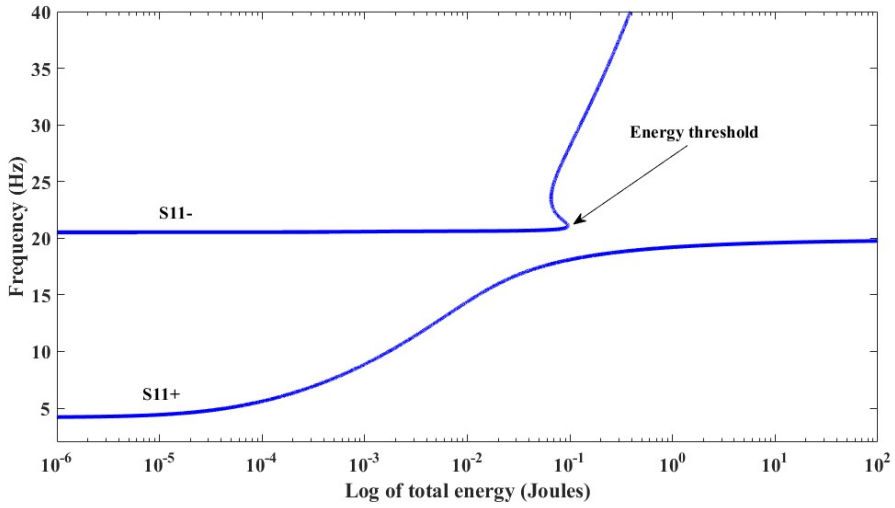

Figure 3.38 Analytic approximations of the frequency energy plot for the weakly coupled system: Backbone curve S11±.

In order to compare the frequency contents of the responses with the backbone curves, the contours of the WT spectrum of the relative displacement is superimposed on the FEP. To this end, the WT spectrum's time axis is matched to the system's total energy determined at each time instant t. The results for the weakly coupled system are shown in Figure 3.39 and Figure 3.40 and the results for the strongly coupled system are shown Figure 3.41 and Figure 3.42

As shown in Figure 3.39 (a), when the low initial energy level is below the energy threshold, the response of the system is not fully attracted to the backbone branch $S11+$. This indicates that the desired 1:1 resonance does not occur. However, after a short period, the energy is concentrated on the backbone branch $S11+$, indicating that the TET is achieved and the energy

is localized in the NES even without the 1:1 resonance, with this initial energy level, the nonlinearity of the NES is less dominant.

As shown in Figure 3.39 (b), with the medium energy level, the initial energy is close to the threshold. The response appears more nonlinear, as revealed by the energy concentration around both the backbone branches $S11-$ and $S11+$ in the beginning. After a short period of time, the energy concentration starts follow the $S11+$curve and ends at the frequency components around f_a. This indicates that the 1:1 resonance and the TET are partially established.

Figure 3.39 (c) and Figure 3.39 (d) show the cases of the high-energy level and the case of the extra high-energy level (which will be explained in the next figure), respectively. Both of the initial energy levels pass the energy threshold. As a result, the oscillation energy is rapidly attracted to the $S11+$ curve so that a dominant 1:1 resonance appears and the desired TET is established. With the increase of the initial energy level, the NES demonstrates the desired nonlinear manner.

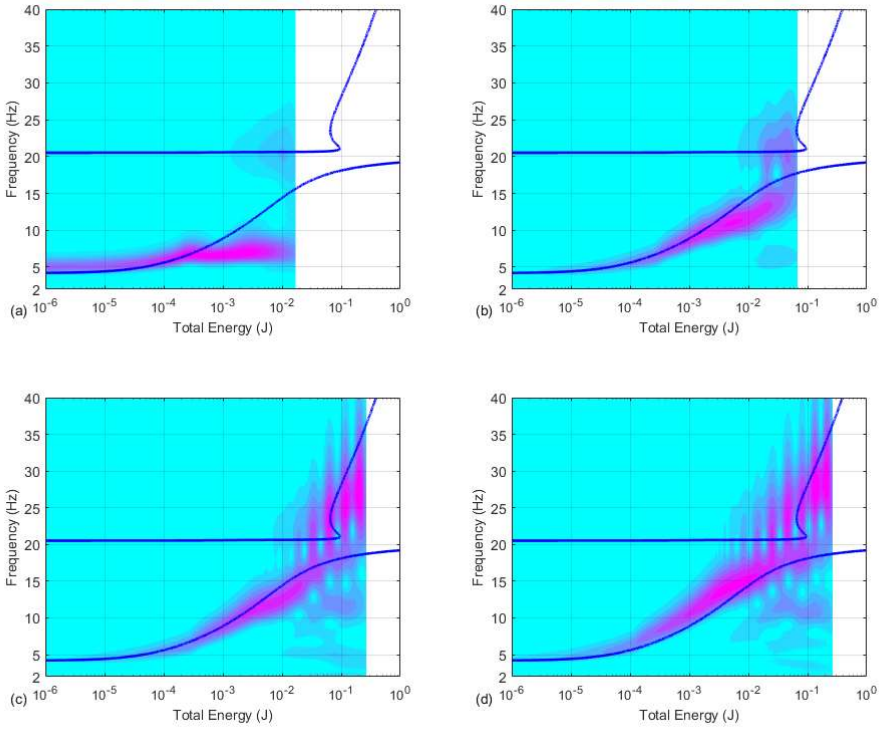

Figure 3.39 Frequency energy plots and wavelet transforms of relative displacement x_a-x_p from the simulation results: (a) low-energy level X =2.5 mm; (b) medium-energy level X = 5 mm; (c) high-energy level X = 10 mm and (d) extra high-energy level X = 13 mm.

Figure 3.40 shows the FEPs of the experimental results. Figure 3.40 (a) shows that at the low-energy level, the vibration energy mainly concentrates around f_a, similar to Figure 3.39 (a). This indicates that the 1:1 resonance is not triggered, but the TET is established. However, the nonlinearity of the NES is not activated. Figure 3.40 (b) shows that with an increase of the initial energy level, the vibration energy concentration starts to follow the backbone curve $S11+$. The oscillation energy concentration originates around the frequency 7.5 Hz and gradually sets down around f_a. This indicates that the TET is triggered without the 1:1 resonance. Figure 3.40 (c) shows the case of the high energy level. The initial energy level is still below the threshold. The response appears more nonlinear, as indicated by the response energy concentration around the $S11+$ curve.

Comparing Figure 3.39 (a) to (c) reveals that the energy levels of the responses from the experiments are lower than those of the responses from the computer simulation. This is due to the fact that the stiffer the primary system, the more difficult to fully excite it with a large initial displacement. By closely inspecting Figure 3.25 and Figure 3.27, one can note that the primary system oscillates to a magnitude that is much lower than the initial displacement after it is released. To confirm the trend of the response energy concentration, an extra high-energy level is introduced by setting X = 13.25 mm. Figure 3.40 (d) shows the results. As it can be seen, although the initial energy still cannot exceed the threshold level, the response energy become more dominantly concentrated along the $S11+$ backbone. This indicates that the NES behaves strongly nonlinearity and the TET is quickly established.

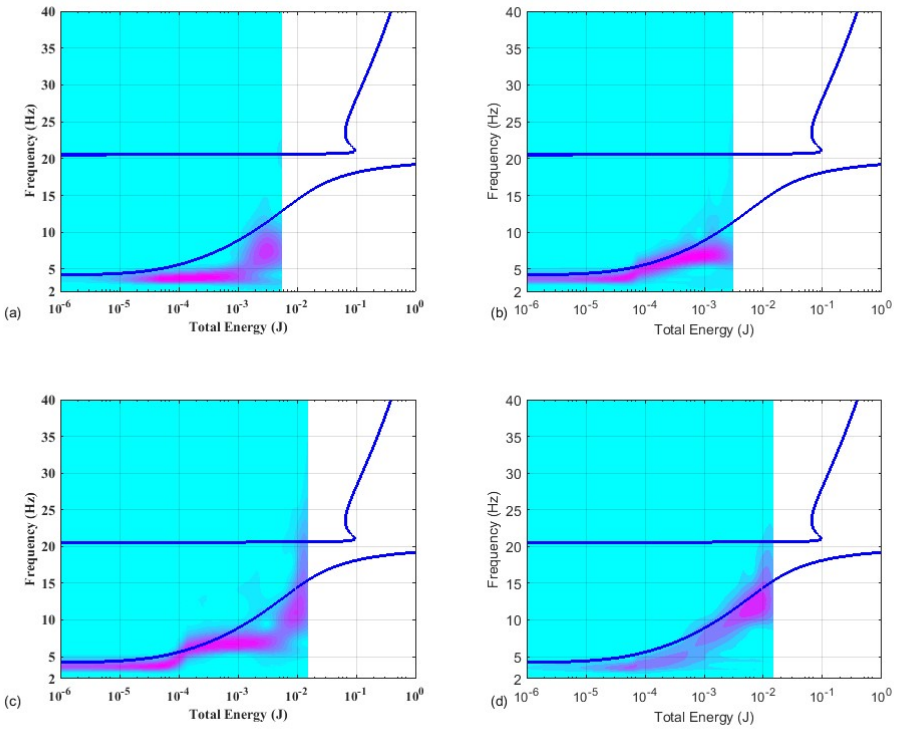

Figure 3.40 Frequency energy plots and wavelet transforms of relative displacement x_a-x_p from the experimental results: (a) low-energy level X =2.48 mm; (b) medium-energy level X =5.03 mm; (c) high-energy level X =10.29 mm and (d) extra high-energy level X =13.25 mm.

Figure 3.41 shows the FEPs of the responses obtained by computer simulation with the strongly coupled system. Figure 3.41 (a) shows that the response energy concentrates around f_a and f_p in the beginning and sets down to f_a eventually. Figure 3.41 (b), (c) and (d) confirm the trend that when the initial energy level exceeds the threshold, the 1:1 resonance occurs and the response energy is attracted to the backbone $S11+$ curve. It is also noted that the nonlinear beats exist in all of the three cases, indicating that the energy is exchanged back and forth between the primary system and NES.

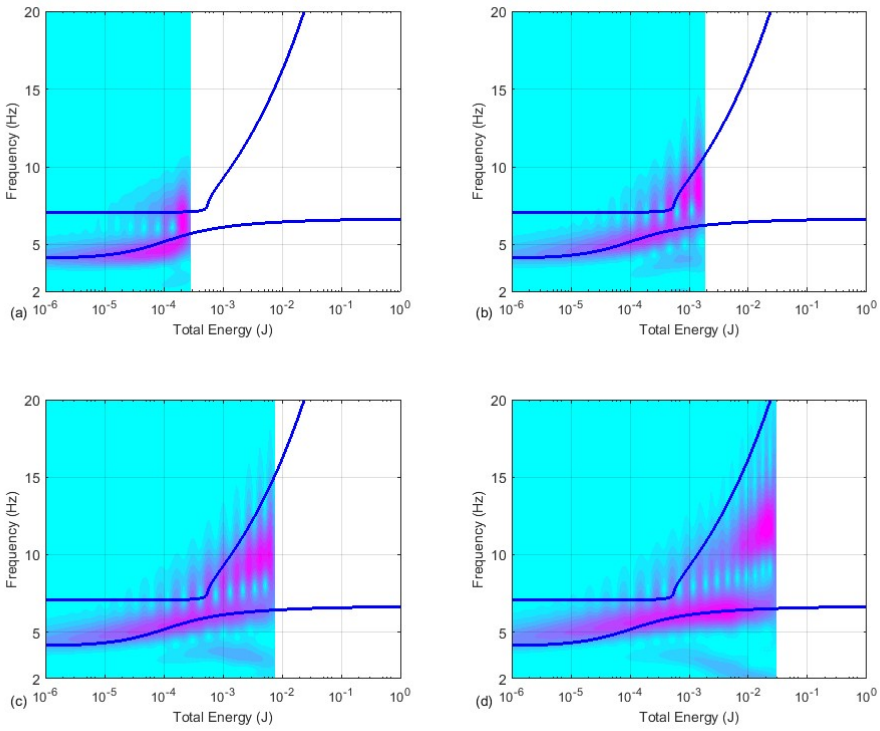

Figure 3.41 Frequency energy plots and wavelet transforms of relative displacement x_a-x_p from the simulation results: (a) extra low-energy level X =1 mm; (b) low-energy level X =2.5 mm; (c) medium-energy level X =5 mm and (d) high-energy level X =10 mm.

Figure 3.42 shows the FEPs of the responses obtained experimentally with the strongly coupled system. The results are similar as to those shown in Figure 3.41, validating that the oscillation energy concentrates on the $S11+$ backbone curve when the initial energy level

exceeds the energy threshold. Comparing Figure 3.42 and Figure 3.40 reveals that the TET establishment in the strongly coupled system is accompanied by the nonlinear beats.

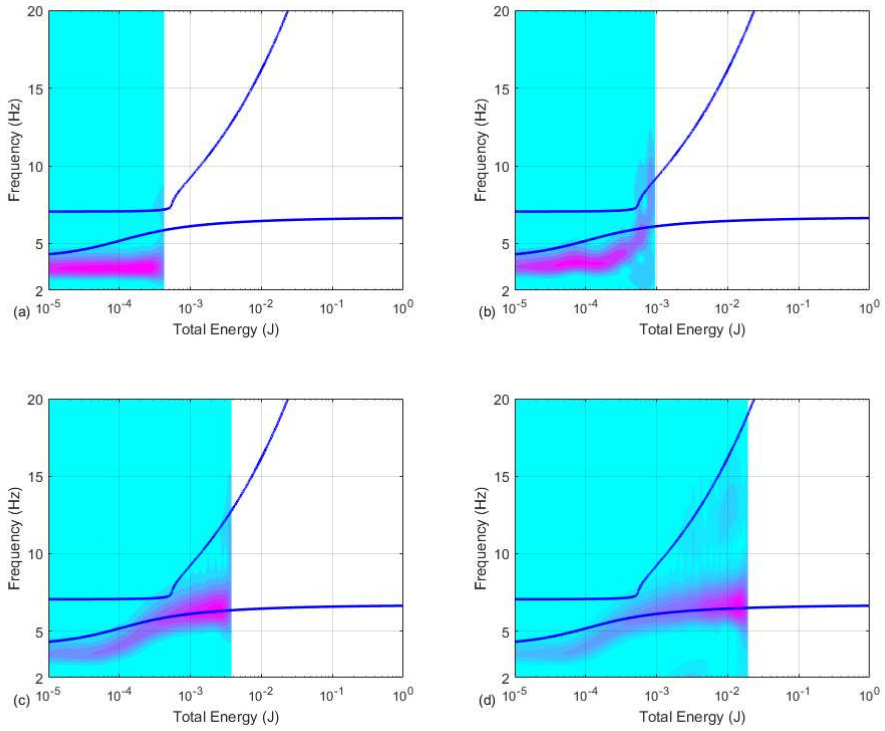

Figure 3.42 Frequency energy plots and wavelet transforms of relative displacement x_a-x_p from the experimental results: (a) extra low-energy level X =1.08 mm; (b) low-energy level X =2.55 mm; (c) medium-energy level X =5.19 mm and (d) high-energy level X =10.14 mm.

3.6 Conclusion

In this chapter, the transient behaviors of the variant NES have been studied. Both the weakly coupled system and strongly coupled system are investigated through simulations and experiments. From the results given above, several conclusions are obtained as follow. Firstly, in order to activate the combined system into the 1:1 resonance and to achieve the TET, the oscillation energy of the combined system should exceed the critical energy threshold. Second, the weakly coupled system gives a better performance than the strongly coupled system in terms of the 1:1

resonance and TET. Finally, the accumulated energy capture of the weakly coupled system is greater than that of the strongly coupled system. Overall, the weakly coupled system is a better choice to activate the NES system and to establish the TET.

Chapter 4 Harmonically forced responses

4.1 Simulation of harmonically forced responses

In the study presented in [43], a software called Matcont was used in the study of harmonically forced responses of the combined system. The software uses the continuation method to find the approximate steady-state solutions of the primary and NES systems under harmonic excitation. In this study, ODE 45, a MATLAB built in function is used for the numerical simulation study. As in [43], it is of interest to investigate the phenomena of the saddle-node and Hopf bifurcation regions, where the saddle region indicates the presence of multiple solutions while the Hopf bifurcation region reveals the strongly modulated responses. The equations of motion with a harmonic base excitation are defined by

$$m_a(\ddot{z}+\ddot{x}_p)+c_a\dot{z}+k_1z+k_3z^3+\theta V=-m_a\ddot{y} \tag{4.1}$$

$$m_p\ddot{x}_p+c_p\dot{x}_p+k_px_p-\left(c_a\dot{z}+k_1z+k_3z^3+\theta V\right)=-m_p\ddot{y} \tag{4.2}$$

$$\frac{V}{R}+C^s\dot{V}-\theta\dot{z}=0 \tag{4.3}$$

where $\ddot{y}=-\Omega^2Y\cos(\Omega t)$ is the acceleration of the base with an amplitude defined as $A_y=\Omega^2Y$ in which Ω is the excitation frequency and Y is the amplitude of the base motion, and the other variables have been defined in Chapter 2. The parameter values used in the following simulation are the same as those used in Chapter 3

For the harmonically excitation, the focus is on the steady state responses. As the system is nonlinear, its responses to single frequency harmonic excitation depend on the initial conditions in certain frequency ranges. One of the methods to deal with this problem is to conduct Monte

Carlo simulations of the steady state responses for different values of randomly picked initial conditions. This method is very time-consuming. In this study, a slow frequency sweep excitation is used to generate the so-called frequency response plots (FRPs) [44]. In particular, a chirp sweep is used. The instantaneous exciting frequency is determined by

$$f = f_s + \frac{f_e - f_s}{T} t \tag{4.4}$$

where f_s is the starting frequency, f_e is the ending frequency, $T = (f_e - f_s)/r$ is the sweep duration and r is the sweeping-rate. In an upsweep, f_s = 4 Hz, f_e = 25 Hz and r = 0.02 Hz/s while in a downsweep, f_s = 25 Hz, f_e = 4 Hz and r =– 0.02 Hz/s.

4.1.1 Harmonically forced responses of the weakly coupled system

Figure 4.1, Figure 4.2 and Figure 4.3 show the upsweep and downsweep frequency responses of the weakly coupled system subjected to base excitation with the three accelerations A_y = 1.0, 1.5 and 2.0 m/s^2, respectively. The load resistance is R = 20 kΩ. In all the figures, there are two frequency regions of interest. The first one is referred to low frequency region that is between 6.2 Hz and 18.2 Hz while the second one is referred to as high frequency region that centers around 20.5 Hz. In the high frequency region, the downsweep FRPs appear similar for all the three excitation levels. However, the upsweep FRP shows jumping when A_y = 1 m/s^2. But the jumping phenomenon becomes less visible when A_y = 2 m/s^2 is too high to attainable physically for the real apparatus. The responses peak around 20.5 Hz without jumping while the response amplitudes increase with the increase of the excitation level. The low frequency region can be considered as a broadband frequency region with the occurrence of the jump phenomenon. For all three excitation levels, the responses jump from a high state to a low state in the upsweep while the responses jump from a low state to a high state in the downsweep. The responses between the jump frequencies depend on initial conditions or disturbances. They may appear as the so-called strongly

modulated responses (SMRs) [63]. In Figure 4.1, the two jumping frequencies are found around 6.21 Hz and 17.10 Hz, respectively. Figure 4.2 shows that the jumping frequencies are around 6.73 Hz and 17.79 Hz, respectively. With the increase of the excitation level, the low frequency region is widened. Figure 4.3 indicates the jumping frequencies are around 7.2 Hz and 18.2 Hz, respectively, indicating that the low frequency region expands with an increase in the acceleration level.

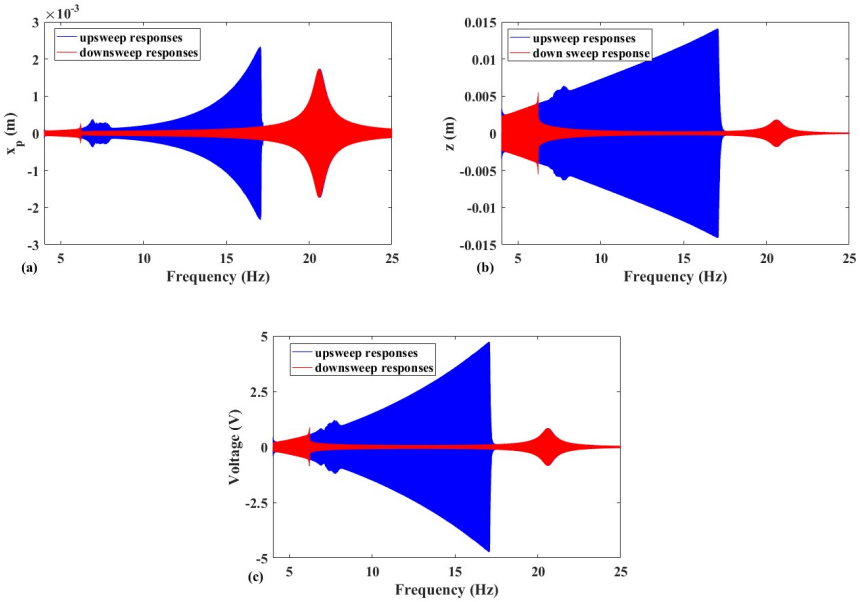

Figure 4.1 Frequency responses of the weakly coupled system under the base excitation of A_y = 1 m/s^2: (a) x_p; (b) z and (c) v (Blue line is the up sweep responses; Red line is the down sweep responses).

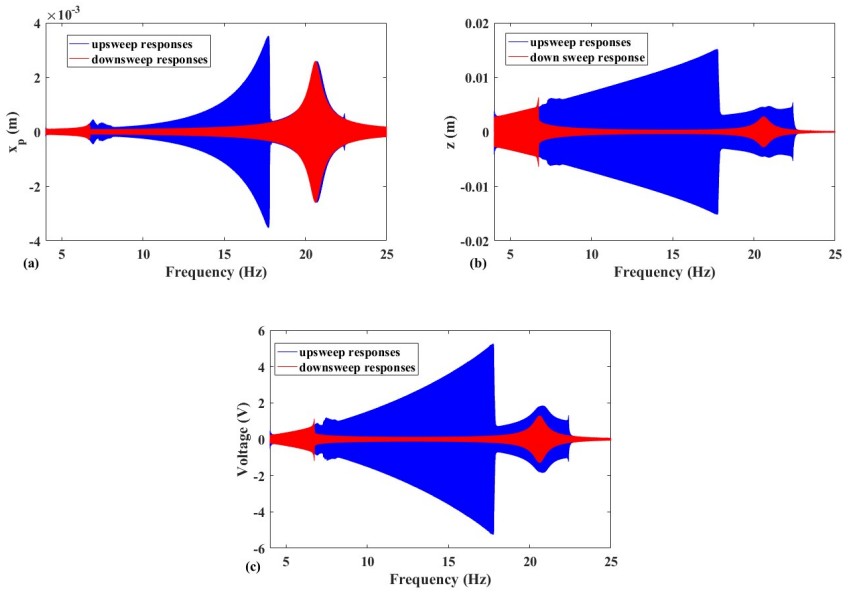

Figure 4.2 Frequency responses of the weakly coupled system under the base excitation of A_y = 1.5 m/s^2: (a) x_p; (b) z and (c) v (Blue line is the up sweep responses; Red line is the down sweep responses).

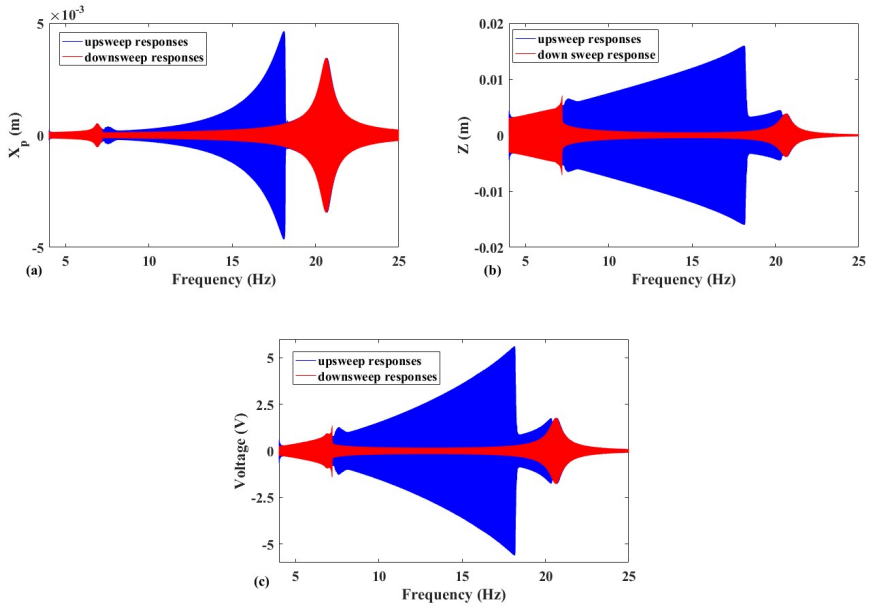

Figure 4.3 Frequency responses of the weakly coupled system under the base excitation A_y = 2 m/s^2: (a) x_p; (b) z and (c) v (Blue line is the up sweep responses; Red line is the down sweep responses).

Figure 4.4, Figure 4.5 and Figure 4.6 show the upsweep and downsweep voltage responses of the weakly coupled system subjected to the three base excitation levels with the five load resistances of R = 20, 50, 100, 200, 1000 kΩ. In all the figures, jumping phenomena occur in the low frequency region and the generated voltages increase with the increase in the value of the load resistance.

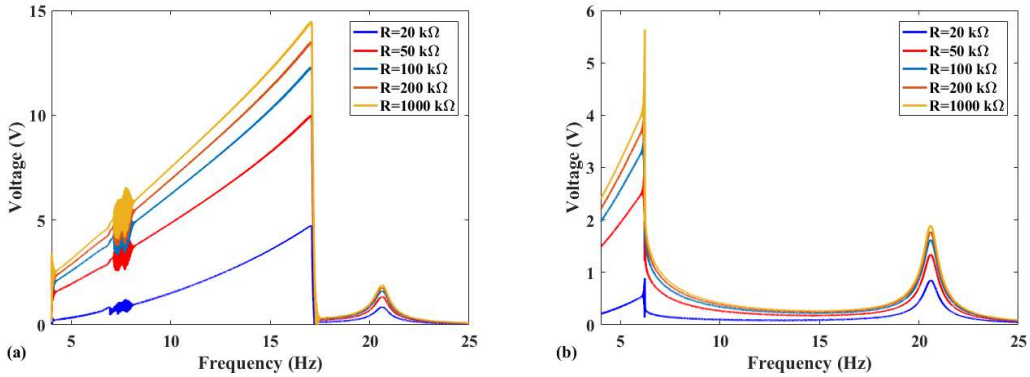

Figure 4.4 Voltage responses with five load resistances under the base excitation of A_y = 1 m/s^2 (a) upsweep excitation; (b) downsweep excitation (blue line: 20 kΩ, red line: 50 kΩ, cyan line: 100 kΩ, magenta line: 200 kΩ, yellow line: 1000 kΩ).

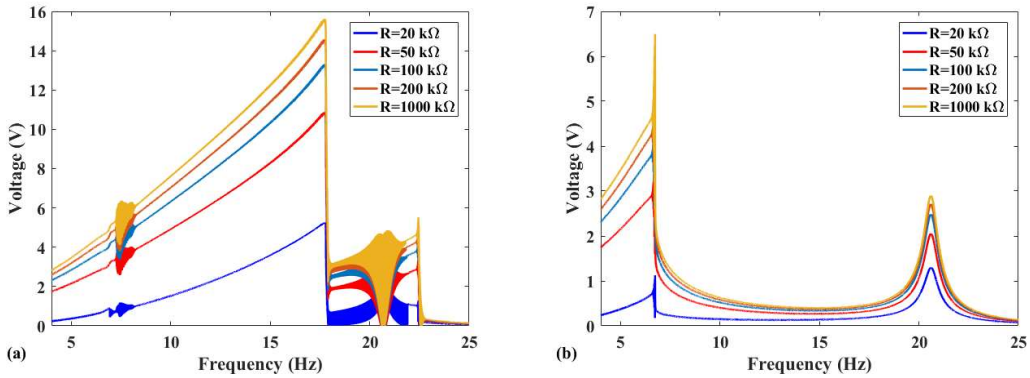

Figure 4.5 Voltage responses with five load resistances under the base excitation of A_y = 1.5 m/s^2 (a) upsweep excitation; (b) downsweep excitation (blue line: 20 kΩ, red line: 50 kΩ, cyan line: 100 kΩ, magenta line: 200 kΩ, yellow line: 1000 kΩ).

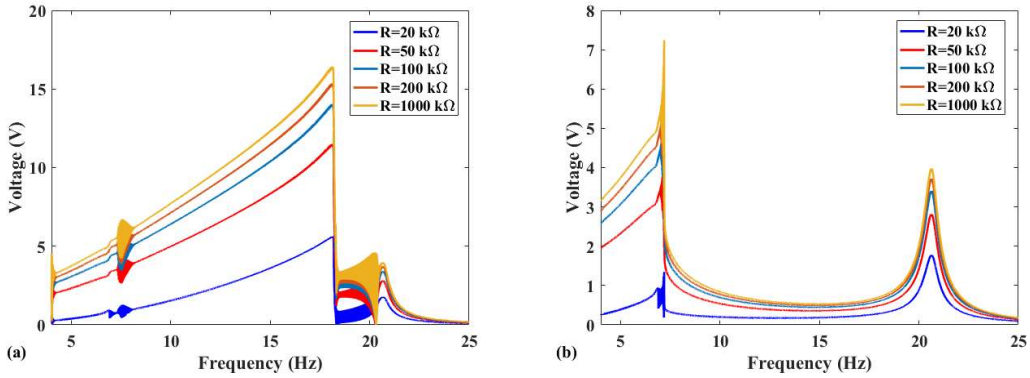

Figure 4.6 Voltage responses with five load resistances under the base excitation of $A_y = 2$ m/s^2 (a) upsweep excitation; (b) downsweep excitation (blue line: 20 kΩ, red line: 50 kΩ, cyan line: 100 kΩ, magenta line: 200 kΩ, yellow line: 1000 kΩ).

As mentioned in the previous study [43], the system under harmonic excitation may experience the weakly modulated responses or more importantly the strongly modulated responses (SMRs). Due to the nonlinearity of the NES system, the nonlinear beating may be found when the exciting frequency is close to the natural frequency of the NES system. Figure 4.7 shows the responses of the system excited at $f = 6.5$ Hz, indicating that the beating phenomena are found while the SMRs are not obtained. Basically, the nonlinearity can be observed when the oscillation amplitude is high enough. Figure 4.8 shows that when the acceleration level is dramatically increased to $A_y = 10$ m/s^2 when the SMRs appear. Figure 4.9 shows another typical SMR when the system is excited at $f = 7.52$ Hz.

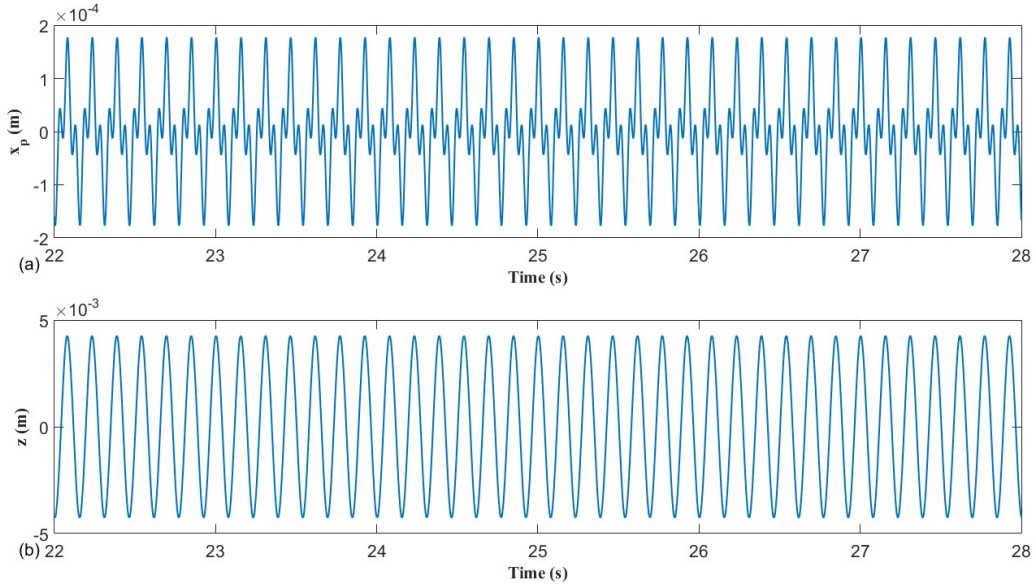

Figure 4.7 Response subjected to A_y = 1 m/s^2 and f = 6.5 Hz: (a) x_p; (b) z.

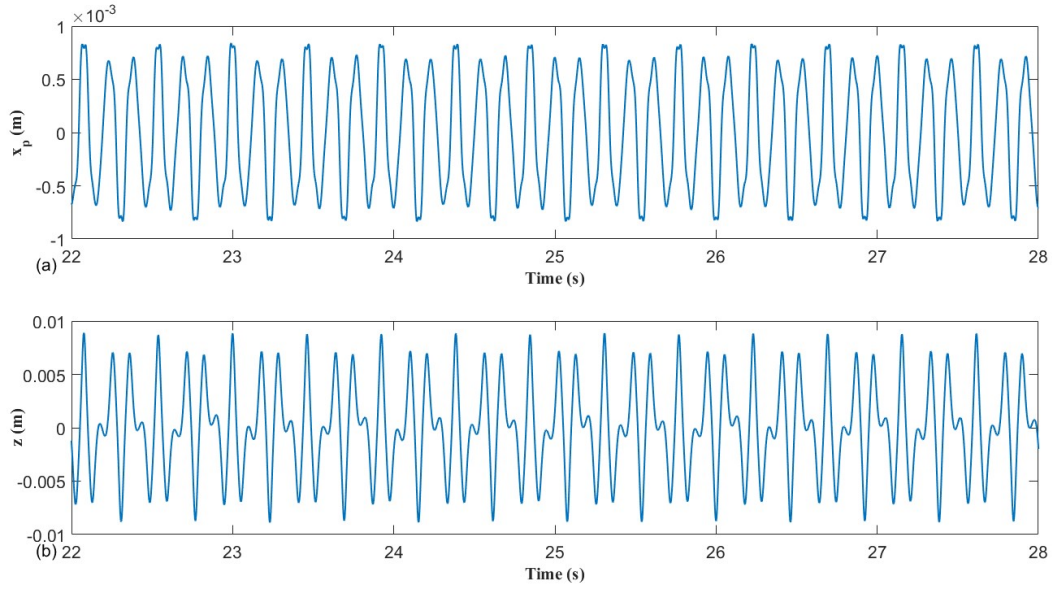

Figure 4.8 Response subjected to A_y = 10 m/s^2 and f = 6.5 Hz: (a) x_p; (b) z.

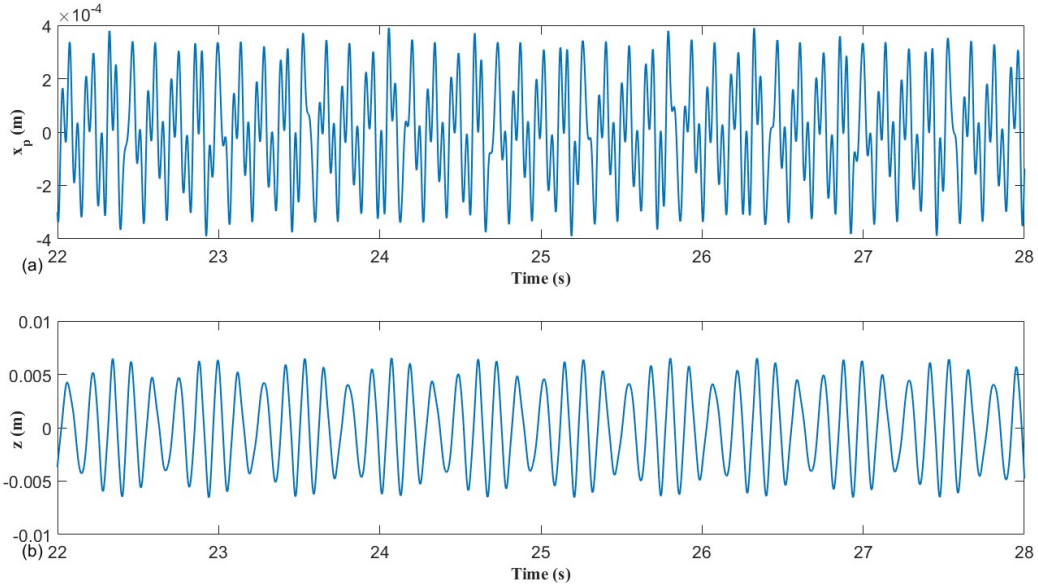

Figure 4.9 Response subjected to $A_y = 2$ m/s^2 and $f = 7.5$ Hz: (a) x_p; (b) z.

4.1.2 Harmonically forced responses of the strongly coupled system

Figure 4.10, Figure 4.11 and Figure 4.12 show the upsweep and downsweep frequency responses of the strongly coupled system subjected to base excitation with the three accelerations $A_y = 0.5$, 0.75 and 1.0 m/s^2, respectively. The load resistance is $R = 20$ kΩ. Due to that the rigidity of the strongly coupled system is much lower than that of the weakly coupled system, lower excitation level must be used to limit the responses within a realistic level. The excitation levels are chosen so that $|z| \le 0.015$ m . As a result, the acceleration levels are reduced. In all the figures, the low frequency region centers around 6.5 Hz while the high frequency region that is between 7.6 and 8.8 Hz. For all excitation levels, the upsweep and downsweep FRPs appear similar in the low frequency region. The responses peak around 6.5 Hz without jumping while the response amplitudes increase with the increase in the excitation level. The high frequency region can be considered as a broadband frequency region with the occurrence of the jump phenomenon. For all excitation levels, the responses jump from a high state to a low state in the upsweep while the responses jump from a low state to a high state in the downsweep. The responses between the jump

frequencies may appear as the strongly modulated responses, similar to the low frequency region of the weakly coupled system. In Figure 4.10, the two jumping frequencies are found around 7.66 and 8.35 Hz, respectively. Figure 4.11 shows that the jumping frequencies are around 7.87 and 8.578 Hz, respectively. Figure 4.12 indicates the jumping frequencies are around and 8.80 Hz, respectively, indicating that the low frequency region keeps expanding with the increase in the acceleration level.

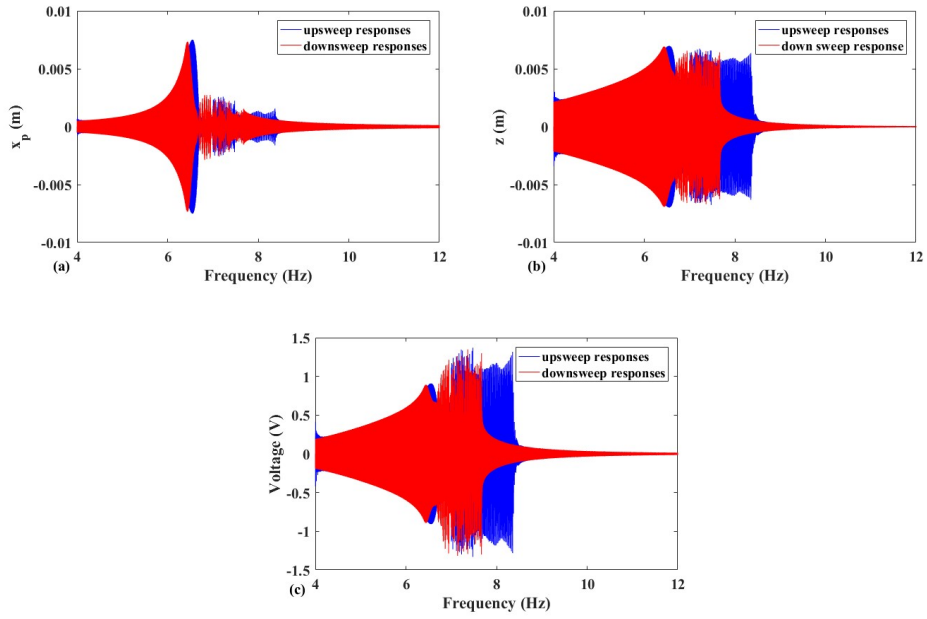

Figure 4.10 Frequency responses of the strongly coupled system under the base excitation of $A_y = 0.5$ m/s^2: (a) x_p; (b) z and (c) v (Blue line: the upsweep responses; Red line: the downsweep responses).

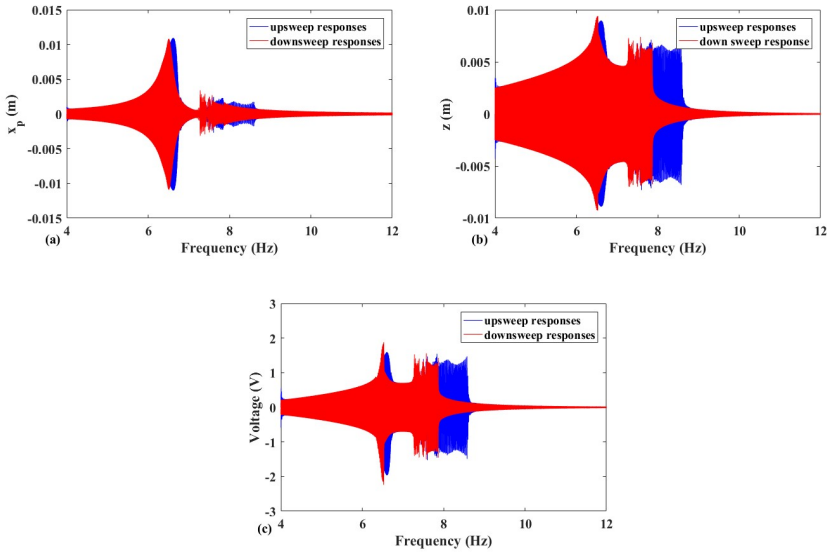

Figure 4.11 Frequency responses of the strongly coupled system under the base excitation of $A_y = 0.75$ m/s^2: (a) x_p; (b) z and (c) v (Blue line: the upsweep responses; Red line: the downsweep responses).

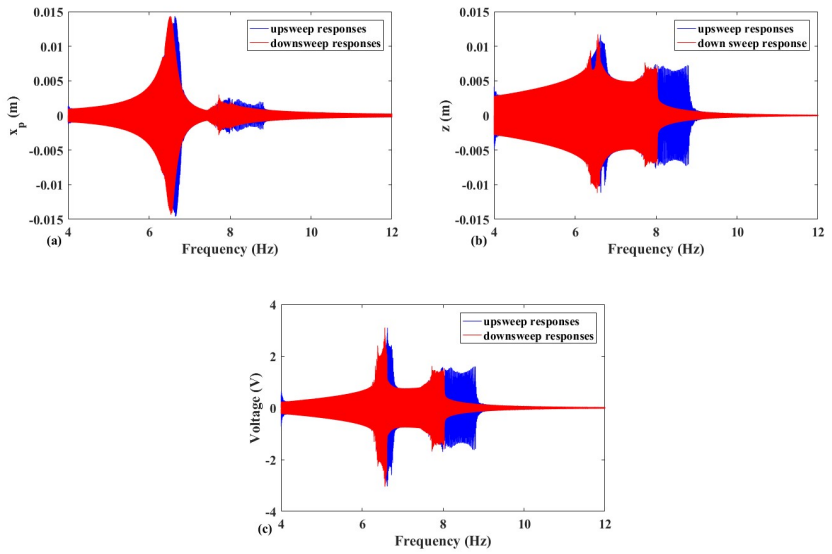

Figure 4.12 Frequency responses of the strongly coupled system under the base excitation of $A_y = 1$ m/s^2: (a) x_p; (b) z and (c) v (Blue line: the upsweep responses; Red line: the downsweep responses).

Figure 4.13, Figure 4.14 and Figure 4.15 show the upsweep and downsweep voltage responses of the strongly coupled system, subjected to the three base excitation levels. Five load resistance

R = 20, 50, 100, 200, 1000 kΩ are considered. In all the figures, jumping phenomena occur in the high frequency region and the generated voltages increase with the increase in the load resistance. It is noted that the voltage responses are very complicated around 6.5 Hz and the jumping frequencies.

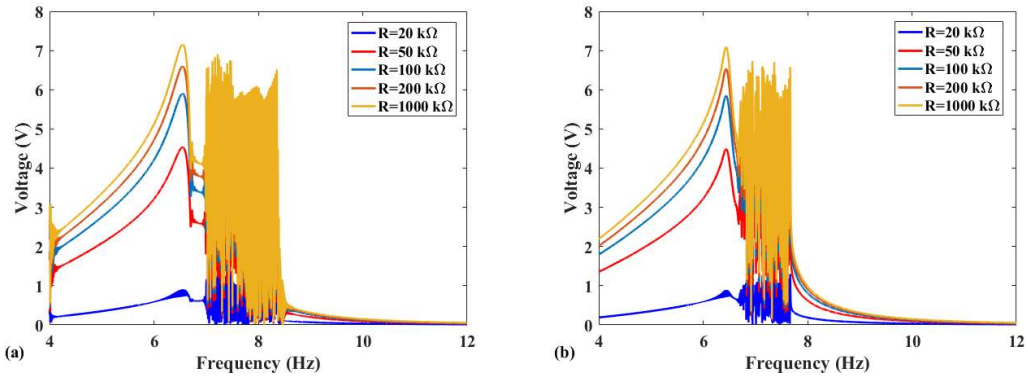

Figure 4.13 Voltage responses with five load resistances under the base excitation of A_y = 0.5 m/s^2 (a)upsweep excitation; (b) downsweep excitation (blue line: 20 kΩ, red line: 50 kΩ, cyan line: 100 kΩ, magenta line: 200 kΩ, yellow line: 1000 kΩ).

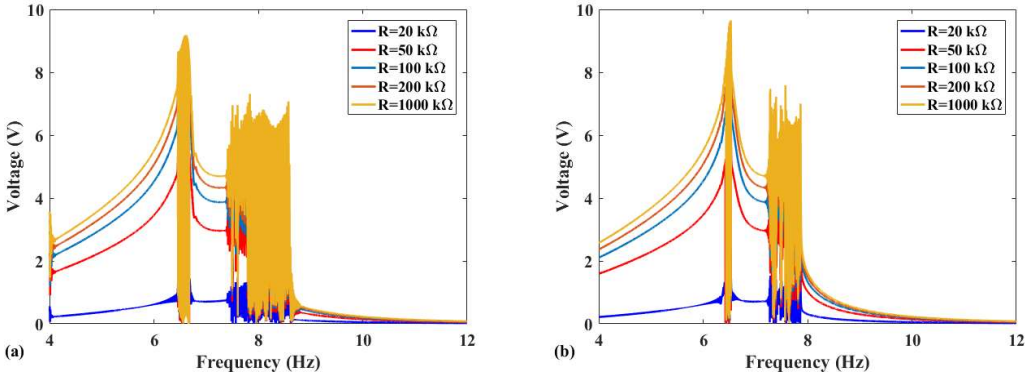

Figure 4.14 Voltage responses with five load resistances under the base excitation of A_y = 0.75 m/s^2 (a)upsweep excitation; (b) downsweep excitation (blue line: 20 kΩ, red line: 50 kΩ, cyan line: 100 kΩ, magenta line: 200 kΩ, yellow line: 1000 kΩ).

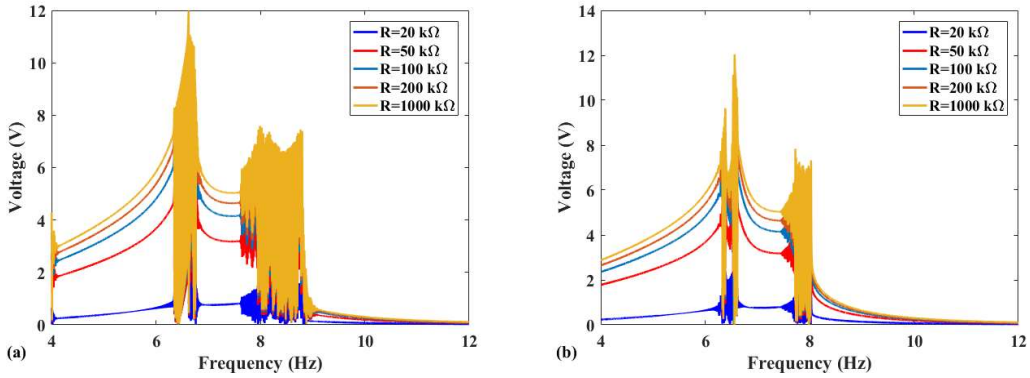

Figure 4.15 Voltage responses with five load resistances under the base excitation of $A_y = 1$ m/s^2 (a)upsweep excitation; (b) downsweep excitation (blue line: 20 kΩ, red line: 50 kΩ, cyan line: 100 kΩ, magenta line: 200 kΩ, yellow line: 1000 kΩ).

Figure 4.16 shows the responses of the system excited at $f = 7$ Hz, indicating that the SMRs are found. Within the region of the two jumping frequencies, the responses with the excited frequency at $f = 7.5$ Hz are shown in Figure 4.17, indicating the beating phenomenon and the SMRs.

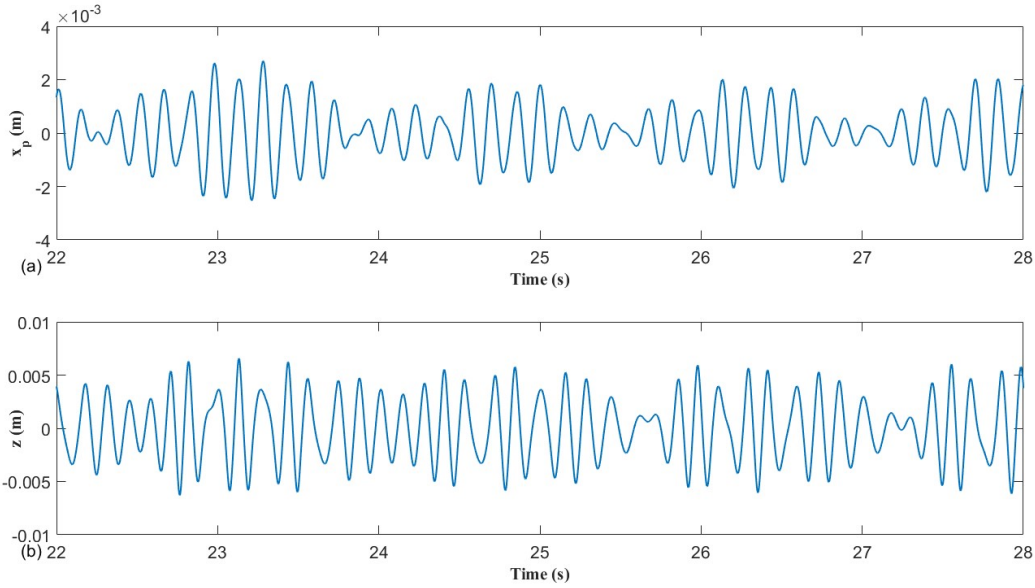

Figure 4.16 Response subjected to $A_y = 0.5$ m/s^2 and $f = 7$ Hz: (a) x_p; (b) z.

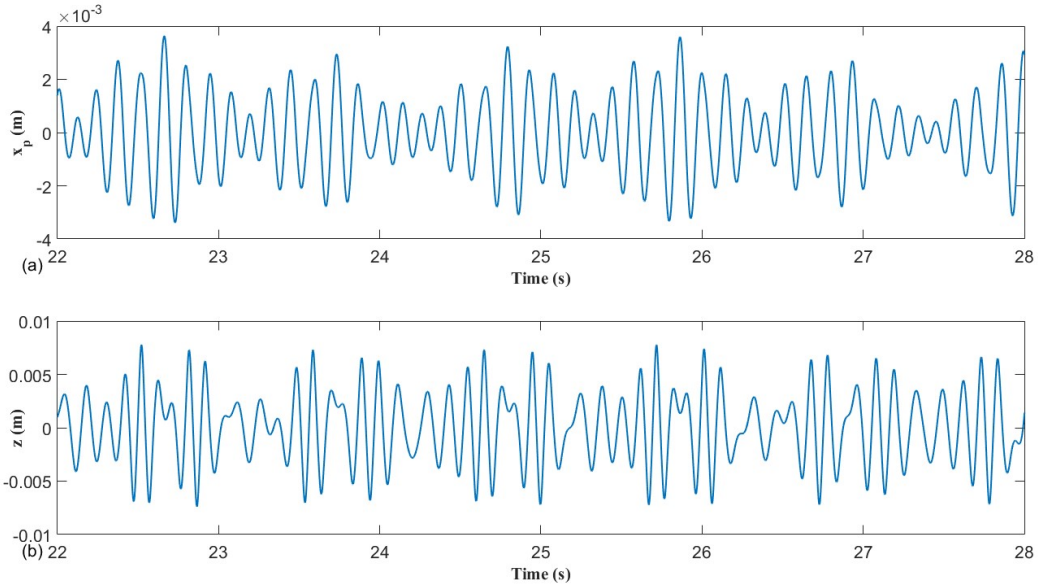

Figure 4.17 Response subjected to $A_y = 1$ m/s^2 and $f = 7.5$ Hz: (a) x_p; (b) z.

4.2 Experimental results of the weakly coupled system

Figure 4.18 contains photograph of the testing setup. Three laser reflex (RF) sensors on the left are used to measure the displacement of the primary mass, the NES mass and the base, respectively. A variable load resistor is connected to the piezoelectric energy harvester by two wires. The load resistance is set to be $R = 20$ kΩ . The base of the apparatus is fixed on a slipping table in the bottom that is driven by the shaker (Brüel & Kjær model 2809) through a stinger. A power amplifier (Brüel & Kjær model 2718) is used to power the shaker. And a dSPACE CLP1104 data acquisition board collects data from the RF sensors and sends an exciting voltage signal to the power amplifier. The dSPACE Controldesk interface is used to control the testing system and save the experimental data.

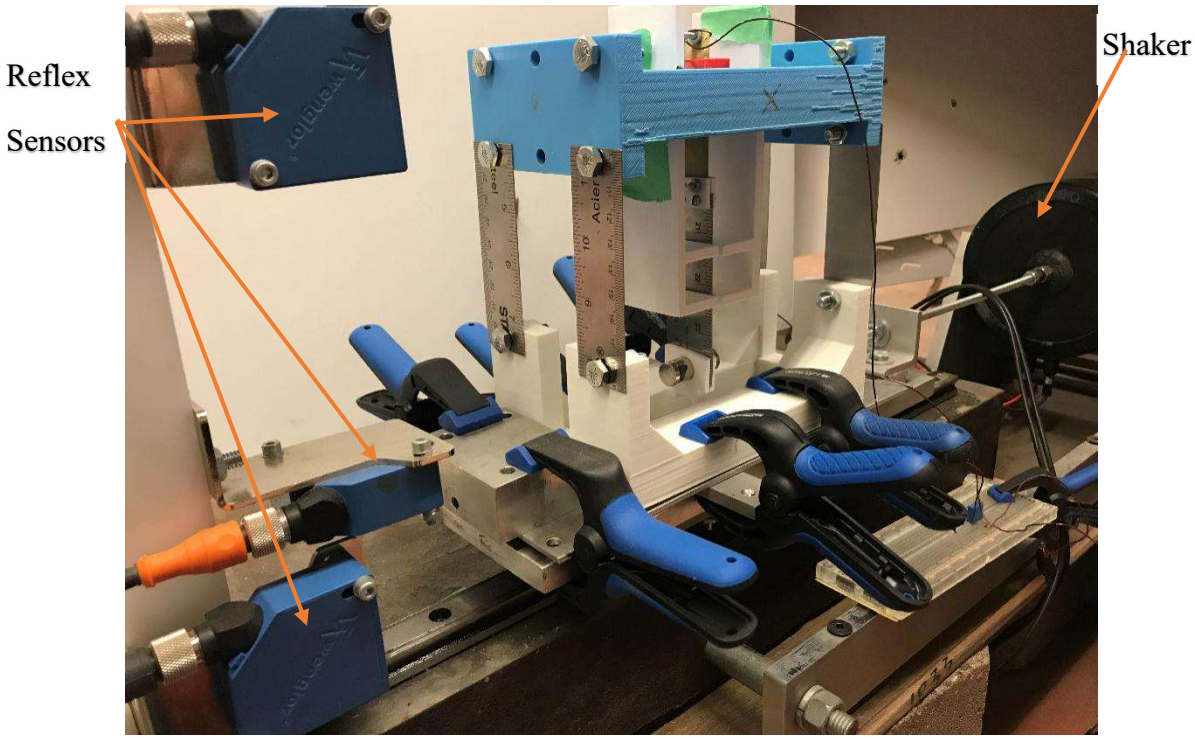

Figure 4.18 Photo of the testing setup of the weakly coupled system.

To generate a harmonic base motion with a constant acceleration for frequency sweep, it is required to find the relationship between the base acceleration and magnitude of the exciting voltage signal that is sent to the power amplifier for each of the exciting frequencies. The voltage magnitude is varied from 0.2 V to 1.0 V in an increment of 0.025 V. For each voltage magnitude, the base displacement is recorded after the responses become steady. The acceleration of the base motion is computed by numerical differentiation. By repeating the process for all the voltage magnitudes, a linear relationship between the voltage magnitude and acceleration amplitude is obtained by curve fitting. This procedure was repeated for each frequency between 4 and 25 Hz with a increment of 0.5 Hz. Table 4.1 to Table 4.5 list the obtained results for the three acceleration amplitudes.

Table 4.1 The exciting voltage magnitudes (V) for the frequency in the range of 4 Hz to 8 Hz

Base acceleration	4 Hz	4.5 Hz	5 Hz	5.5 Hz	6 Hz	6.5 Hz	7 Hz	7.5 Hz	8 Hz
1.0 m/s^2	0.7631	0.5126	0.4484	0.3862	0.3241	0.2803	0.2690	0.2394	0.2214
1.5 m/s^2	1.1105	0.7394	0.6311	0.5417	0.4522	0.3881	0.3712	0.34	0.3113
2.0 m/s^2	1.4579	0.9662	0.8139	0.6971	0.5804	0.4958	0.4734	0.4405	0.4011

Table 4.2 The exciting voltage magnitudes (V) for the frequency in the range of 8.5 Hz to 12.5 Hz

Base acceleration	8.5 Hz	9 Hz	9.5 Hz	10 Hz	10.5 Hz	11 Hz	11.5 Hz	12 Hz	12.5 Hz
1.0 m/s^2	0.2012	0.1868	0.1838	0.1834	0.1909	0.1912	0.1939	0.1952	0.1882
1.5 m/s^2	0.2924	0.2811	0.2782	0.2729	0.2766	0.2809	0.288	0.2956	0.2984
2.0 m/s^2	0.3836	0.3753	0.3725	0.3624	0.3624	0.3705	0.382	0.3961	0.4086

Table 4.3 The exciting voltage magnitudes (V) for the frequency in the range of 13 Hz to 17 Hz

Base acceleration	13 Hz	13.5 Hz	14 Hz	14.5 Hz	15 Hz	15.5 Hz	16 Hz	16.5 Hz	17 Hz
1.0 m/s^2	0.1698	0.1896	0.16	0.1948	0.1978	0.21	0.2033	0.2381	0.2893
1.5 m/s^2	0.2906	0.3188	0.298	0.3481	0.3671	0.3924	0.4048	0.457	0.5201
2.0 m/s^2	0.4114	0.4481	0.4362	0.5014	0.5363	0.5748	0.6062	0.6758	0.7508

Table 4.4 The exciting voltage magnitudes (V) for the frequency in the range of 17.5 Hz to 21.5 Hz

Base acceleration	17.5 Hz	18 Hz	18.5 Hz	19 Hz	19.5 Hz	20 Hz	20.5 Hz	21 Hz	21.5 Hz
1.0 m/s^2	0.3386	0.3991	0.4658	0.5202	0.3221	0.1626	0.1894	0.1915	0.2038
1.5 m/s^2	0.5686	0.6163	0.6923	0.7760	0.7147	0.3596	0.283	0.2899	0.3257
2.0 m/s^2	0.7986	0.8335	0.9188	1.0319	1.1072	0.5565	0.3766	0.3883	0.4477

Table 4.5 The exciting voltage magnitudes (V) for the frequency in the range of 22 Hz to 25 Hz

Base acceleration	22 Hz	22.5 Hz	23 Hz	23.5 Hz	24 Hz	24.5 Hz	25 Hz
1 m/s^2	0.2144	0.2217	0.2257	0.2272	0.2328	0.246	0.2677
1.5 m/s^2	0.3582	0.3723	0.3897	0.406	0.4264	0.4545	0.489
2.0 m/s^2	0.5019	0.5228	0.5537	0.5847	0.62	0.6629	0.7103

In the testing, frequency sweep excitation is carried out incrementally instead continuously. The frequency sweep test starts from 4 Hz and ends at 25 Hz with a step of 0.5 Hz. At each of the frequencies, a harmonic voltage signal with the magnitude corresponding to the desired base acceleration is sent to the power amplifier to drive the shaker. After the responses become steady state, they are recorded for 30 seconds. After removing the offset of each responses, the root-mean-square (RMS) value of each response is used to represent its magnitude. The responses are classified as high state and low state. If the cantilever beam hits the stop blocks, the responses are referred to as high state. On the other hand, if the cantilever beam does not hit the blocks, the responses are referred to as low state. Figure 4.19, Figure 4.20 and Figure 4.21 show the FRPs of

the primary mass's displacement, the NES mass's relative displacement, and the load resistor's voltage for the three base acceleration levels. In the figures, blue squares only represent the high state while red circles only represent the low state. A frequency region where both the states exist is the so-called jumping region. There are two types of jumping. In the first type, a low state can jump up to a high state by tapping the NES mass gently or a high state can jump down to a low state by holding the NES mass temporarily. In the second type, the high state can automatically switch to the low state after a long period. The time duration required by such a switching is random and unpredictable. When a data point is marked by both a blue square and red circle, it may be a low state or high state, which is stable, i.e., no jumping.

Figure 4.19 shows the experimental results with the acceleration A_y = 1 m/s^2. Figure 4.19 (b) clearly shows that there are three jumping regions 6 to 11 Hz, 14 to 15.5 Hz, and 23 to 24.5 Hz. The first region belongs to the first type of jumping. Within this region, the high state responses may appear as the SMRs. The next two regions belong to the second type of jumping. Within these two regions, the high state responses may appear as the SMRs as well. Comparing these results with those in Figure 4.1, the testing somewhat validates the jumping phenomenon revealed in the simulation. Figure 4.19 (c) shows the voltage of the load resistor. The voltage trend in the first-type jumping region agrees well with that in Figure 4.1 (c). However, the measured voltage magnitudes are higher than those from the simulation. In the high frequency region, the measured voltage peaks around 11 Hz with the magnitude of 1.12 V. Again, the overall trend is similar to that from the simulation, but the magnitudes are different.

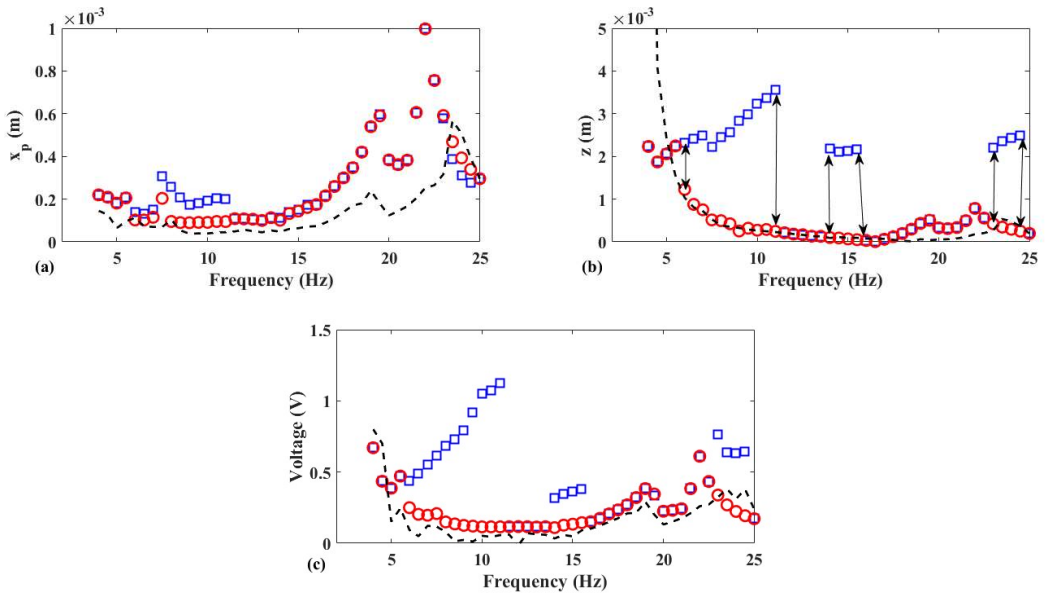

Figure 4.19 Testing results with A_y = 1 m/s^2 and R = 20000 Ω. (a) x_p; (b) z and (c) v. (Red circle: low amplitude state; Blue square: high-low amplitude state; Dashed line: FPRs without the stop blocks).

Figure 4.20 shows the experimental results with the acceleration A_y = 1.5 m/s^2. In Figure 4.20 (b), there are also three jumping regions: 6 to 9.5 Hz, 14 to 18 Hz and 20 to 23 Hz. The first region belongs to the first type of jumping while the last two regions pertain to the second type of jumping. Within the jumping region, the high state responses may appear as SMRs. Figure 4.20 (c) shows the voltage of the load resistor. In the first type of jumping region, the measured voltage peaks around 9.5 Hz with the magnitude of 0.78 V. The voltage trend in this jumping region agrees with the voltage trend in Figure 4.2 (c). However, the measured voltage magnitudes are lower than those from the simulation.

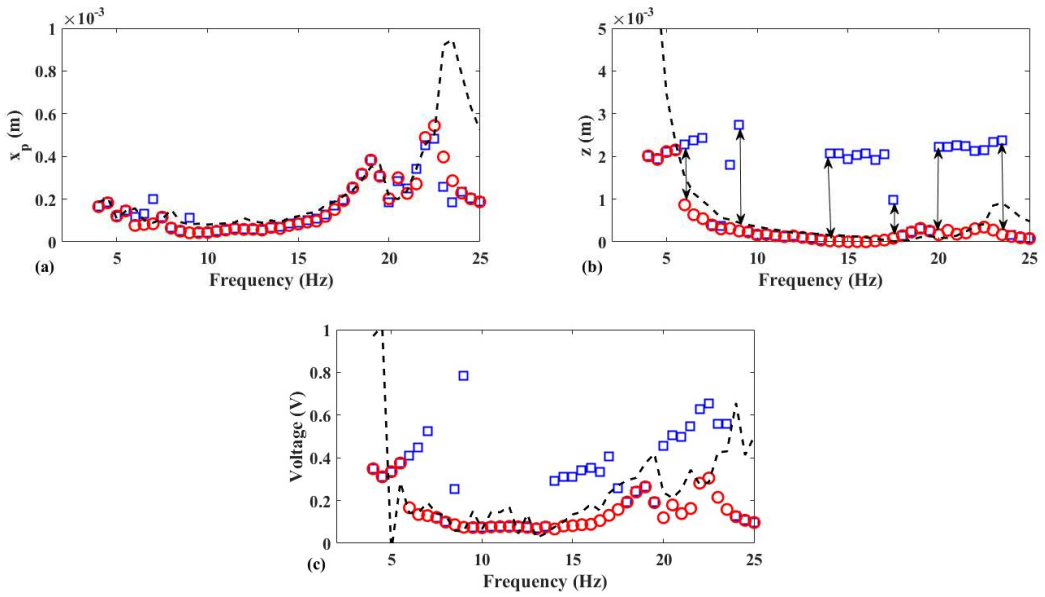

Figure 4.20 Testing results with A_y = 1.5 m/s^2 and R = 20000 Ω. (a) x_p; (b) z and (c) v. (Red circle: low amplitude state; Blue square: high-low amplitude state; Dashed line: states without the stop blocks).

Figure 4.21 shows the experimental results with the acceleration A_y = 2.0 m/s^2. In Figure 4.21 (b), only two jumping regions are found. They are: 6.5 to 13 Hz and 22 to 24.5 Hz. In this acceleration level, the first region belongs to the first type of jumping region while the second region belongs to the second type of jumping. This first type of jumping region is the widest region among the three excitation levels. In Figure 4.21 (c), the voltage of the load resistor is shown with the measured peak voltage around 1.87 V at frequency 13 Hz. The measured voltage trend agrees well with that in Figure 4.3 (c) while the measured voltage magnitudes are lower than those from the simulation.

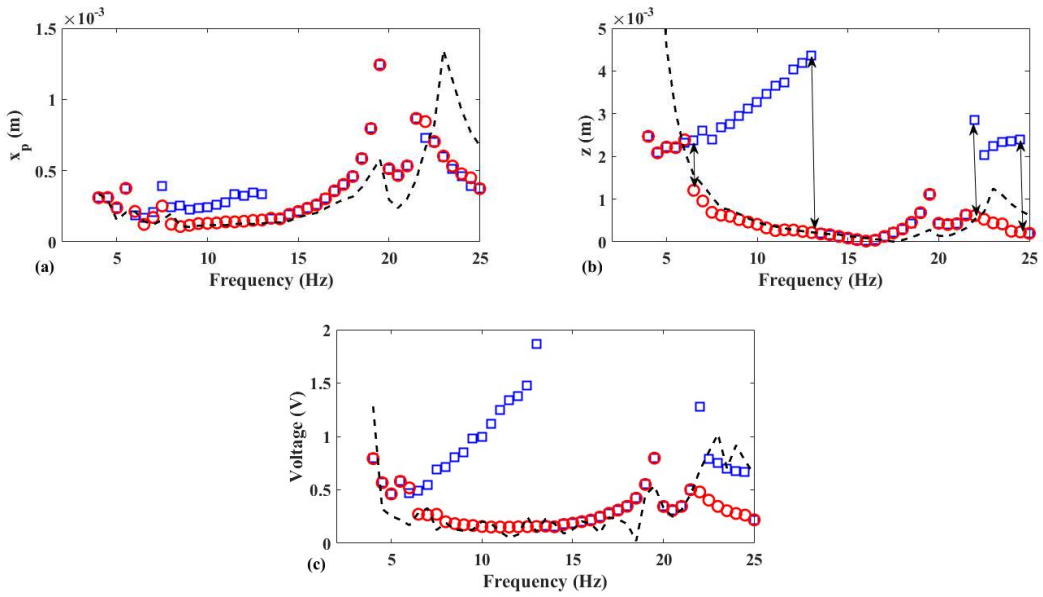

Figure 4.21 Testing results with A_y = 2 m/s^2 and R = 20000 Ω. (a) x_p; (b) z and (c) v. (Red circle: low amplitude state; Blue square: high-low amplitude state; Dashed line: states without the stop blocks).

Figure 4.22 shows the responses of the system excited at f = 7.5 Hz and A_y = 1 m/s^2. Both responses are the weakly modulated ones, showing a beating phenomenon and the weakly modulated responses. Figure 4.23 shows the combined system excited at f = 7.5 Hz with acceleration of A_y = 2 m/s^2 levels. It clearly reveals the occurrence of the SMRs and beating phenomena.

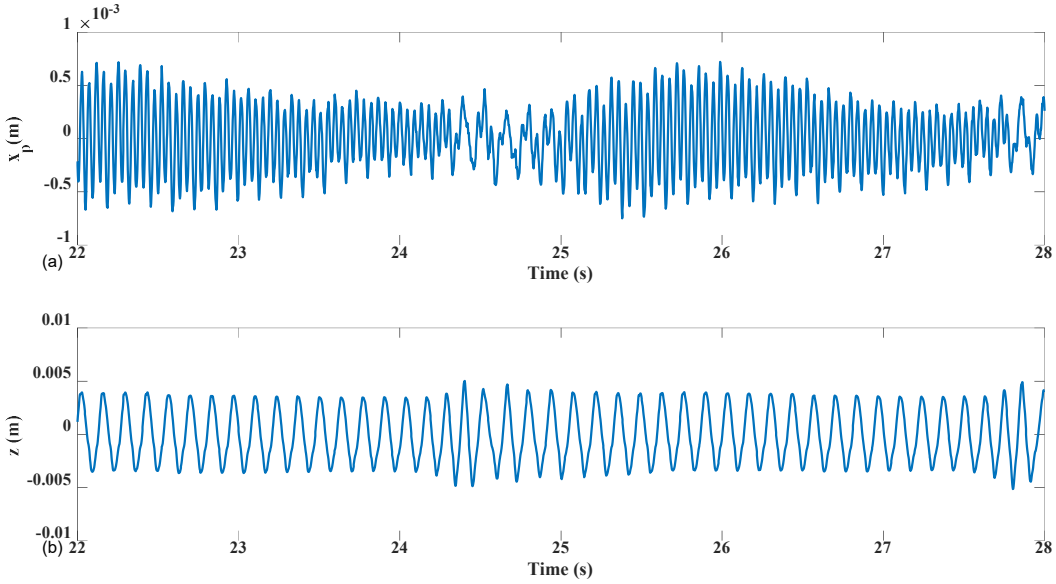

Figure 4.22 Experimental results with A_y = 1 m/s^2 and f = 7.5 Hz: (a) x_p; (b) z.

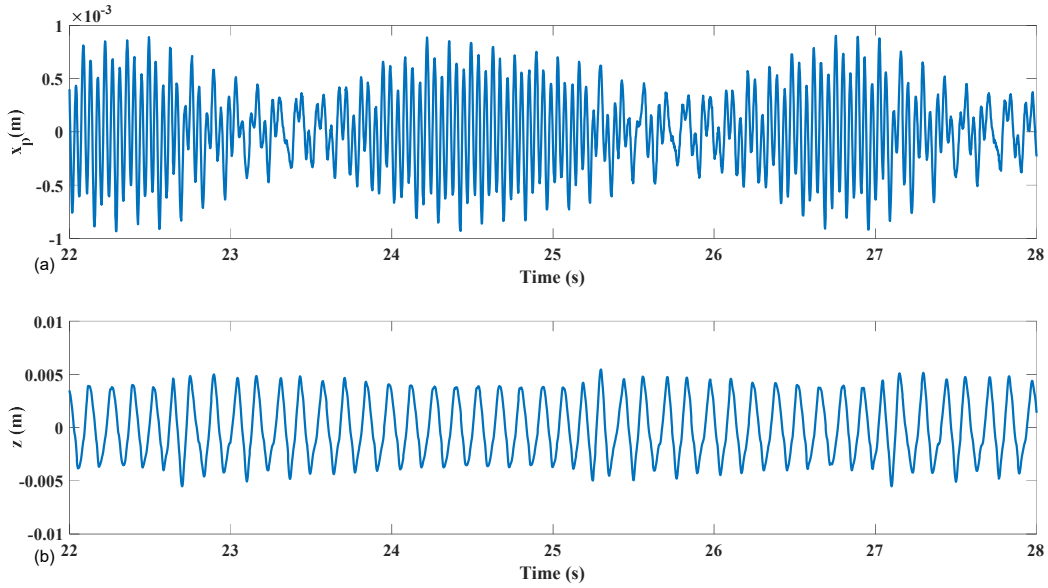

Figure 4.23 Experimental results with A_y = 2 m/s^2 and f = 7.5 Hz: (a) x_p; (b) z.

4.3 Experimental results of the strongly coupled system

Figure 4.24 shows the experimental results with the acceleration A_y = 1 m/s^2. Figure 4.24 (b) clearly shows that there are two jumping regions 8.5 to 10.5 Hz, and 13 to 14.5 Hz. The first region belongs to the first type of jumping. Within this region, the high state responses may appear as the SMRs. The next region belongs to the second type of jumping. Within these two regions, the high state responses may appear as the SMRs as well. Comparing these results with those in Figure 4.10, the testing somewhat validates the jumping phenomenon revealed in the simulation. Figure 4.24 (c) shows the voltage of the load resistor. The voltage trend in the first-type jumping region agrees well with that in Figure 4.10 (c). In the high frequency region, the measured voltage peaks around 10.5 Hz with the magnitude of 0.8844 V. Again, the overall trend is similar to that from the simulation, but the magnitudes are different.

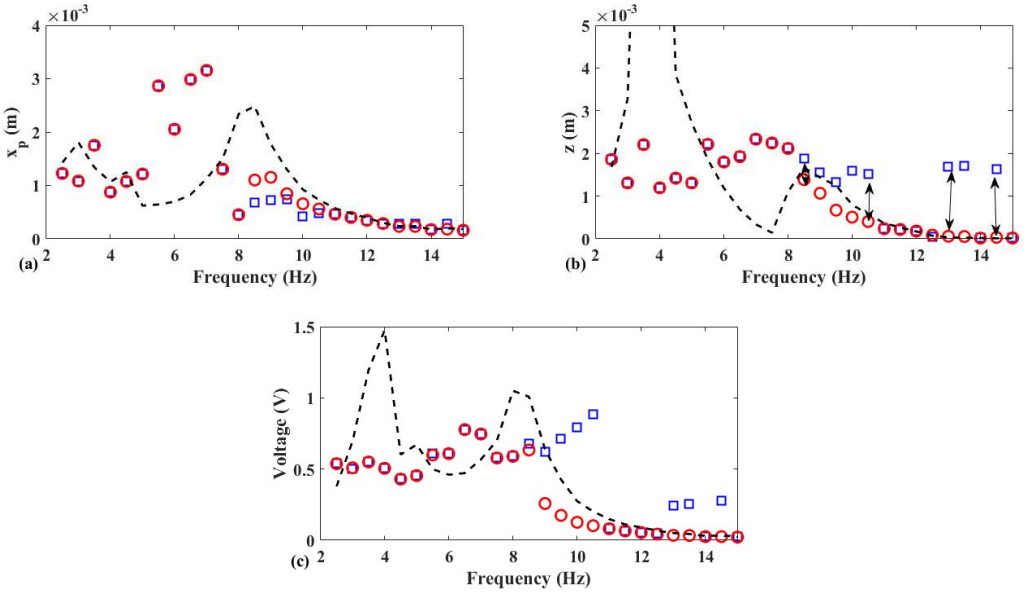

Figure 4.24 Testing results with Ay = 1 m/s2 and R = 20000 Ω. (a) xp; (b) z and (c) v. (Red circle: low amplitude state; Blue square: high-low amplitude state; Dashed line: states without the stop blocks).

Figure 4.25 shows the experimental results with the acceleration A_y = 1.5 m/s^2. In Figure 4.25 (b), there are also two jumping regions: 9.5 to 11.5 Hz and 14.5 to 15 Hz. The first region belongs to the first type of jumping while the second regions pertain to the second type of jumping. Within the jumping region, the high state responses may appear as SMRs. Figure 4.25 (c) shows the voltage of the load resistor. In the first type of jumping region, the measured voltage peaks around 10.5 Hz with the magnitude of 0.91 V. The voltage trend in this jumping region agrees with the voltage trend in Figure 4.11 (c). However, the measured voltage magnitudes are different but close to those from the simulation.

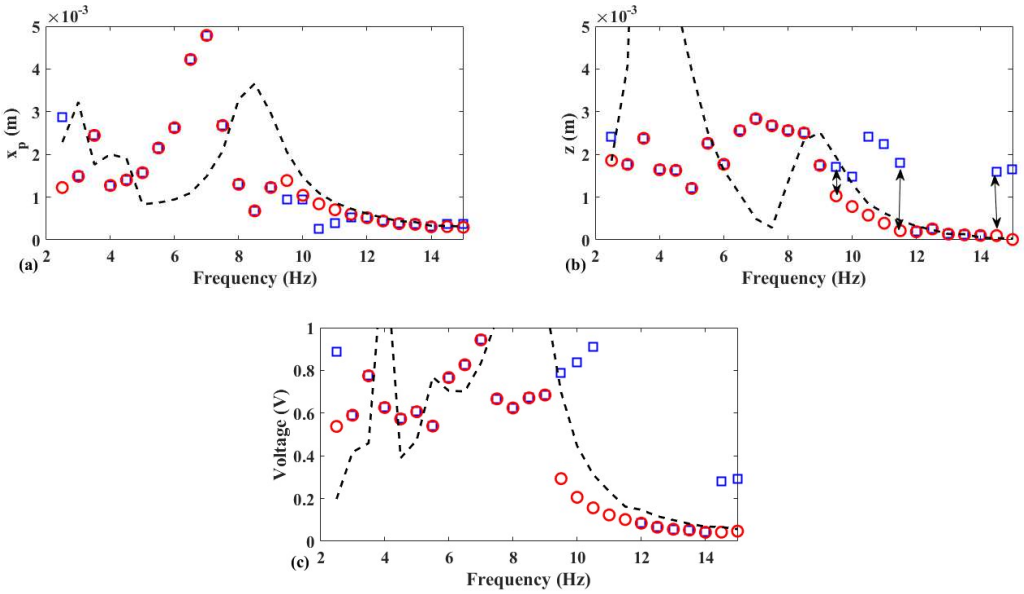

Figure 4.25 Testing results with A_y = 1.5 m/s^2 and R = 20000 Ω. (a) x_p; (b) z and (c) v. (Red circle: low amplitude state; Blue square: high-low amplitude state; Dashed line: states without the stop blocks).

Figure 4.26 shows the experimental results with the acceleration A_y = 2.0 m/s^2. In Figure 4.26 (b), only two jumping regions are found and they are: 10 to 12.5 Hz and 13 to 15 Hz. In this acceleration level, the first region belongs to the first type of jumping region while the second region belongs to the second type of jumping. This first type of jumping region is the widest region among the three excitation levels. In Figure 4.26 (c), the voltage of the load resistor is shown with

the measured peak voltage around 1.288 V at frequency 12.5 Hz. The measured voltage trend agrees well with that in Figure 4.12 (c) while the measured voltage magnitudes are lower than voltage magnitude responses from the simulation.

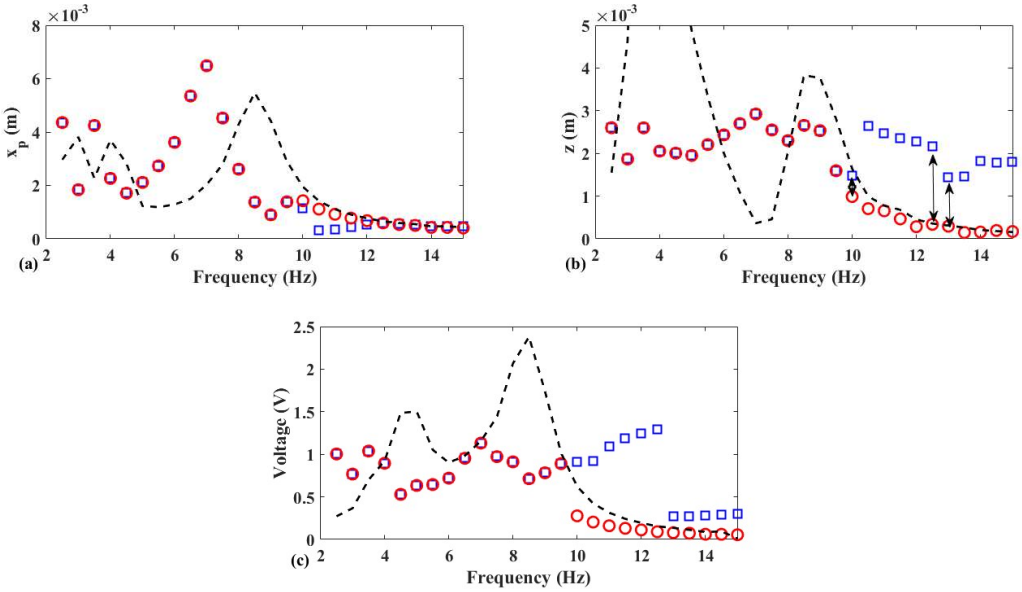

Figure 4.26 Testing results with A_y = 2 m/s^2 and R = 20000 Ω. (a) x_p; (b) z and (c) v. (Red circle: low amplitude state; Blue square: high-low amplitude state; Dashed line: states without the stop blocks).

Figure 4.27 shows the responses of the system excited at f = 10 Hz, and A_y = 1 m/s^2. Both the responses are the strongly modulated responses and showing a beating phenomenon. Figure 4.28 shows the combined system excited at f = 9 Hz with acceleration of A_y = 2 m/s^2 levels. It clearly reveals the occurrence of the SMRs and beating phenomena.

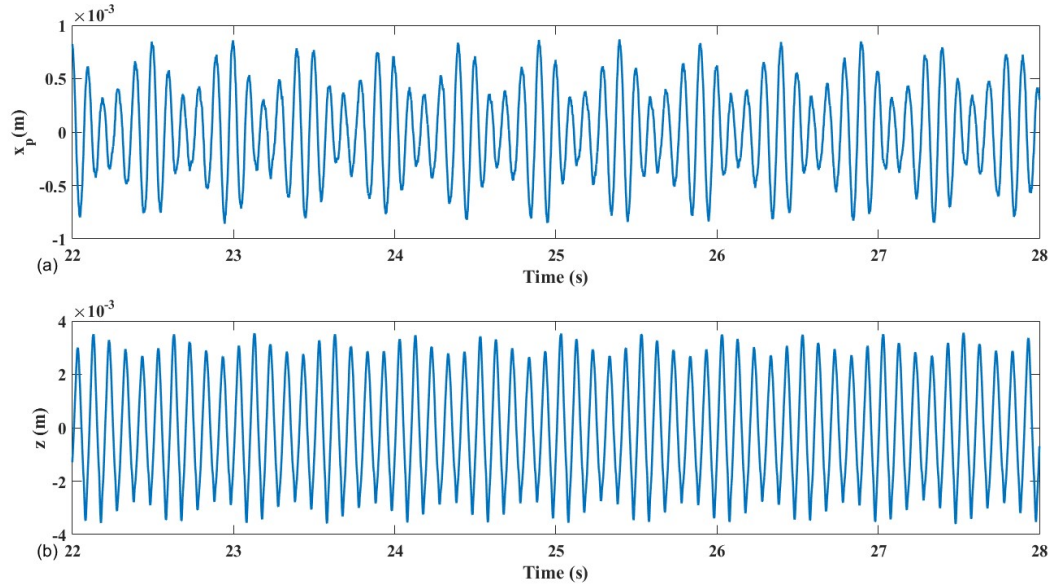

Figure 4.27 Experimental results with $A_y = 1$ m/s^2 and $f = 10$ Hz: (a) x_p; (b) z.

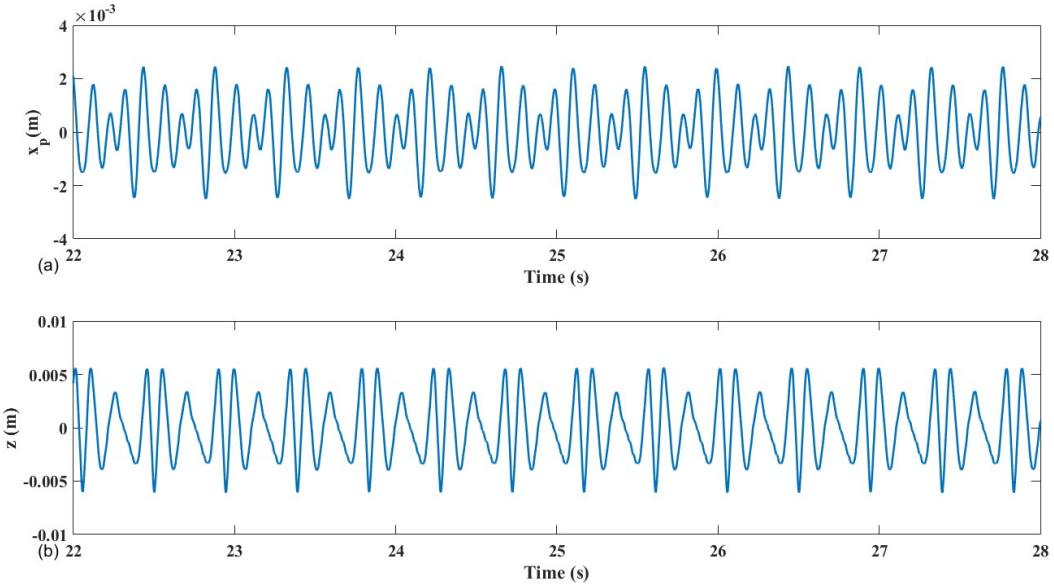

Figure 4.28 Experimental results with $A_y = 2$ m/s^2 and $f = 9$ Hz: (a) x_p; (b) z.

4.4 Conclusion

The harmonically forced responses of the weakly coupled system and strongly coupled system are investigated by the computer simulation study. The frequency response plots are obtained by the upsweep and downsweep excitations for the different base acceleration levels. The results from both the weakly coupled system and strongly coupled system show some typical features of the NES such as the responses' dependence on the excitation level, jumping phenomena, strongly modulated responses (SMRs), and so on. However, there are two notable differences between the two systems. For the weakly coupled system, there are two jumping regions. The low frequency jumping appears easily for the excitation levels used while the high frequency jump occurs only when the excitation level is high enough. For the strongly coupled system, there is only one jumping region that is around the natural frequency of the primary system. The experimental studies are conducted to validate the harmonic forced responses of the weakly coupled system and strongly coupled system. Overall, the experimental results show the similar trends as those from the simulation.

Chapter 5 Conclusion

The main purpose of this study is to develop a device for broadband vibration suppression and energy harvesting. For this propose, in Chapter 2, the three proposed apparatuses of the variant NES have been developed, and their parameters were identified. In the meantime, a stiff primary system and a flexible primary system have been developed, and their parameters were found. An experiment has been conducted to select one variant NES for subsequent study. The key findings are as follows. The proposed variant NESs are based on the use of different types of stop blocks: the single-stop blocks, double-stop blocks and continuous-contact blocks. The nonlinear stiffness and piecewise linear stiffness of each of the variant NESs have been determined based on testing results. Comparing the identification results indicates that the apparatus with double-stop blocks is closest to the NES as it has a low linear stiffness and high nonlinear stiffness.

The transient responses of the two combined systems have been investigated in Chapter 3. It has been found that there is a critical energy threshold for establishment of the TET. The initial energy of the combined systems should exceed this energy threshold so that the combined systems could be activated into the 1:1 resonance for the TET to be established. Based on the simulation and experimental results, the weakly coupled system possesses a better nonlinear capture than the strongly coupled system. Moreover, the accumulated energy capture in the piezoelectric energy harvester of the weakly coupled system is greater than the strongly coupled system.

In Chapter 4, the harmonically forced responses of the weakly coupled system and strongly coupled systems have been investigated by simulation. The frequency response plots (FRPs) have been obtained by the upsweep and downsweep excitations for different base acceleration levels. The results have shown the typical features of the NES: the jumping phenomena and the strongly modulated responses (SMRs). The voltage responses at five different load resistances have been examined under different base excitation levels. The experimental study has been conducted to

validate the simulation study. The results show a good match with those from simulation. The typical features such as the jumping phenomena and the SMRs have been observed.

Future work may consider optimizing the proposed apparatus. For this concern, the improvement on the design of the continuous-contact blocks can be investigated. The current design of the variant NES with the continuous-contact blocks produces a relatively low nonlinear stiffness compared with the variant NES with double-stop blocks. A better design of the quartic surface can be used to process a strong nonlinearity in the NES. Finally, the dynamic responses of the system subject to random excitation can be an interesting topic to be investigated.

References

[1] S. P. Beeby, R. N. Torah, M. J. Tudor, P. Glynne-Jones, T. O'Donnell, C. R. Saha and Roy, "A micro electromagnetic generator for vibration energy harvesting," *Journal of Micromechanics and Microengineering,* 5 June 2007.

[2] A. Erturk, J. Hoffmann and D. Inman, "A piezomagnetoelastic structure for broadband vibration energy harvesting.," *American Institute of Physics,* vol. 94, p. 254102, 2009.

[3] M. Franchek, M. Ryan and R. Bernhard, "Adaptive passive vibration control," *Journal of Sound and Vibration,* vol. 189, no. 5, pp. 565-585, 1995.

[4] D. Leo and D. Inman, "A quadratic programming approach to the design of active-passive vibration isolation systems," *Journal of Sound and Vibration,* pp. 807-825, 1999.

[5] J. M.R. and S. J.Q, "Passive tuned vibration absorbers for sound radiation reduction from vibrating panels," *Journal of Sound and Vibration,* pp. 577-583, 1996.

[6] S. J.Q., J. M.R. and N. M.A., "Passive, adaptive and active tuned vibration absorbers—a survey," *Journal of Mechanical Design,* vol. 117, no. B, pp. 234-242, 1995.

[7] C. Johnson, "Design of passive damping systems.," *Journal of Vibration and Acoustics,* vol. 117, no. B, pp. 171-176, 1995.

[8] K. Williams, G. Chiu and R. Bernhard, "Adaptive-passive absorbers using shape-memory alloys," *Journal of Sound and Vibration,* vol. 249, no. 5, pp. 835-848, 2002.

[9] A. H. Nayfeh and D. T. Mook, Nonlinear Oscillations, New York: Toronto: Wiley, 1979.

[10] G. Pennisi, "Passive vibration control by using Nonlinear Energy Sink absorbers.Theoretical study and experimental investigations," *INSTITUT SUPERIEUR DE L'AERONAUTIQUE ET DE L'ESPACE (ISAE),* 2016.

[11] L. Haiping, W. Yaobing, S. Pengfei and X. Zhe, "Analysis of the dynamics of the flywheel with nonlinear vibration absorber using wavelets," in *24th International congress on sound and vibration*, London, 2017.

[12] Y. Starosvetsky and O. Gendelman, "Dynamics of a strongly nonlinear vibration absorber coupled to a harmonically excited two-degree-of-freedom system.," *Journal of Sound and Vibration,* vol. 312, no. 2008, p. 234–256, 2007.

[13] Y. Starosvetsky and O. Gendelman, "Attractors of harmonically forced linear oscillator with attached nonlinear energy sink. II: Optimization of a nonlinear vibration absorber," *Journal of Applied Mechanics,* vol. 2008, no. 51, p. 47–57, 2007.

[14] O. Gendelman, L. Manevitch, A. Vakakis and R. M'closkey, "Energy pumping in nonlinear mechanical oscillators: Part I—Dynamics of the underlying Hamiltonian systems," *Journal of Applied Mechanics,* vol. 68, no. 1, pp. 34-41, 2001.

[15] A. Vakakis and O. Gendelman, "Energy pumping in nonlinear mechanical oscillators: part II—Resonance Capture," *Journal of Applied Mechanics,* vol. 68, no. 1, pp. 42-48, 2001.

[16] X. Jiang, D. M. McFarland, L. A. Bergman and A. F. Vakakis, "Steady state passive nonlinear energy pumping in coupled oscillators: theoretical and experimental results," *Nonlinear Dynamics,* vol. 33, no. 1, p. 87–102, 2003.

[17] A. I. MUSIENKO, C. H. LAMARQUE and L. I. MANEVITCH, "Design of Mechanical Energy Pumping Devices," *Journal of Vibration and Control,* vol. 12, no. 4, p. 355–371, 2005.

[18] G. Kerschen, A. F. Vakakis, Y. S. Lee, D. M. Mcfarland, J. J. Kowtko and L. A. Bergman, "Energy Transfers in a System of Two Coupled Oscillators with Essential Nonlinearity: 1:1 Resonance Manifold and Transient Bridging Orbits," *Nonlinear Dynamics,* vol. 42, no. 3, pp. 283-303, 2005.

[19] A. Vakakis, O. Gendelman, L. Bergman, D. McFarland, G. Kerschen and Y. Lee, "Nonlinear Targeted Energy Transfer in Mechanical and Structural Systems," *Springer Science & Business Media,* 2008.

[20] Y. S. Lee, A. F. Vakakis, L. A. Bergman, D. M. McFarland, G. Kerschen, F. Nucera, S. Tsakirtzis and P. N. Panagopoulos, "Passive non-linear targeted energy transfer and its applications to vibration absorption: a review," *Sage Journals,* vol. 222, no. 2, pp. 77-134, 2008.

[21] G. Kerschen, J. J. KowtkoD, M. Mcfarland, L. A. Bergman and A. F. Vakakis, "Theoretical and Experimental Study of Multimodal Targeted Energy Transfer in a System of Coupled Oscillators," *Nonlinear Dynamics,* vol. 47, no. 1-3, p. 285–309, 2007.

[22] O. V.Gendelman, "Targeted energy transfer in systems with non-polynomial nonlinearity," *Journal of Sound and Vibration,* vol. 315, no. 3, pp. 732-745, 2008.

[23] B. Vaurigaud, A. T. Savadkoohi and C.-H. Lamarque, "Targeted energy transfer with parallel nonlinear energy sinks. Part I: Design theory and numerical results," *Nonlinear Dynamics,* vol. 66, no. 4, p. 763–780, 2011.

[24] A. T. Savadkoohi, B. Vaurigaud, C.-H. Lamarque and S. Pernot, "Targeted energy transfer with parallel nonlinear energy sinks, part II: theory and experiments," *Nonlinear Dynanics,* vol. 67, no. 1, p. 37–46, 2012.

[25] O.V.Gendelmana, T.Sapsis, A.F.Vakakis and L.A.Bergman, "Enhanced passive targeted energy transfer in strongly nonlinear mechanical oscillators," *Journal of Sound and Vibration,* vol. 330, no. 1, pp. 1-8, 2011.

[26] S. Tsakirtzis, P. N. Panagopoulos, G. Kerschen, O. Gendelman, A. F. Vakakis and L. A. Bergman, "Complex dynamics and targeted energy transfer in linear oscillators coupled to multi-degree-of-freedom essentially nonlinear attachments," *Nonlinear Dynamics,* vol. 48, no. 3, p. 285–318, 2007.

[27] R.Belleta, B.Cochelin, R.Côte and P.-O.Mattei, "Enhancing the dynamic range of targeted energy transfer in acoustics using several nonlinear membrane absorbers," *Journal of Sound and Vibration,* vol. 331, no. 26, pp. 5657-5668, 2012.

[28] B.Vaurigaud, L.I.Manevitch and C.-H.Lamarque, "Passive control of aeroelastic instability in a long span bridge model prone to coupled flutter using targeted energy transfer," *Journal of Sound and Vibration,* vol. 330, no. 11, pp. 2580-2595, 2011.

[29] D. DaneQuinn, OlegGendelman, G. Kerschenc, T. P.Sapsis, L. A.Bergman and A. F.Vakakis, "Efficiency of targeted energy transfers in coupled nonlinear oscillators associated with 1:1 resonance captures: Part I," *Journal of Sound and Vibration,* vol. 311, no. 3-5, pp. 1228-1248, 2008.

[30] T.P.Sapsis, A.F.Vakakis, O.V.Gendelman, L.A.Bergman, G.Kerschen and D.D.Quinn, "Efficiency of targeted energy transfers in coupled nonlinear oscillators

associated with 1:1 resonance captures: Part II, analytical study," *Journal of Sound and Vibration,* vol. 325, no. 1-2, pp. 297-320, 2009.

[31] A. L. Zulli, "Dynamic analysis of externally excited NES-controlled systems via a mixed Multiple Scale/Harmonic Balance algorithm," *Nonlinear Dynamics,* vol. 70, no. 3, p. 2049–2061, 2012.

[32] Y.Starosvetsky and O.V.Gendelman, "Dynamics of a strongly nonlinear vibration absorber coupled to a harmonically excited two-degree-of-freedom system," *Journal of Sound and Vibration,* vol. 312, no. 1-2, pp. 234-256, 2008.

[33] D. Zulli and A. Luongo, "Nonlinear energy sink to control vibrations of an internally nonresonant elastic string," *Meccanica,* vol. 50, no. 3, p. 781–794, 2015.

[34] A. Luongo and D. Zulli, "Nonlinear energy sink to control elastic strings: the internal resonance case," *Nonlinear Dynamics,* vol. 81, no. 1-2, p. 425–435, 2015.

[35] E.Gourdon, N.A.Alexander, C.A.Taylor, C.H.Lamarque and S.Pernot, "Nonlinear energy pumping under transient forcing with strongly nonlinear coupling: Theoretical and experimental results," *Journal of Sound and Vibration,* vol. 300, no. 3-5, pp. 522-551, 2007.

[36] D. M. McFarland, B. Lawrence A. and A. F. Vakakis, "Experimental study of non-linear energy pumping occurring at a single fast frequency," *International Journal of Non-Linear Mechanics,* vol. 40, no. 6, pp. 891-899, 2005.

[37] G. Kerschen, J. J. Kowtko, D. M. Mcfarland, L. A. Bergman and A. F. Vakakis, "Theoretical and Experimental Study of Multimodal Targeted Energy Transfer in a System of Coupled Oscillators," *Nonlinear Dynamics,* vol. 47, no. 1-3, p. 285–309, 2006.

[38] G. Kerschen, D. M. McFarland, J. J. Kowtko, Y. S. Lee, L. A. Bergman and A. F. Vakakis, "Experimental demonstration of transient resonance capture in a system of two coupled oscillators with essential stiffness nonlinearity," *Journal of Sound and Vibration,* vol. 299, no. 4-5, pp. 822-838, 2007.

[39] R.Bellet, B.Cochelin, P.Herzog and P.-O.Mattei, "Experimental study of targeted energy transfer from an acoustic system to a nonlinear membrane absorber," *Journal of Sound and Vibration,* vol. 329, no. 14, pp. 2768-2791, 2010.

[40] E. Gourc, G. Michon, S. Seguy and A. Berlioz, "Theoretical and Experimental Study of an Harmonically Forced Vibro-Impact Nonlinear Energy Sink," in *ASME 2013 International Design Engineering Technical Conferences and Computers and Information in Engineering Conference*, Portland, 2013.

[41] D. Kremer and K. Liu, "A nonlinear energy sink with an energy harvester: Transient responses," *Journal of Sound and Vibration,* vol. 333, no. 20, pp. 4859-4880, 2014.

[42] D. Kremer and K. Liu, "A nonlinear energy sink with an energy harvester: Harmonically forced responses," *Journal of Sound and Vibration,* vol. 410, pp. 287-302, 2017.

[43] Y. Zhang, L. Tang and K. Liu, "Piezoelectric energy harvesting with a nonlinear energy sink," *Journal of Intelligent Materials Systems and Structures,* vol. 28, no. 3, pp. 307-322, 2016.

[44] L. Xiong, L. Tang, K. Liu and B. R. Mace, "Broadband piezoelectric vibration energy harvesting using a nonlinear energy sink," *Journal of Physics D: Applied Physics,* 2018.

[45] S. Priya and D. Inman, Energy Harvesting Technologies, New York: Springer Science+Business Media, 2009.

[46] S. P. Beeby, M. J. Tudor and N. M. White, "Energy harvesting vibration sources for microsystems applications," *Measurement Science and Technology,* vol. 17, no. 12, 2006.

[47] P. D. Mitcheson, E. M. Yeatman, G. K. Rao, A. S. Holmes and T. C. Green, "Energy Harvesting From Human and Machine Motion for Wireless Electronic Devices," *Proceedings of the IEEE ,* vol. 96, no. 9, pp. 1457 - 1486, 2008.

[48] B. Yang, C. Lee, W. Xiang, J. Xie, J. H. He, R. K. Kotlanka, S. P. Low and H. Feng, "Electromagnetic energy harvesting from vibrations of multiple frequencies," *Journal of Micromechanics and Microengineering,* vol. 19, no. 3, 2009.

[49] P.Glynne-Jones, M.J.Tudor, S.P.Beeby and N.M.White, "An electromagnetic, vibration-powered generator for intelligent sensor systems," *Sensors and Actuators A: Physical,* vol. 110, no. 1-3, pp. 344-349, 2004.

[50] S. P. Beeby, R. N. Torah, M. J. Tudor, P. Glynne-Jones, T. O'Donnell, C. R. Saha and S. Roy, "A micro electromagnetic generator for vibration energy harvesting," *Journal of Micromechanics and Microengineering,* vol. 17, no. 7, 2007.

[51] P. Wang, K. Tanaka, S. Sugiyama, X. Dai, X. Zhao and J. Liu, "A micro electromagnetic low level vibration energy harvester," *Microsystem Technolgies,* vol. 15, no. 6, p. 941–951, 2009.

[52] A. Erturk and D. J. Inman, "An experimentally validated bimorph cantilever model for piezoelectric energy harvesting from base excitations," *Smart Materials and Structures,* vol. 18, no. 2, 2009.

[53] H.-B. Fang, J.-Q. Liu, Z.-Y. Xu, L. Dong, L. Wang, D. Chen, B.-C. Cai and Y. Liu, "Fabrication and performance of MEMS-based piezoelectric power," *Microelectronics Journal,* vol. 37, no. 11, pp. 1280-1284, 2006.

[54] H. S. Kim, J.-H. Kim and J. Kim, "A review of piezoelectric energy harvesting based on vibration," *International Journal of Precision Engineering and Manufacturing,* vol. 12, no. 6, p. 1129–1141, 2011.

[55] H. A. Sodano, D. J. Inman and G. Park, "Comparison of Piezoelectric Energy Harvesting Devices for Recharging Batteries," *Journal of Intelligent Materials Systems and Structures,* vol. 16, no. 10, pp. 799-807, 2005.

[56] A. Erturk and D. J. Inman, "A Distributed Parameter Electromechanical Model for Cantilevered Piezoelectric Energy Harvesters," *Journal of Vibration and Acoustics,* vol. 130, no. 4, p. 041002, 2008.

[57] A. Erturk and D. Inman, "On Mechanical Modeling of Cantilevered Piezoelectric Vibration Energy Harvesters," *Journal of Intelligent Materials Systems and Structures,* vol. 19, no. 11, pp. 1311-1325, 2008.

[58] H. A. Sodano, D. J. Inman and G. Park, "Comparison of Piezoelectric Energy Harvesting Devices for Recharging Batteries," *Journal of Intelligent Materials Systems and Structures,* vol. 16, no. 10, pp. 799-807, 2005.

[59] F. Cottone, H. Vocca and L. Gammaitoni, "Nonlinear Energy Harvesting," *Physical Review Letters,* vol. 102, no. 8-27, 2009.

[60] K.Worden, "Data processing and experiment design for the restoring force surface method, part I: integration and differentiation of measured time data," *Mechanical Systems and Signal Processing,* vol. 4, no. 4, pp. 295-319, 1990.

[61] K.Worden, "Data processing and experiment design for the restoring force surface method, part II: Choice of excitation signal," *Mechanical Systems and Signal Processing,* vol. 4, no. 4, pp. 321-344, 1990.

[62] M. Kurt, M. Eriten, D. M. McFarland, L. A.Bergman and A. F.Vakakis, "Strongly nonlinear beats in the dynamics of an elastic system with a strong local stiffness nonlinearity: Analysis and identification," *Journal of Sound and Vibration,* vol. 333, no. 7, pp. 2054-2072, 2014.

[63] Y.Starosvetsky and O.V.Gendelman, "Strongly modulated response in forced 2DOF oscillatory system with essential mass and potential asymmetry," *Physica D: Nonlinear Phenomena,* vol. 237, no. 13, pp. 1719-1733, 2008.

[64] E. Gourc, G. Michon, S. Seguy and A. Berlioz, "Targeted Energy Transfer Under Harmonic Forcing With a Vibro-Impact Nonlinear Energy Sink: Analytical and Experimental Developments," *Journal of Vibration and Acoustics,* vol. 137, no. 3, p. 7, 2015.